From the holdings of the Department of Special Collections , Princeton University Library, Princeton, NJ

These documents are either in the public domain, or can only be used for educational and research purposes (Fair use) as per U.S. Copyright law (text below). By accessing this file, all users agree that their use falls in the public domain or within fair use as defined by the copyrightlaw. We do not charge any permission or usage fees for the publication of images of material inour collections, including those provided by Princeton University Library, via our website, catalog, or directly from staff.For more information regarding copyright, credit, and citation please review the information onthe Copyright, Credit and Citation Guidelines page of our website.
https://library.princeton.edu/special-collections/policies/copyright-credit-and-citation-guidelines. If you have any questions, including how to order higher-quality images from the collection, contact Special Collections Public Services via our Ask Us! Form. https://library.princeton.edu/special-collections/ask-us

---

Doctoral Dissertations, 2011-2026 Atmospheric and Oceanic Sciences

2019

Eddy equilibration in idealized models of the extratropical troposphere

Chang, Chiung-Yin

Princeton, NJ : Princeton University

---

http://arks.princeton.edu/ark:/88435/dsp01db78tf96p

U.S. Copyright law: The copyright law of the United States (Title 17, §108, United States Code) governs the making of photocopies or other reproductions of copyrighted material. Under certain conditions specified in the law, libraries and archives are authorized to furnish a photocopy or other reproduction. One of these specified conditions is that the photocopy or reproduction is not to be used for any purpose other than private study, scholarship, or research. If a user makes a request for, or later uses, a photocopy or reproduction for purposes in excess of fair use that user may be liable for copyright infringement. This institution reserves the right to refuse to accept a copying order if, in its judgment, fulfillment of the order would involve a violation of copyright law. https://www.copyright.gov/title17/title17.pdf

Eddy equilibration in idealized models of the extratropical troposphere

Chiung-Yin Chang

A Dissertation
Presented to the Faculty
of Princeton University
in Candidacy for the Degree
of Doctor of Philosophy

Recommended for Acceptance
by the Program in
Atmospheric and Oceanic Sciences
Adviser: Isaac M. Held

September 2019

© Copyright by Chiung-Yin Chang, 2019.

All rights reserved.

Abstract

The equilibration of the extratropical troposphere is controlled in large part by the transient eddy heat fluxes. This thesis analyzes some idealized models that capture the essential sources of complexity which have hindered our understanding of these fluxes. In particular, it attempts to eliminate some knowledge gaps between proposed turbulence diffusivity theories for these fluxes.

The thesis begins by comparing two of these theories, one motivated by homogeneous quasigeostrophic (QG) simulations and one by parameter variations in a comprehensive atmospheric model. The two theories share the same turbulent inverse energy cascade argument but differ in the assumptions concerning the mixing slope used in estimating the entropy budget. The importance of this mixing slope is verified using an idealized dry general circulation model (GCM).

We find that the inverse cascade part of these theories fails to explain some of the GCM simulations. Hence, we return to the homogeneous two-layer QG model. In the limit of vanishing environmental vorticity gradient $\beta = 0$, we find that the diffusivity does not depend on the friction in the same way as the passive tracer diffusivity in barotropic turbulence. Unlike what is typically assumed, there is no classical inverse cascade inertial range in the two-layer model.

We next show that the β dependence of heat flux diffusivity can be combined with the dependence on friction in a single nondimensional parameter. Based on this result, we discuss how the heat flux diffusivity is suppressed by β due to wave propagation in addition to its effect on the extent of the inverse cascade.

Finally, we return to the idealized GCM to evaluate the maximum entropy production (MEP) argument, which suggests that the eddy heat fluxes adjust to maintain the MEP state. We solve for the MEP climate and show that it is unlikely to be physically relevant even if one constrains the global mean vertical temperature profile. We

argue against the use of the MEP argument and reaffirm the need to thoroughly understand the eddy dynamics.

Acknowledgements

First and foremost, I want to thank my adviser Isaac Held, without whom this thesis would not be possible. It is difficult to put into words how important he is to shape the way I think about climate and to provide all kinds of support along the way. To cut a long story short, he is such a wonderful adviser and mentor.

I also want to thank Pablo Zurita-Gotor for his help on the various parts of this thesis and to agree to be its reader. I am grateful to my committee, Stephan Fueglistaler, Steve Garner, and Yi Ming, for their encouragement and the efforts they made to understand and improve this work. In addition, many GFDL scientists and AOS graduate students also offered their assistance for me to carry out my research, even though some did not end up in this thesis.

It is because my cohort, Xin Rong Chua, Spencer Clark, Michelle Frazer, Tsung-Lin Hsieh, Justin Ng, and Sarah Schlunegger, that I feel I belong to the Princeton community. On the other hand, I also thank my friends outside Princeton to keep me connect to the rest of the world and to give me excuses to escape and travel around. I am also lucky to have my CPS counselor Hilary Herbold to continue checking on me and helping me navigate through my last year in the program.

A friend once joked that people should better be away from me when I am about to graduate and head to my next step. As every time this happened in the past, one of those very close to me became sick and passed away. From this perspective, I think I should also thank everyone to stick around and, perhaps most importantly, to stay healthy.

Meow.

Contents

Abstract iii

Acknowledgements v

List of Tables x

List of Figures xi

1 Introduction **1**

1.1 Motivation 1

1.2 Overview 8

2 Eddy equilibration in an idealized GCM: thermodynamic budgets and QG theory **13**

2.1 Introduction 13

2.2 The idealized GCM and the numerical simulations 21

2.3 A generalized thermodynamic relation for the idealized GCM 23

2.4 Validating individual scaling relations: varying Δ_y simulations 29

2.4.1 Relating diffusivity to kinetic energy level 29

2.4.2 Relating kinetic energy level to the rate of kinetic energy dissipation 31

2.4.3 Estimating kinetic energy dissipation from entropy and kinetic energy budgets 31

2.4.4 Relating entropy destruction to the mean thermal structure . 33

2.5 Validating individual scaling relations: varying Ω simulations 34
2.6 Overall performance as a closed theory 37
2.6.1 Approximating total heat flux as eddy heat flux 37
2.6.2 Error assessment 38
2.6.3 Closure form 39
2.7 Conclusions 40
2A Calculations of global kinetic energy and entropy budgets 52

3 Eddy equilibration in two-layer QG models: the roles of surface friction 55

3.1 Introduction 55
3.2 Asymmetric versus symmetric drag simulations 62
3.3 Symmetric drag simulations versus theoretical prediction 65
3.4 Asymmetric drag simulations versus modified prediction 70
3.5 Equilibration without an inverse cascade 72
3.6 Linear versus quadratic drag 74
3.7 A comparison with TY06 76
3.8 Homogeneous and inhomogeneous comparison 79
3.9 Discussion and conclusions 81
3A Equations of the model 94

4 Eddy equilibration in two-layer QG models: the roles of β 96

4.1 Introduction 96
4.2 Parameter dependence of D_τ 102
4.2.1 Overview of the simulations 102
4.2.2 The propagation-suppression effect 107
4.2.3 The spectrally nonlocal barotropic energy input effect 110
4.3 Assessment on alternative scaling relations 114

4.3.1 Empirical fits 114
4.3.2 $\epsilon^{3/5}\beta^{-4/5}$ and the three diffusivities 115
4.3.3 Bulk mixing length theory with Rhines scale 117
4.4 Conclusions 120

5 Maximum entropy production and the climates of the idealized GCM 134

5.1 Introduction 134
5.2 The idealized GCM and its MEP solution 139
5.3 Relating the mean thermal stratification to the strength of global entropy cycle 144
5.4 Imposing a constraint on the mean thermal stratification 147
5.5 Interpreting the constrained MEP solution 149
5.6 Summary and discussion 153

6 Conclusion 163

6.1 Summary of the findings 163
6.2 Directions for future work 167
6.2.1 Connecting back to barotropic turbulence 167
6.2.2 Introducing spatial inhomogeneity 168
6.2.3 Determining the thermal stratification 170
6.2.4 Toward a moist theory 171
6.3 In a nutshell 172

Bibliography 175

List of Tables

4.1 A list of the examined variables and their diagnostic definitions. ψ and τ denotes for the barotropic and baroclinic streamfunction, respectively. The angle brackets refer to the domain averaged. 126

List of Figures

1.1 An overview of the relations between the chapters (indicated by the numbered ovals) and the addressed references (indicated by the acronyms). The acronyms stand for the following list of previous studies: Larichev and Held (1995, LH95), Held and Larichev (1996, HL96), Held (1999, H99), Lapeyre and Held (2003, LH03), Zurita-Gotor (2007, Z07), Zurita-Gotor and Vallis (2009, ZV09), Jansen and Ferrari (2012, JF12), Jansen and Ferrari (2013a, JF13), Barry et al. (2002, BCT02), Thompson and Young (2006, TY06), Thompson and Young (2007, TY07), Kong and Jansen (2017, KJ17), Paltridge (1975, P75), and Paltridge (1978, P78). 12

2.1 Mean thermal structure of the control simulation (Δ_y =60K and $\Omega = \Omega_e$). The potential temperature is plotted as the gray contours with a 10K interval, and the nondissipative diabatic heating is plotted as the colored shading with its magnitude indicated by the colorbar. The two black dots denote for the centroids of heating and cooling, respectively, and the dashed line linking them is the bulk mixing surface defined accordingly. The detailed definitions are described in the text. 44

2.2 Diffusivity (D), eddy kinetic energy (EKE), and kinetic energy dissipation (ϵ_d) in the varying Δ_y simulations: the log-log plots of the simulations versus the predictions based on the scaling relations. In the top panel, two D predictions are provided by Eq. (2.1) with V estimated as the squared root of the EKE in two different ways: one is the total EKE (V_t; filled circles) and the other is the barotropic EKE (V_b; open circles). In the middle panel, the V_t^2 prediction is provided by Eq. (2.2) with ϵ estimated as ϵ_d. In the bottom panel, two ϵ_d predictions are provided. The first is from Eq. (2.3) the simulated globally averaged entropy destruction with a constant reference temperature ($\dot{s}$ times T_0; filled circles), and the second is the globally averaged eddy kinetic energy generation (ϵ_p; open circles). All the predicted values are multiplied by a constant such that the prediction for the control simulation (black filled) equals to the simulated value. The arrows indicate the direction where Δ_y increases. 45

2.3 Globally averaged entropy destruction ($\dot{s}$) in the varying Δ_y simulations: the log-log plots of the simulated $\dot{s}$ versus three different predictions based on Eq. (2.9) ($T_0{}^{-1}\mathcal{F}\,\partial_y \ln \bar{T}\big|_m$; colored filled) , Eq. (2.11) ($T_0{}^{-1}\mathcal{F}\,\partial_y \ln \bar{T}\big|_p$; colored open), and Eq. (2.10) ($T_0{}^{-1}\mathcal{F}\kappa\,\partial_y \ln \bar{p}|_\theta$; black open). All the relevant quantities are diagnosed from the simulations with the details described in the text. All the predicted values are multiplied by a constant such that the prediction for the control simulation (black filled) equals to the simulated $\dot{s}$. The arrows indicate the direction where Δ_y increases. 46

2.4 As in Fig. 2.3, but for the varying Ω simulations. 47

2.5 As in Fig. 2.2, but for the varying Ω simulations. 48

2.6 Total heat fluxes in the varying Δ_y (blue) and Ω (red) simulations: the log-log plots of the simulated total heat flux ($\mathcal{F}$) versus the predictions by Eq. (2.12). All the predicted values are multiplied by a constant such that the prediction for the control simulation (black filled) equals to the simulated $\mathcal{F}$. The arrows indicate the direction that the parameters' value increases. 49

2.7 Error contribution by each scaling assumption to diffusivity prediction in the varying Δ_y (blue) and Ω (red) simulations: the log-log plots of the simulated diffusivity (D) versus the predictions based on the various combinations of the acaling relations. All the predicted values are multiplied by a constant such that the prediction for the control simulation (black filled) equals to the simulated D. 50

2.8 Final results of diffusivity prediction by the closure form in the varying Δ_y (blue) and Ω (red) simulations: the log-log plots of the simulated diffusivity (D) versus its predictions in two different ways of visualization. All the predicted values are multiplied by a constant such that the prediction for the control simulation (black filled) equals to the simulated D. 51

2.9 Budget analysis for the varying Δ_y (left) and Ω (right) simulations: (from top to bottom) the global kinetic energy budget, the global entropy budget, and the averaged dissipative temperature (T_ϵ). The definitions of the terms are described in Appendix 2A. 54

3.1 A summary of the parameter settings for each set of numerical simulations: (from left to right) the chosen form of large scale friction, maximum wavenumber resolved (k_{max}), wavenumber of deformation radius (k_d), initial condition (IC), and the explored range of nondimensionalized damping strength. For initial condition, "I" refers to the simulations integrated from the infinitesimal perturbations prescribed in the same way as LH95, and "S" refers to the simulations integrated from the simulated streamfunction field taken from the $c_D k_d^{-1} = 10^{-1}$ run that is integrated from the first initial condition until statistically steady state. 86

3.2 Eddy scales in the asymmetric and symmetric drag simulations: (from top to bottom) eddy length scale (L), velocity scale (V), and diffusivity (D) as a function of damping strength ($c_D k_d^{-1}$). Simulations with the asymmetric drag are colored as red and with the symmetric drag are colored as black. The different symbols refer to the model settings with different domain sizes and spectral resolutions (Fig. 1). For an easier comparison, all the asymmetric drag results are shifted by a factor of two along x-axis, i.e. from $c_D k_d^{-1}$ to $c_D k_d^{-1}/2$ (which would be the effective drag if the drag was symmetric). In each panel, the top left solid line indicates the power law scaling estimated from a least-squared fit of the data in the $k_d = 50$, $c_D k_d^{-1} < 10^0$ symmetric drag simulations. The bottom right solid line indicates the power law scaling predicted by H99's theory, and the top right dashed line indicates the scaling proposed by Arbic and Scott (2008) in the strong asymmetric drag limit. 87

3.3 Deviations of the simulated spectrum shapes from the theory in the symmetric and asymmetric drag simulations ($k_d = 50$ only): (from top to bottom) compensate spectra of barotropic energy $(E_\psi(k)k^{5/3})^{3/2}$, compensate spectra of baroclinic available potential energy $(E_\tau(k)k^{5/3})^3$, barotropic energy spectra $E_\psi(k)$ (solid) versus the corresponding predictions by $C_\psi\epsilon_\psi(k)^{2/3}k^{-5/3}$ (dashed), and barotropic energy flux spectra $\epsilon_\psi(k)$. In each panel, the spectra for the $c_D k_d^{-1} = 10^{-1}$ and $c_D k_d^{-1} = 10^{-2}$ simulations are colored, with the rest of the cases plotted in gray. We have chosen $C_\psi = 7$ to obtain an overall reasonable fit for both sets of simulations, but we notice that this results in a slight overestimation for the symmetric drag simulations and a slight underestimation for the asymmetric drag simulations (for reasons unclear to us). The black solid line indicating the slope k^{-x} or k^x with $x \approx 0.72$ is estimated from the simulated L using Eq. (3.16) (see text for more details). 88

3.4 Relations among eddy scales in the asymmetric and symmetric drag simulations ($k_d = 50$ only): relations of eddy timescale (T) and eddy diffusivity (D) with eddy length scale (L). The slope of the black line is computed from the least-squared fit of the data from both the asymmetric and symmetric drag simulations (i.e. all the data points shown in the plot). 89

3.5 Initial condition dependence of steady state flow properties in the strong symmetric drag regime ($k_d = 10$ only): (from top to bottom) meridional kinetic energy ($\langle v^2 \rangle / 2$) to total kinetic energy ($\langle u^2 + v^2 \rangle / 2$) ratio, baroclinic kinetic energy ($\langle KE_\tau \rangle$) to total kinetic energy ($\langle KE_\psi + KE_\tau \rangle$) ratio, and baroclinic timescale (T_τ defined as the ratio of eddy length scale L and baroclinic meridional velocity V_τ) as a function of $c_D k_d^{-1}$. Two initial conditions are considered: the one with infinitesimal perturbations in the streamfunction field as described in LH95 (cross) and the other one as the steady state streamfunction field taken from the $c_D k_d^{-1} = 10^{-1}$ simulation (triangle). 90

3.6 Eddy scales in the linear and quadratic drag simulations: diffusivity (D) diagnosed from linear (square) and quadratic (circle) drag simulations as a function of linear damping strength $\kappa k_d^{-1} U^{-1}$. The two set of simulations are mapped to each other by comparing κ to the effective linear damping strength (κ_e, defined in the text) for the quadratic drag simulations. LH denotes for the run that shares the same parameter setting as the case I simulation in LH95. The solid line indicates the scaling prediction discussed in the text. 91

3.7 Scatterplots of baroclinic streamfunction (τ) and barotropic vorticity ($\nabla^2 \psi$) and the snapshots of the two fields: a simulation using linear asymmetric drag with $\kappa k_d^{-1} U^{-1} = 0.25$ (left) and another using linear symmetric drag with $\kappa k_d^{-1} U^{-1} = 0.16$ (right) are shown to compare with the simulations of Thompson and Young (2006). 92

3.8 Eddy heat fluxes in the channel model simulations: the meridional structure of eddy heat fluxes simulated from the channel model (Eq. (3.21); solid) and the predictions by a diffusive energy balance model with the diffusivity predicted by our homogeneous model simulations (Eq. (3.22); dashed). Two sets of simulations are examined: one with varying jet width at radiative equilibrium (σ) and one with varying frictional quadratic damping strength (c_D). The first set of simulations has a fixed $c_D\lambda = 10^{-1}$ and $\sigma\lambda^{-1} = 1, 2, 4, 8$ (left); the second set of simulations has a fixed $\sigma\lambda^{-1} = 8$ and $c_D\lambda = 10^{-1}, 10^{-0.5}, 10^{0}, 10^{0.5}$ (right). λ is deformation radius. The rest of the model parameters is described in the text. 93

4.1 The parameter dependence of the simulated heat flux diffusivity: (left) $\tilde{D}_\tau = D_\tau k_d U^{-1}$ plotted against $\tilde{\beta} = \beta k_d^2 U^{-1}$ and (right) $\tilde{D}_\tau$ normalized by $\tilde{D}_\tau|_{\beta=0}$ plotted against the nondimensional parameter $\tilde{\epsilon}_p^{-1/5}\tilde{\beta}^{3/5}\tilde{c}_D^{-1}$. The simulations with different $\tilde{c}_D = c_D k_d^{-1}$ are indicated by different symbols. The tildes imply the nondimensionalization by k_d and U. . . 127

4.2 The parameter dependence of the simulated heat flux diffusivity and its empirical fit: (left) $\tilde{D}_\tau$ normalized by $\tilde{D}_\tau|_{\beta=0}$ plotted against the revised nondimensional parameter $\mu = \epsilon_p^{-1/5}\beta^{3/5}c_D^{-1/2}k_d^{-1/2}$ and (right) $\tilde{D}_\tau$ plotted against $\tilde{\beta}$. The doted line in the left panel indicates the power law scaling $\mu^{-5/2}$. The empirical fit is shown as the gray line, and its functional form $f(\mu)$ is described by Eq. (4.8). See the text for the details on the inversion of Eq. (4.8) in obtaining estimates of $\tilde{D}_\tau$ in the right panel. 128

4.3 As in Fig. 4.2, but with the comparison to the two predictions based on the simulated eddy kinetic energy spectrum: the simulation (black), the prediction by the mixing length theory (D_{ml} as the integral of Eq. (4.10); red), and the prediction by the suppressed mixing length theory (D_{sml} as the integral of Eq. (4.9); blue). 129

4.4 The eddy spectra as a function of the total wavenumber (k): heat flux diffusivity ($D_\tau(k)$; left) and barotropic eddy kinetic energy ($V_\psi^2(k)$; right). Each panel shows a set of simulations with a fixed $\tilde{c}_D$ but varying $\tilde{\beta}$. On the left, the simulated $D_\tau(k)$ (black solid) is plotted along with the prediction by the suppressed mixing length theory ($D_{sml}(k)$; blue dashed). On the right, the simulated $V_\psi^2(k)$ is plotted along with the predicted spectral slope $k^{-7/3}$ (dashed). 130

4.5 The log-log plots of the predicted versus simulated eddy diffusivities: (upper left) the empirical fits obtained in Fig. 4.2 and the simulated heat flux diffusivity ($\tilde{D}_\tau$), (upper right) $\tilde{\epsilon}_p^{3/5}\tilde{\beta}^{-4/5}$ versus simulated heat flux diffusivity ($\tilde{D}_\tau$), (lower left) $\tilde{\epsilon}_p^{3/5}\tilde{\beta}^{-4/5}$ versus simulated lower layer PV flux diffusivity ($\tilde{D}_l$), and (lower right) $(1-\tilde{\beta})^{3/2}\tilde{\beta}^{-2}$ versus simulated lower layer PV flux diffusivity ($\tilde{D}_l$). 131

4.6 The parameter dependence of the simulated bulk correlation coefficient and eddy velocity: the correlation coefficient between barotropic meridional velocity and baroclinic streamfunction ($c_\tau = D_\tau(V_\psi L_\tau)^{-1}$; left) and barotropic meridional velocity ($\tilde{V}_\psi$; right) plotted against $\tilde{\beta} = \beta k_d^2 U^{-1}$. 132

4.7 The scaling prediction by $0.4\tilde{V}_\psi^{3/2}\tilde{\beta}^{-1/2}$ versus simulated diffusivities: heat flux diffusivity ($\tilde{D}_\tau$; top), upper layer PV flux diffusivity ($\tilde{D}_u$; middle), and lower layer PV flux diffusivity ($\tilde{D}_l$; bottom). The constant 0.4 is arbitrarily chosen to shift all the data closer to the diagonal line. 133

5.1 The temperature structures in three climates: the radiative equilibrium (red), the MEP solution (dashed black), and the control simulation (solid black). Shown from left to right are (a) meridional profiles of the vertically averaged temperature, (b) meridional profiles of the lowest-level temperature, and (c) vertical profiles of the horizontally averaged temperature. 158

5.2 Simulated entropy destruction versus the prediction based on the vertical potential temperature difference in Eq. (5.13). The simulations with varying (a) Δ_y and (b) Ω are shown separately. The black solid dot denotes for the control climate. Its prediction by Eq. (5.13) is multiplied by a constant to ensure a perfect fit to the simulated value. The predictions for all other cases are then normalized by this constant accordingly. 159

5.3 A comparison of the entropy destruction in three climates: the numerical simulation (black) and the CMEP solution (dashed gray). Upper panels show the entropy destruction as a function of (a) Δ_y and (b) Ω, respectively. Lower panels plot the simulated entropy destruction versus the one computed from the CMEP solution for the varying (c) Δ_y and (d) Ω simulations, respectively. 160

5.4 As in Fig. 5.1, but for the control simulation (solid black) and its corresponding CMEP solution (dashed gray). 161

5.5 As in Fig. 5.3, but for the meridional temperature difference evaluated at the lowest model level ($\sigma = 0.98$) as the estimated value for the projected coefficient of the second Legendre polynomial. 162

6.1 A schematic plot of the before and after views with the numbered ovals indicating the corresponding chapters (see the "SUMMARY POINTS" text box). 173

6.2 As in Fig. 6.1, but for the illustration of how the core concepts described in "SUMMARY POINTS" fit together. 174

Chapter 1

Introduction

1.1 Motivation

Earth's atmosphere is a stratified fluid on a rotating sphere. Forced by differential radiative heating that varies with latitude, the mean flow of the extratropical troposphere constantly becomes baroclinically unstable and generates time and zonally varying motions. These motions are known as the transient eddies. They grow by consuming available potential energy in the mean flow, counteracting the energy refilled by the thermal forcing. The heat, momentum, and potential vorticity fluxes associated with these eddies continuously modify the mean flow, while the kinetic energies in both the eddies and the mean flow are meanwhile dissipated by surface friction. At a statistically steady state, the climate of the extratropical troposphere, as well as of the global atmosphere, is then largely determined by how the eddies equilibrate with the mean flow.

Since the maintenance of the climate mean state is such a fundamental problem, understanding the equilibration of these eddies has been a central topic in many earlier studies. Depending on how they view the nature of the equilibrated eddies, these studies are primarily divided into two schools. The first school of studies proposes

that the eddies, similar to thermal convection, can quickly adjust the mean flow so that the latter always remains approximately neutral to baroclinic instability and can only vary as a function of external parameters in such a way as to maintain this neutrality. It is thus usually referred as baroclinic adjustment theory (Smagorinsky 1963; Stone 1978a; Branscome 1983; Stone and Branscome 1992; Cehelsky and Tung 1991; Welch and Tung 1998). Because the mean state is at most weakly unstable in this picture, the equilibrated eddies are often assumed to have their scales and fluxes set by the linear characteristics of the baroclinic unstable modes. But more fundamentally, in this school of thought the approach is to create a theory for the mean climate directly, without requiring a detailed theory for the eddy fluxes. The latter have to adjust to the requirements imposed by the maintenance of the mean climate. From this broader perspective, the work on some variational-principle like arguments, such as the Maximum Entropy Production (MEP) theory (Lorenz 1960; Paltridge 1975, 1978) and Stone (1978b)'s hypothesis of outgoing longwave radiation being independent of latitude, also falls in this category.

Distinct from the first school, the second school of studies attempts to understand the equilibrated eddies from the perspective of geostrophic turbulence. It proposes that the equilibration of these eddies eventually involves the nonlinear interactions among the eddies themselves and not simply interactions with the mean flow. The quasigeostrophic nature of the extratropical troposphere makes these eddies quasi-horizontal. Similar to the two-dimensional turbulence, their kinetic energies cascade into larger spatial scales so that they no longer resemble the linear unstable modes (Rhines 1977; Salmon 1978, 1980). While turbulent flows are complex and unlikely to yield to complete theories, a simplification that emerges from these works, around which much of the theory has developed, is that the baroclinic component of the eddies can be thought as being stirred by the barotropic component, with the heat flux behaving like turbulent diffusion of a passive tracer (e.g. Haidvogel and Held 1980;

Pavan and Held 1996; Held 1999). In any case, as in other turbulence problems, the mean state is determined by and helps to determine these eddy fluxes, and, in general, their interactions are controlled by a complex dynamics varying among parameter regimes and among model systems of interest.

The views of the two schools seem contradictory, particularly on the freedom of the mean flow to vary with parameters. It is noted that the idea of baroclinic adjustment is first motivated by Smagorinsky (1963) and Stone (1978a)'s attempt to explain the observed mean isentropes in the extratropical troposphere. These mean isentropes are seen to rise from the surface in the subtropics to the polar tropopause, giving a slope which is consistent with the critical slope of baroclinic instability suggested by the linear theory in Phillips (1954)'s two-layer quasigeostrophic (QG) model. However, the fully nonlinear numerical simulations of these two-layer QG models actually show the equilibrated isentropes being steeper than this critical slope (e.g. Salmon 1980), posing a direct challenge to Smagorinsky (1963) and Stone (1978a)'s argument. While some modifications can be made to this adjustment theory hoping to explain these supercritical simulations (Cehelsky and Tung 1991; Welch and Tung 1998), a more serious issue with the concept of the critical slope is that it does not exist in the continuously stratified QG models (Charney and Stern 1962), which are presumably more realistic for representing the atmosphere. An example of an argument for why the two-layer model's critical isentropic slope is important in atmospheres with continuous stratification is that of Held (1978), who pointed out that this critical slope is required for the unstable modes to extend vertically throughout the troposphere in Charney (1947)'s model and argued that the eddy diffusivity will be a strong function of this parameter.

Adding more mysteries on the topic is the recent work by Schneider and colleagues. Schneider (2004) and Schneider and Walker (2006) investigated numerical simulations of an idealized primitive-equation general circulation model (GCM). They showed

the equilibrated isentropes stay robustly constant and close to two-layer critical slope in a range of Earth-like climates, agreeing well with Stone (1978a)'s observations. However, different from all the previous theories, they explained their results by a diffusive but non-QG argument and concluded that it leads to the same outcome of the eddies preferring to organize into a state with minimal self-interaction and weak baroclinic instability (Schneider and Walker 2006; O'Gorman and Schneider 2007; Schneider and Walker 2008; Merlis and Schneider 2009).

Complementing this work, Zurita-Gotor and colleagues studied both two-layer QG models and primitive-equation models, but in a broader parameter space. When they increased the strength of the thermal forcing sufficiently, they found that both models smoothly transit into states with supercritical isentropic slopes (Zurita-Gotor and Lindzen 2006; Zurita-Gotor 2007, 2008). They also found that no inherent distinction exists between the equilibration in the two classes of models, confirmed by comparing a two-layer QG model and two-level primitive-equation model with the former's static stability set to the same value as the latter's diagnosed mean stratification (Zurita-Gotor and Vallis 2009). This indicates that QG models, in spite of their inability to provide a theory for the static stability, are still relevant to more realistic models and the extratropical troposphere when combined with a non-QG theory for the static stability.

Consistent results are also presented by Jansen and Ferrari (2012, 2013a,b) using primitive-equation models with more vertical degrees of freedom. Their work is also motivated by the attempt to reconcile the similarities and differences between the extratropical atmosphere and the Antarctic Circumpolar Current (ACC). The latter is known to be baroclinically unstable with observations suggesting its eddies to be supercritical and kinetic energies going through substantial inverse cascade (e.g. Scott and Wang 2005; Tulloch et al. 2011). In the Jansen-Ferrari model, the ocean is effectively more strongly forced than the troposphere in the appropriate non-dimensional

sense, due to its smaller eddies. Therefore this can be a possible reason for the ACC to equilibrates more supercritically.

By virtue of these studies, a consensus has begun to emerge that baroclinic eddies in general can indeed equilibrate nonlinearly. Together, they suggest that the numerical findings of Schneider and earlier adjustment studies should be interpreted as mainly due to the limited parameter range explored. Also, the observations for Earth's extratropical troposphere merely confirm that its flow is located in a regime whose parameters happen to give a very weakly supercritical mean state. In other words, the stiffness of aspects of the mean flows in these cases, specifically the isentropic slopes, should not be taken as support of the linear adjustment theories nor an objection to the nonlinear perspective. Instead, we should expect that this stiffness is part of the solutions predicted by the geostrophic turbulence theory. We view this state of affairs as justifying continuing study of the geostrophic turbulence perspective.

Yet, we shall also emphasize that there is still lack of a satisfying, quantitative theory for eddy equilibration and the maintenance of the mean flows. In addition to discussing the criticality of the equilibrated mean flows, the studies by Zurita-Gotor, Jansen, and Ferrari have tried to explain the determination of the equilibrated states from the arguments of a particular QG turbulence theory. Despite the theory's ability to qualitatively predict the mean isentropic slope and the equilibrated eddies' parameter dependence, they also reported some quantitative differences between their simulations and the theory. This theory is based on a series of work by Held and colleagues, who studied the eddy scales and fluxes in a homogeneous QG two-layer model. The theory, following its predecessors (Rhines 1977; Salmon 1978, 1980), aims to determine the relations between the eddies and the mean flow using a series of assumptions and approximations (Larichev and Held 1995; Held and Larichev 1996; Lapeyre and Held 2003). As any of them can break down in different regimes and

different systems, it is therefore not surprising that the theory would not hold in general and require modification.

In fact, critical arguments against the theory of Held and colleagues have long existed in the literature. They have received more attention in the oceanic context due to the practical importance of the ocean mesoscale eddy parameterization problem (e.g. Smith and Vallis 2002; Thompson and Young 2006, 2007; Arbic and Scott 2008). While the baroclinic eddies in the extratropical atmosphere are pretty well simulated in the comprehensive global climate models nowadays, the baroclinic eddies in the ocean are on smaller scales referred as mesoscale that are generally not properly resolved, especially in ocean models that need to be integrated for centuries, and their effects still needed to be parameterized in the ocean component of these models (e.g. Hallberg 2013). For the development of the oceanic mesoscale eddy parameterization, there is hence a even more practical benefit from advancing the theoretical understanding of these eddies' scales and fluxes (e.g. Gent and Mcwilliams 1990; Visbeck et al. 1997; Cessi 2008; Jansen et al. 2015).

In addition to the parameterization problem of mesoscale ocean eddies, another line of inquiry on improving the theory comes from the recent exploration of the dynamics of planetary atmospheres. Due to the rapid developments of observational techniques, measurements on the other planets have become more available and it has been well known the planetary atmospheres span in a very wide range of climate regimes. A theoretical framework is then requested to better understand these different planetary climates. These include the climates that are likely involving the same baroclinic eddy dynamics seen on Earth. Therefore, a desire for a more quantitative theory on eddy equilibration emerges naturally (e.g. Chai et al. 2016; Kaspi and Showman 2015; Chemke and Kaspi 2015, 2016). Nonetheless, since all these studies are motivated somewhat differently for understanding different physical systems

and involve different models and parameter regimes, it is often hard to connect their theories, or even just their numerical findings, in a systematical way.

On the other hand, it is worth noted that all the research described above considers dry systems (or at least the dynamics they considered is essentially dry). Driven by an increasing computational power and a need to better predict anthropogenic climate change, the focus of much recent atmospheric research has shifted to the roles of moisture and how the eddies interact with various physical processes once the moisture is introduced (e.g. Juckes 2000; Frierson et al. 2006, 2007; O'Gorman 2011; O'Gorman et al. 2018). But to build a moist theory for eddy equilibration, a better dry theory has to be provided first so that we identify the complexities associated with the moisture and add them to the equilibration picture in a convincing way. Indeed, we seem to be going into a stage that we are unsure whether the questions we face are owing to the complexities associated with moisture or the complexities that are already there in the dry dynamics, so the research on models with different levels of complexities is demanded even more (e.g. Held 2005; Shaw et al. 2016).

With this background, it becomes apparent that there is a need to revisit and solidify our understanding of the dry problem, which is the motivation of this thesis. Following previous studies, this thesis places its particular focus on improving the QG turbulence theory proposed by Held and colleagues. Specifically, it aims to eliminate some of the gaps between the understanding of this theory and the understanding of its competing theories. In doing so, it seeks to also improve the understanding of how this theory fits into the bigger picture needed to understand baroclinic eddies in nature.

1.2 Overview

As we have explained in Section 1.1, eddy equilibration in the extratropical troposphere is a multidimensional problem. Given its fundamental importance to the theories for climate, many studies have tackled the problem from different perspectives. Given the turbulence nature of the subject itself, these studies are forced to develop their theories based on the numerical simulations of a certain model in a certain parameter regime. Meanwhile, each theory is formed by a number of assumptions. These together have led to a body of literature in which the individual theories are loosely connected.

This thesis engages with the existing literature by building upon the QG turbulence theory of Held and colleagues. In each chapter, we investigate a particular way to connect this theory to its competing theories. Attempts to reconcile with these theories, especially the apparently contradictory ones, would require a clarification of the relationships between the models on which they are based, of the parameter regimes they consider, and of the dynamics behind the assumptions they adopt. The dynamical issues will be introduced in detail in the individual chapters as the motivation for carrying out a particular investigation. Here, we provide an overview of the thesis by first describing the relations of the models and parameter regimes among all the theories addressed.

Fig. 1.1 maps out the thesis's basic structure and the relations of the theories that will be mainly considered. Each theory is referred by an acronym of the publication where it is proposed. The vertical axis indicates a hierarchy of models in different setups, with model complexity increasing when moving downward. Along this axis, each theory is placed align side of its corresponding model. The thesis includes four main chapters. Each of them is labeled with its chapter number, locating at a gap between the theories which the chapter attempts to fill.

Chapter 2 starts by comparing the theories of Held and Larichev (1996) and of Barry et al. (2002) for the meridional eddy heat fluxes and the mean thermal structure in the equilibrated states. The two theories share some assumptions that include a heat flux diffusivity scaling derived from the barotropic turbulence theory. They disagree on the thermodynamic budget, kinetic energy versus entropy, used to close the full theory. As the former is proposed for a homogeneous two-layer QG model and the latter is for a comprehensive GCM, we conduct a test on both theories in a model with intermediate complexity, i.e., an idealized GCM. We reconcile the two theories with a generalized expression for the thermodynamic budget involved and show that this expression explains a range of the simulated climates. Yet, we also point out that these simulations do not agree quantitatively with the barotropic QG scaling, consistent with previous studies' findings that the theory of Held and Larichev (1996) holds only qualitatively.

Motivated by the general difficulties in explaining the baroclinic systems by the barotropic theory, Chapter 3 goes back to reexamine the eddy scaling in the homogeneous two-layer QG models. To obtain a clean comparison to barotropic models, we consider a two-layer model with no background vorticity gradient, $\beta = 0$, which has symmetric equations and the same eddy statistics in its two layers. In this limit, the only physical parameter of interest is the strength of surface friction. We analyze how it controls the equilibrated eddy scales, fluxes, and energy spectra and identify their inconsistency with Held (1999)'s prediction for the dependence of heat flux on surface friction. Accordingly, we revise the theory of Larichev and Held (1995), which is the theoretical foundation of Held (1999), by heuristically modifying its assumption on the its barotropic energy spectrum to reconnect to the barotropic theory. In addition, we discuss how this revised theory is related to the theory of Thompson and Young (2006) for a similar system, which argued that a prevalence of vortices with baroclinic signatures make the barotropic theory irrelevant to this problem.

Chapter 4 extends the analysis in Chapter 3 to study the homogeneous two-layer QG model with an extra level of complexity, that is, with the presence of β. Thompson and Young (2007) reported that the barotropic theory also breaks down in the nonzero β cases. With the modified barotropic energy spectrum assumption, we develop a revised scaling argument for the two-layer model with nonzero β. It is built on the derivation of Kong and Jansen (2017) for the barotropic model, where the role of β in suppressing the meridional mixing due to zonal phase propagation of waves is emphasized. Instead, Lapeyre and Held (2003) argued the primary role of β is to introduce layer asymmetry that leads to distinct dynamics between the two layers and a different scaling. A comparison between the fits of the two scaling in the simulations is presented to address this discrepancy.

Given the complexities involved in these turbulence theories, Chapter 5 explores an entirely different approach to explain the maintenance of the climate mean states without explicitly thinking about eddy equilibration and its dynamics. The approach assumes that eddy dynamics is slave to some thermodynamic principle which describes some invariant aspects of the climate system. One candidate for such a principle is proposed by Paltridge (1975, 1978). He hypothesized that the equilibrated climate always maximize its entropy production. As the entropy budget of the idealized GCM has been examined in Chapter 2, we test this hypothesis in the idealized GCM to study whether it is reconcilable with our previous analysis according to the model dynamics. We demonstrate that the hypothetical state of maximum entropy production violates physical relations derived from dynamical consideration and is manifestly inconsistent with the model simulations. When the hypothetical state of local maximum entropy production is constrained by an aspect of the simulations, specifically the global mean vertical temperature profile, the results look superficially impressive. Yet, a closer examination shows that the variational calculation then adds no new information.

Hence, the approach may be compatible but is unlikely to be more economical than studying the dynamics itself.

Finally, Chapter 6 summarizes the overall findings and concludes by redefining the knowledge boundaries and possible directions for future work.

The research presented in this thesis is joint work with Isaac Held. Some results of Chapters 2 and 5 have been presented at the 21st Conference on Atmospheric and Oceanic Fluid Dynamics. Some results of Chapter 4 have been presented at the 22nd Conference on Atmospheric and Oceanic Fluid Dynamics. Chapter 3 has been published as Chang and Held (2019), and the rest of the work is currently in preparation for submission with Isaac Held.

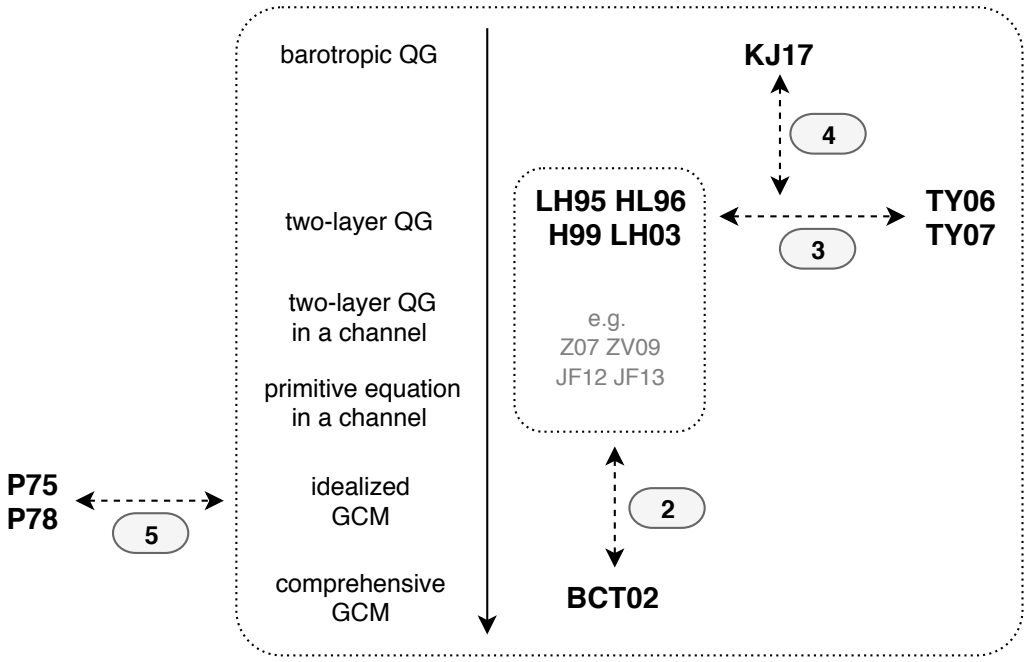

Figure 1.1: An overview of the relations between the chapters (indicated by the numbered ovals) and the addressed references (indicated by the acronyms). The acronyms stand for the following list of previous studies: Larichev and Held (1995, LH95), Held and Larichev (1996, HL96), Held (1999, H99), Lapeyre and Held (2003, LH03), Zurita-Gotor (2007, Z07), Zurita-Gotor and Vallis (2009, ZV09), Jansen and Ferrari (2012, JF12), Jansen and Ferrari (2013a, JF13), Barry et al. (2002, BCT02), Thompson and Young (2006, TY06), Thompson and Young (2007, TY07), Kong and Jansen (2017, KJ17), Paltridge (1975, P75), and Paltridge (1978, P78).

Chapter 2

Eddy equilibration in an idealized GCM: thermodynamic budgets and QG theory

This chapter examines how eddies equilibrate in an idealized GCM, a dry model on the sphere forced by simple radiative relaxation. Despite the idealization, this is the most realistic model studied in this thesis, raising many issues that remain unresolved. Thinking of the eddies as geostrophic turbulence and their meridional heat fluxes as turbulent diffusion, two theories that can relate the eddy heat flux diffusivity to the equilibrated thermal structure are tested in the model simulations.

2.1 Introduction

To develop a theory for the general circulation of the atmosphere, one fundamental problem that remains to be better understood is the determination of the large-scale poleward heat transport. From the Eulerian mean perspective, this transport can be regarded as carried by the mean meridional circulation and by the eddies deviating from the mean. For Earth's climate, the transport by stationary waves is of secondary

importance. It is rather the transient eddy heat fluxes that are directly related to the midlatitude baroclinic instability are of central concern, while the transient eddy momentum fluxes, which organize the mean meridional circulation that transports heat in an opposite direction in midlatitudes, is also of lesser importance. Being predominate, we focus on the transient eddy heat fluxes here. This heat flux is often thought as a turbulent diffusive process that transports heat down the equator-to-pole thermal gradient (Held 1999).

With the diffusion approximation of poleward eddy heat transport, one-dimensional energy balance models have been a popular tool to obtain the qualitative understanding of the changes of global climate due to the various types of forcing (e.g. North 1975). These models typically adopt a single value of diffusivity to represent, in some globally averaged sense, the effective eddy thermal diffusivity. It is recognized that this effective diffusivity leaves out the information encoded in the spatial structures that may be crucial in determining the actual detailed structure of the spatial variations of the heat flux (e.g. Green 1970; Zurita-Gotor 2008; Jansen and Ferrari 2013b; Yuval and Kaspi 2017). Such a globally averaged concept may be of limited value in some parameter ranges that requires a finer spatial investigation. Yet, this effective diffusivity is still a useful starting point to test our current theory for the underlying dynamics of poleward heat transport (e.g. Stone 1972; Frierson et al. 2007).

A theory for this type of effective diffusivity that seems particularly promising is proposed by Barry et al. (2002, hereafter BCT02). These authors explored a range of parameters of a comprehensive atmospheric-only global climate model. They found that, despite the rich physics and dynamics in their simulations, the simulated eddy heat fluxes over the parameter range considered are well explained by a relatively simple scaling theory that expresses the effective diffusivity in terms of the external parameters and the variables of the mean state. This chapter is in large part motivated

by the BCT02 study, which argues that their theory provides a much better fit to the comprehensive global climate model simulations than the previous theories.

To understand their theory, it is useful to divide it into four parts. The first part of the theory assumes the effective eddy heat flux diffusivity (D) can be estimated from a mixing length theory, i.e., $D \sim VL$, where V and L are the characteristic eddy velocity and length scale, respectively (the notation $A \sim B$ means A scales with B). It argues that, because kinetic energy cascades to larger scale in quasi-horizontal flows and because the cascade, as it affects meridional mixing, is typically halted by the β effect, L can be assumed to be the Rhines scale, $L_R \equiv (V/\beta)^{1/2}$ (Rhines 1975; Salmon 1978, 1980), where β is the meridional gradient of planetary vorticity. One can then obtain a scaling for the diffusivity given V,

$$D \sim V^{3/2}\beta^{-1/2}. \tag{2.1}$$

To determine V, the second part of the theory assumes that, because kinetic energy also cascades to the largest vertical scale, the heat transporting eddies are at the scale that contains most of the barotropic kinetic energy. Taking advantage of the classical two-dimensional turbulence theory, the barotropic energy spectrum is assumed to have a Kolmogorov's inertial range that is associated with an inverse energy cascade. Denoting the energy cascade rate, per unit mass, as ϵ with the unit $length^2 time^{-3}$ so that it scales as V^3L^{-1}, and with this cascade halted by β effect, one can derive a scaling for V,

$$V^2 \sim \epsilon^{4/5}\beta^{-2/5}, \tag{2.2}$$

via dimensional analysis. Eqs. (2.1) and (2.2) can be further combined to give

$$D \sim \epsilon^{3/5}\beta^{-4/5}.$$

While Eq. (2.1) provides an expression for the diffusivity given V, this expression provides the diffusivity given ϵ. The latter form is advantageous if ϵ is more easily determined than V using additional dynamical constraints.

The third part of the theory then tries to link ϵ to the entropy budget. This requires first of all that this energy cascade rate towards large scales can also be considered as the kinetic energy dissipation, with the kinetic energy dissipation at small scales being negligible. It also requires that the kinetic energy dissipation is the dominant entropy production term due to irreversible processes that balances the entropy destruction due to differential diabatic heating ($\dot{s}$). One can then write down

$$\epsilon \sim \dot{s} T_\epsilon, \tag{2.3}$$

where T_ϵ is the averaged temperature at which the dissipation occurs. It is noted that since this entropy budget argument apparently holds only as a global constraint, the relevant ϵ, V, L, and β should now all be regarded as some relevant globally averaged quantities as opposed to the local flow properties. This is self-consistent with a theory that is intended to provide an effective global diffusivity.

At this point, we are ready to relate $\dot{s}$ back to the mean state. For that, the fourth part of BCT02's theory uses a qualitative entropy budget which sets entropy destruction equal to a characteristic heating rate ($\mathcal{Q}$) times a characteristic temperature difference ($\Delta\mathcal{T}$) divided by the square of a characteristic temperature ($\mathcal{T}$), which they then approximate by

$$\dot{s} \sim \frac{\mathcal{Q}\Delta\mathcal{T}}{\mathcal{T}^2} \sim \frac{\bar{q}\partial_y \bar{T} a}{{T_0}^2}. \tag{2.4}$$

In the above equation, $\bar{q}$ is the mean column-integrated diabatic heating in the tropics (or cooling in high latitudes) and $\partial_y \bar{T}$ is the mean meridional temperature gradient in some globally averaged sense. Multiplying $\partial_y \bar{T}$ with the planetary radius a yields a representative of the bulk temperature difference between the averaged heating and

cooling regions, and T_0 can be thought of as the global mean atmospheric temperature. Assuming that neither T_ϵ nor T_0 are significantly parameter dependent, Eqs. (2.3) and (2.4) together provide an expression for ϵ in terms of $\bar{q}$ and the horizontal temperature gradient.

If large-scale eddies dominate the convergence of energy that balances $\bar{q}$, one can also write $\bar{q} \sim a^{-1}\mathcal{F}$, where $\mathcal{F}$ is the magnitude of the total heat transport. This transport, assumed to be mostly from its eddy component, can in turn be expressed in terms of the diffusivity D. While BCT02 does not present their theory in this way, the combination of Eqs. (2.3) and (2.4) then becomes another relation between ϵ and D that would need to be satisfied simultaneously with $D \sim \epsilon^{3/5}\beta^{-4/5}$ (i.e., the combination of Eqs. (2.1) and (2.2)) and ultimately gives a closure scaling for D in terms of β and the horizontal temperature gradient.

These four parts together form the diffusivity scaling theory developed by BCT02. An important result embedded in the first and second parts of BCT02's theory is that one can estimate the diffusivity for eddy heat fluxes and the eddy kinetic energy given the knowledge of kinetic energy dissipation. This had been proposed earlier by Held and Larichev (1996, hereafter HL96) in their more idealized study on a homogeneous two-layer quasigeostrophic (QG) model, based on essentially the same physical picture that the baroclinic streamfunction can be regarded as a passive tracer mixed by the barotropic flows where most energy is contained. Therefore, the novelty of BCT02's theory is in the third and fourth parts, in their approach for estimating ϵ.

As BCT02 emphasized, they have tested in their model simulations the ϵ expression given by HL96 and found that it performs inadequately compared to theirs. HL96's ϵ expression for a Boussinesq continuously stratified system, obtained from the available potential energy (APE) generation, can be written as

$$\epsilon \sim \frac{D(\partial_y \bar{b})^2}{N^2}, \tag{2.5}$$

where N^2 is Brunt-Vaisala frequency, $b = gT/T_0$ is the buoyancy, and g is the gravitational acceleration. Similar to the combination of Eqs. (2.3) and (2.4), Eq. (2.5) is itself a scaling relation between D and ϵ. Combined with $D \sim \epsilon^{3/5}\beta^{-4/5}$, it gives $D \sim \beta^{-2}\tau^{-3}$, where $\tau = N\partial_y \bar{b}^{-1}$ is the inverse Eady growth rate. This diffusivity expression is the closure form derived in HL96 (c.f. their Eq. (32)), which writes D in terms of β, the horizontal temperature gradient, and N^2. It is noteworthy that this APE expression for ϵ used in HL96 depends on the static stability (in N^2), while that of BCT02 does not. This is a potentially important simplification in BCT02, making it easier to apply the theory to a moist atmosphere where the appropriate choice of the static stability becomes an issue.

Given the above derivation, it is natural to speculate that the difference between the theories of BCT02 and HL96 arises from the thermodynamic budget they have used to estimate ϵ. However, it is also important to recall that the design of APE concept is related the entropy budget (Lorenz 1967). Indeed, Lapeyre and Held (2003, hereafter LH03) have discussed this issue. While the homogeneous two-layer QG model does not explicitly have a temperature variable, they derived an equivalent entropy budget for the model and showed that it results in essentially the same ϵ expression (i.e., Eq. (2.5)) as obtained from the APE budget. Given that BCT02 only provided a descriptive explanation for their derivation of Eq. (2.4), it is then mysterious why the two studies start from the same theoretical consideration but end up in different scaling expressions. It is also unclear why one performed better than the other in fitting BCT02's model simulations.

Since the comparison is between two theories which were verified using two different sets of model simulations whose parameters are not directly comparable, it is unclear how much of their differences has to do with 1) the inaccurate assumptions in the theories on the fundamental dynamics shared by both models, 2) the different natures of how the two models (a comprehensive global climate model and a homo-

geneous QG two-layer model) behave as parameters are varied, or 3) the different parameter ranges the model simulations represent. For example, one can suspect that the breakdown of HL96's theory in the BCT02's model simulations may be resulted from a more complicated model's extra dynamics and physics that are not considered in HL96's theory, while HL96's theory remain to be suitable for the homogeneous two-layer QG models (e.g. Zurita-Gotor 2007). Alternatively, HL96's theory has been questioned even in the context of homogeneous two-layer QG dynamics, for its relevance to broader parameter regimes (e.g. Thompson and Young 2007). A plausible way to reconcile the two theories can therefore be that they are applicable for different parameter regimes.

It is difficult to investigate all the differences between the two type of models and all the parameter regimes at once, so we do not aim to solve the whole problem. Instead, in this chapter, we hope to clarify some of these issues by studying a model with a level of complexity intermediate between the models BCT02 and HL96 have examined. Here, we choose to test these theories and explain their differences in a series of simulations of an idealized dry general circulation model ('idealized GCM' hereafter). This model has a primitive-equation spherical dynamical core and an idealized physical package described in Held and Suarez (1994). While there are many options in between the two-layer QG models and comprehensive GCMs, this idealized GCM helps isolate the complexities in the dry dynamics with zonally symmetrical forcing from the other complexities that are not involved in the theories described above, such as zonal inhomogeneity of boundary condition and physics of moist processes. Yet, unlike simpler models assuming QG, the model has temperatures and an unambiguous entropy budget. Additionally, the full spherical geometry and the greater freedom in vertical structures in the model are important differences with the homogeneous two-layer QG framework.

Another reason to study this model is that it appears to be a natural element of a model hierarchy that forms our understanding of the maintenance of climate by mid-latitude eddy dynamics. Since it was first introduced, various aspects of this model and its close relatives have been investigated, especially as to how the equilibrated thermal structure is determined (e.g. Schneider and Walker 2006; Zurita-Gotor 2008; Chai and Vallis 2014). Because the model's diabatic heating is in the form of Newtonian relaxation, the thermal structure is very simply related to the heat transport, the focus of this study. Therefore, as a contribution to the existing literature on this model, we believe it is worthwhile to document its behavior focusing on how it differs or resembles the results and theories in HL96 and BCT02.

The rest of the chapter is organized in the following way. The details of the model and the simulations examined are described in Section 2.2. In Section 2.3, we derive a generalized scaling relation that can potentially reconcile Eqs. (2.4) and (2.5) in this model, and we explain that Eqs. (2.4) and (2.5) are two limits of this generalized expression. In Section 2.4, this generalized scaling relation and the other assumptions in the theories, i.e., Eqs. (2.1)-(2.3), are validated individually in the simulations with varying Δ_y, which is a model parameter controlling the equator-to-pole temperature difference at radiative equilibrium (defined later on in Section 2.2). Because there is no direct analog of Δ_y in BCT02's model results, we also study in Section 2.5 another set of the simulations with varying planetary rotation rate (Ω), which is precisely defined in both models and is examined by BCT02. In Section 2.6, we then assess the overall performance of the general diffusivity theory combining all these assumptions. We compare the errors introduced by each assumption on the estimate of diffusivity and present the final result in the closure form of the theory. Finally, we conclude by discussing the implications of our findings and some open questions in Section 2.7.

2.2 The idealized GCM and the numerical simulations

We conduct our numerical simulations using the GFDL FMS idealized global spectral atmospheric model. Its dynamical core solves for the primitive equations on the spherical coordinate with no surface topography, and it is run at T85 and T213 resolutions with 30 equally spaced σ levels in the vertical (where σ is the model's vertical coordinate defined as the ratio of the pressure at a given level and the surface pressure). This model's physics are kept highly idealized (Held and Suarez 1994). The only diabatic heating Q is parameterized as Newtonian relaxation that damps the temperature T back to the prescribed radiative equilibrium value T_{eq}, i.e.,

$$Q = -c_p k_T \left(T - T_{eq}\right),$$

where k_T is the inverse of diabatic forcing timescale and c_p is the specific heat capacity at a constant pressure. The standard setting for T_{eq} is

$$T_{eq} = max\left\{200K, [315K - \Delta_y \sin^2\phi - \Delta_z log(p/p_0)\cos^2\phi](p/p_0)^{\kappa}\right\},$$

where p is pressure, $\kappa = R/c_p$, and R is the ideal gas constant. The constants are chosen as $p_0 = 1000\ hPa$, $\Delta_y = 60\ K$, and $\Delta_z = 10\ K$. Thus, the radiative equilibrium state is statically stable in the tropics and slowly approaches to neutral in the extratropics. Any further stabilization is caused by the large-scale dynamics. In addition, k_T is defined as

$$k_T = k_a + (k_s - k_a) max\left(0, \frac{\sigma - \sigma_b}{1 - \sigma_b}\right)\cos^4\phi,$$

where $\sigma_b = 0.7$, $k_a^{-1} = 40\ days$, and $k_s^{-1} = 4\ days$. The uniform and relatively long timescale in the free troposphere k_a is designed to represent radiative cooling, while a shorter timescale k_s imposed in the nominal boundary layer ($\sigma \leq \sigma_b$) is to mimic the surface heat fluxes. There is no diurnal or seasonal cycle in diabatic heating, and both the radiative equilibrium and the steady state climates are zonally symmetric. A Rayleigh drag is implemented in the boundary layer to account for the effect of bottom friction. For numerical stability, ∇^8 hyperdiffusion is also operated on horizontal momentum (vorticity and divergence) and temperature fields in the model. In order to conserve global energy, Rayleigh frictional heating is directly added back to the local temperature budget, and any other energy loss are compensated by a spatially uniform temperature correction at each model time step.

We refer the simulation with the standard setting in Held and Suarez (1994) as our control simulation. Two series of simulations where we individually vary the meridional temperature gradient at radiative equilibrium (Δ_y introduced above; from 10 K to 180 K) and planetary rotation rate (Ω; from 0.25 to 7 times the Earths rotation rate (Ω_e)) are examined. The former is run at T85 resolution. The latter is run at T213 resolution (with an associated control simulation at T213 resolution), due to the reduction in eddy size with increasing Ω. All the diagnostics presented are calculated from the last 1000 days in a 1500-day integration. As discussed in Section 2.1, this study's main interest is the effective diffusivity (D) that can represent some globally averaged eddy poleward heat transport. To this end, we calculate D in the following analysis as the hemispherically averaged column-integrated meridional eddy dry static energy flux divided by hemispherically averaged column-integrated mean meridional dry static energy gradient. The hemispherical average is performed with surface area weighting. The column mass-weighted integration is taken from $\sigma = 0.2$ to $\sigma = 1$. While the details of this choice of averaging is somewhat arbitrary, we note that they are of modest importance for the interpretation of our results, in part

because the temperature gradient and the heat flux are both largest in midlatitudes, so these global means primarily reflect midlatitude values. To be consistent with this D's working definition, other variables will also be mostly calculated as some spatial average. We define them later on whenever they become directly relevant to the discussion.

2.3 A generalized thermodynamic relation for the idealized GCM

In this section, we reconcile the different metrics for entropy destruction proposed in BCT02 and HL96, i.e., Eqs. (2.4) and (2.5), by showing that they are both an approximation of a more general form. We begin with the theoretical derivation for this generalized relation to replace Eqs. (2.4) and (2.5), and then we describe the way we diagnose this relation in the model simulations.

Following Held (2007), we reformulate the global entropy destruction in a flux-times-gradient form through an integration by parts. Written in the Cartesian coordinate for simplicity, this is

$$\begin{aligned} M\dot{s} &\equiv -\int \frac{\overline{\rho Q}}{\bar{T}} dV \\ &= -\int \frac{\nabla \cdot \overline{\rho \mathbf{F}}}{\bar{T}} dV \\ &= \int \overline{\rho \mathbf{F}} \cdot \nabla \left(\frac{1}{\bar{T}} \right) dV \\ &= -\int \frac{\overline{\rho F}_y}{\bar{T}} \left. \frac{\partial \ln \bar{T}}{\partial y} \right|_m dV, \end{aligned} \tag{2.6}$$

where M is total mass, V is volume, and ρ is density. $\bar{Q}$ is the mean nondissipative diabatic heating rate (which is simply the radiative relaxation defined in Section 2.2 for this model). $\overline{\rho \mathbf{F}} \equiv \overline{\rho F}_y \hat{y} + \overline{\rho F}_z \hat{z}$ is a vector quantity representing the mean

adiabatic heat flux, and it is related to heating via $\overline{\rho Q} = \nabla \cdot \overline{\rho \mathbf{F}}$. m denotes the vertical coordinate on the sloping surface along which $\overline{\rho \mathbf{F}}$ is aligned. The normalized temperature gradient along this surface can be expressed as

$$\begin{aligned}
\left.\frac{\partial \ln \bar{T}}{\partial y}\right|_m &= \left.\frac{\partial \ln \bar{T}}{\partial y}\right|_p + \left.\frac{\partial \ln \bar{T}}{\partial \ln p}\,\frac{\partial \ln \bar{p}}{\partial y}\right|_m \\
&= \left.\frac{\partial \ln \bar{T}}{\partial y}\right|_p + \left.\frac{\partial \ln \bar{T}}{\partial \ln p}\xi\frac{\partial \ln \bar{p}}{\partial y}\right|_\theta \\
&= \left.\frac{\partial \ln \bar{T}}{\partial y}\right|_p + \left(\frac{\partial \ln \bar{\theta}}{\partial \ln p} + \kappa\right)(-\xi)\left.\frac{\partial \ln \bar{\theta}}{\partial y}\right|_p \left(\frac{\partial \ln \bar{\theta}}{\partial \ln p}\right)^{-1} \\
&\approx \left.\frac{\partial \ln \bar{T}}{\partial y}\right|_p \left(1 - \xi + \xi\left(\frac{N_0^2}{N^2}\right)\right) \\
&\approx \left.\frac{\partial \ln \bar{T}}{\partial y}\right|_p (1-\xi) + \xi\kappa\left.\frac{\partial \ln \bar{p}}{\partial y}\right|_\theta,
\end{aligned} \tag{2.7}$$

where

$$\xi \equiv \left.\frac{\partial \ln \bar{p}}{\partial y}\right|_m \left(\left.\frac{\partial \ln \bar{p}}{\partial y}\right|_\theta\right)^{-1} \tag{2.8}$$

is the ratio of mixing slope and isentropic slope in the meridional-vertical $(y-p)$ plane and $N_0^2 = (gT_0)^{-1}(g/c_p)$ is N^2 for the dry adiabatic processes. The last two expressions use the approximation $\partial_y ln\bar{T}|_p \approx \partial_y ln\bar{\theta}|_p$.

In the presence of spatial inhomogeneity, the rhs value of Eq. (2.6) depends on the details of the mean thermal structure and heat flux's spatial distribution. For this expression to be useful for the type of global scaling relations that we are hoping for, we need to further assume that it can be written in terms of characteristic domain averages,

$$\dot{s} \sim \frac{-1}{\bar{T}}\left(\int \bar{F}_y \frac{\rho dV}{M}\right)\left(\left.\frac{\partial \ln \bar{T}}{\partial y}\right|_m\right) \sim \frac{-\mathcal{F}\mathcal{M}}{T_0}, \tag{2.9}$$

where $\bar{T} \sim T_0$ is approximately constant, $\mathcal{F}$ is the estimate of characteristic heat flux (in the unit of $length^3 time^{-3}$) and $\mathcal{M}$ is the estimate of characteristic $\partial_y ln\bar{T}|_m$ in Eq. (2.7) (in the unit of $length^{-1}$). We show below that Eqs. (2.4) and (2.5) can

be thought as two distinct approximations on Eq. (2.9) with different assumptions concerning $\mathcal{F}$ and $\mathcal{M}$.

To reduce Eq. (2.9) to LH96's scaling, i.e., Eq. (2.5), we can take $\mathcal{F} \sim -c_p D \partial_y \bar{T}$. This is exact as the total heat flux equals to eddy heat flux in the homogeneous two-layer QG models analyzed in HL96. Second, we take $\xi = 1$ in Eq. (2.7) for estimating $\mathcal{M}$, which is again exact as the eddy heat fluxes are adiabatic in that model and thus they are always aligned with the mean isentropic surface. Together with $\partial_y ln\bar{T}|_p \approx \partial_y ln\bar{\theta}|_p$, we then recover Eq. (2.5) or equivalently

$$\dot{s} \sim -\frac{\mathcal{F}}{T_0}\frac{N_0^2}{N^2}\left.\frac{\partial \ln \bar{T}}{\partial y}\right|_p \sim -\frac{\mathcal{F}}{T_0}\kappa\left.\frac{\partial \ln \bar{p}}{\partial y}\right|_\theta . \tag{2.10}$$

Likewise, to reduce Eq. (2.9) to BCT02's scaling, i.e., Eq.(2.4), we use the relation $\mathcal{F} \sim \bar{q}a$ that is discussed in Section 2.1 and assume $\xi = 0$ in Eq. (2.7) for estimating $\mathcal{M}$. This gives us Eq. (2.4) or equivalently

$$\dot{s} \sim -\frac{\mathcal{F}}{T_0}\left.\frac{\partial \ln \bar{T}}{\partial y}\right|_p . \tag{2.11}$$

The physical interpretation of Eq. (2.11) is worth more elaboration. It is tempting to take Eq. (2.11) as a result of the heat flux being completely horizontally-oriented (as implicitly assumed in BCT02's argument) and the effective mixing direction being horizontal ($m = p$). However, no vertical heat flux requires no potential-to-kinetic energy conversion. $\mathcal{M}$ has to be at least along some sloping surface and ξ can never be exactly zero. Eq. (2.11) is therefore better interpreted as an approximation when the change in $\mathcal{M}$ with the parameters is by and large proportional to the change in mean temperature gradient. That is, in Eq. (2.7), either ξ is nonzero but small, or ξ is nonnegligible but the factor $(1 - \xi + \xi(N_0^2/N^2))$ compared with $\partial_y ln\bar{T}|_p \approx \partial_y ln\bar{\theta}|_p$ stays relatively unchanged with the parameters.

This reformulation also reveals the key difference between Eqs. (2.10) and (2.11) (and thus Eqs. (2.4) and (2.5)). It is clearly seen that Eq. (2.10) has an extra (dimensionless) factor N_0^2/N^2 that depends on the mean static stability. It is with this mean static stability dependence Eq. (2.10) can be written in terms of the mean isentropic slope. It is effectively through $\mathcal{M}$ in Eq. (2.9) that the static stability becomes involved in HL96's diffusivity theory. (Strictly speaking, this only refers to the turbulence part of HL96's theory. We note that HL96 also obtained the same diffusivity closure via a quasi-linear argument (c.f. their Section 5), where the static stability is introduced by the deformation radius and the energy equipartition relation). In contrast, the static stability makes no explicit appearance in Eq. (2.11) and BCT02's theory, distinguishing itself from most other classic diffusivity theories that have various ways of static stability dependence (e.g. Green 1970; Stone 1972).

The above theoretical consideration provides insights in understanding the differences between the two theories. Yet, there are practical issues to validate these equations with the numerical simulations. To rewrite Eq. (2.6) the exact equation to Eq. (2.9) the more workable scaling relation, the spatial structures of the involved variables are assumed to be unimportant. Fig. 2.1 shows the spatial distributions of mean isentropes (contours) and mean diabatic heating (shading) for the control simulation. It exemplifies the complex nature of the idealized GCM in its mean thermal structure. By looking at it, there appears to be no clear way on how best to perform a proper diagnosis of $\mathcal{F}$ and $\mathcal{M}$ in Eq. (2.9) to ensure an adequate representation of the physics behind Eqs. (2.6)-(2.8).

Upon some trial and error, we have managed to find a somewhat arbitrary approach that can demonstrate the qualitative differences in Eq. (2.9)'s performance due to different $\mathcal{M}$ approximations to explain our simulations. We first disclose that in allowing Eq. (2.9) to be easily related back to D defined in Section 2.2, a choice of $\mathcal{F}$ is ideally the hemispherically averaged column-integrated eddy meridional dry

static energy flux used to define D. On the other hand, it is in theory the convergence of total flux that balance the diabatic heating. For now, we compute $\mathcal{F}$ as the total rather than eddy flux and assess the consequences of this extra approximation in Section 2.6.1. With this working definition of $\mathcal{F}$, we choose to quantify the locations of domain averaged heating and cooling using their centroids. Suppose ϕ_h (ϕ_c) and σ_h (σ_c) denote the latitude and σ level at the centroid of heating (cooling), they are computed as

$$\phi_h = \frac{\left[max\left(\bar{Q},0\right)\phi\right]}{\left[max\left(\bar{Q},0\right)\right]} \qquad \sigma_h = \frac{\left[max\left(\bar{Q},0\right)\sigma\right]}{\left[max\left(\bar{Q},0\right)\right]}$$
$$\phi_c = \frac{\left[min\left(\bar{Q},0\right)\phi\right]}{\left[min\left(\bar{Q},0\right)\right]} \qquad \sigma_c = \frac{\left[min\left(\bar{Q},0\right)\sigma\right]}{\left[min\left(\bar{Q},0\right)\right]}$$

where [ ] denotes for the mass-weighted integral over one hemisphere. Expecting that most of the heat transport is confined in the region bounded by the heating and cooling centroids, we define a bulk mixing surface (denoted as $\tilde{m}$) with the bulk mixing slope

$$\left.\frac{\partial \ln \bar{p}}{\partial y}\right|_{\tilde{m}} \equiv \frac{(\sigma_c - \sigma_h)}{a(\phi_c - \phi_h)}$$

and a bulk isentropic slope (denoted as $\tilde{\theta}$)

$$\left.\frac{\partial \ln \bar{p}}{\partial y}\right|_{\tilde{\theta}} \equiv \frac{\bar{\theta}\left(\phi_c,\sigma_c\right) + \bar{\theta}\left(\phi_c,\sigma_h\right) - \bar{\theta}\left(\phi_h,\sigma_c\right) - \bar{\theta}\left(\phi_h,\sigma_h\right)}{\bar{\theta}\left(\phi_c,\sigma_c\right) + \bar{\theta}\left(\phi_h,\sigma_c\right) - \bar{\theta}\left(\phi_c,\sigma_h\right) - \bar{\theta}\left(\phi_h,\sigma_h\right)} \left.\frac{\partial \ln \bar{p}}{\partial y}\right|_{\tilde{m}}.$$

Hence, an estimate of ξ using Eq. (2.8) (denoted as $\tilde{\xi}$) can be obtained accordingly. With this, we then estimate $\mathcal{M}$ using the last form of Eq. (2.7) with $\partial_y ln\bar{T}|_p \sim T_0^{-1}\partial_y \bar{T}$ calculated as the hemispherically averaged column-integrated mean meridional dry static energy gradient (i.e., the one used to define D in Section 2.2). We note that nowhere in these calculations do we invoke a diagnosis on N^2 directly.

As an example, we here perform these calculations for the control simulation. Given its spatial distribution of the mean diabatic heating, we calculate its centroid of heating and its centroid of cooling accordingly, which are indicated as the black dots in Fig. 2.1. The dashed line that links the centroids is the identified bulk mixing surface. Compared with the mean isentropic surface shown as the contours, it is relatively flat and gives a diagnosed $\tilde{\xi} \approx 0.4$. If taken seriously, this suggests the control simulation falls in a regime where neither Eqs. (2.10) nor (2.11) is particularly applicable.

If one ignores the centroids and simply looking at the heating distribution and the isentropic surfaces in Fig. 2.1, one is more likely to guess the effective mixing slope is not much different from the isentropic slope and a better estimate would be $\xi \approx 1$. Apparently, the discrepancy arises from the fact that the heating and cooling centroids do not collocate with the heating and cooling maxima. The heating is present in the whole tropical column even though it is mostly concentrated in the boundary layer where the inverse diabatic damping timescale (k_T) is large (Section 2.2). By contrast, the cooling spreads out more uniformly and is only slightly stronger in the extratropical upper troposphere. Hence, the contribution from the regions other than the local maximum is nonnegligible after weighted by their mass, leading to a distinction between the maximum and the centroid.

We have also tried to calculate the local mixing surface directly from the ratio of the local vertical and meridional heat flux, but the local ξ defined varies strongly in space. From the perspective of local eddy potential temperature variance budget, the statistically steady state local ξ can deviate from the mean isentropic slope in the presence of thermal damping on eddies (i.e., the temporal correlation between diabatic heating and potential temperature) or the horizontal and vertical transports of the eddy potential temperature variance. We found the former is often relatively small and the latter is crucial in shaping the spatial pattern of local ξ. Considering

that the latter vanishes in the global budget, the relevance of the local ξ to the global ξ of interest here is thus unclear (compared to the context of homogeneous two-layer QG). With these uncertainties, we cannot tell a priori whether Eqs. (2.10) and (2.11) would give a better prediction directly from the diagnosed $\tilde{\xi}$. Instead, we will evaluate Eqs. (2.10) and (2.11) based on their ability to explain the changes with the model parameters, as done for the other scaling relations discussed in the other parts of the theories. As we will show in the next sections, the calculations based on this approach can still be useful from this perspective.

2.4 Validating individual scaling relations: varying Δ_y simulations

We begin to test the scaling relations introduced so far by looking at the simulations where we vary Δ_y. As in Section 2.1, we divide the theories into four parts and evaluate these scaling relations separately. For these varying Δ_y simulations, we show that while there are some practical differences in the interpretation of Eqs. (2.1)-(2.3) between BCT02 and HL96, they are all subtle and relatively insignificant. Instead, the most significant differences are in the last part, i.e., Eqs. (2.9)-(2.11). We show that BCT02's scaling breaks down but the generalized scaling remain useful in explaining these simulations.

2.4.1 Relating diffusivity to kinetic energy level

To determine how well the simulated eddy heat flux diffusivity (D) is explained by the simulated eddy velocity (V) using Eq. (2.1), we loosely follow BCT02 to calculate V from the square root of globally averaged total eddy kinetic energy ($V_t^2 \equiv$ EKE) and $\beta \equiv 2\Omega a^{-1} cos\phi_E$ at the latitude of the EKE centroid (ϕ_E). Based on these working definitions, we plot the simulated D against Eq. (2.1)'s prediction in the top panel of

Fig. 2.2, with one filled circle denoting for one simulation and the black dot denoting the control simulation. To ensure the prediction is perfect for the control simulation (i.e., the black dot falls on the diagonal line), all the predicted values are normalized by the same constant accordingly. The control simulation's diffusivity is on the order of $10^6\ m^2 s^{-1}$, which is a typical value used in diffusive energy balance models (e.g. North 1975). As we vary the parameters, D is seen to increase with Δ_y monotonically throughout the explored parameter range, and its changes with Δ_y are well explained by Eq. (2.1).

This nice fit by Eq. (2.1) is aligned with BCT02's results, where they also used the total eddy kinetic energy in defining V. Yet, in the two-layer QG simulations of HL96 and LH03, it is the square root of barotropic rather than total eddy kinetic energy that is considered. Since the baroclinic velocity and the temperature (the interface height) in that model are in quadrature in longitude, baroclinic flow produces no net transport. This reasoning is specific to the two-layer QG model, and its relevance to other systems, such as the idealized GCM considered here, is unclear. It is of interest to see how different expressions for V in this expression affect the results, so we have computed another set of predictions based on the squared root of globally averaged barotropic eddy kinetic energy (V_b^2; the barotropic mode is defined as the average between $\sigma = 0.2$ to $\sigma = 1$). These new results are shown in the top panel of Fig. 2.2 by open circles, which look very similar to the ones based on V_t (the filled circles).

However, the similarity in the results using these two definitions of V is not due to V_b being close to V_t, as one would expect for strongly unstable flows in which most of the kinetic energy has cascaded to and is stored in the barotropic mode. In the control simulation, barotropic and baroclinic eddy kinetic energies contribute about equally to the total eddy kinetic energy. When we vary Δ_y, the two energies change proportionally, so the predictions based on V_b and V_t scale similarly. Hence, the predictions from the two velocity scales are barely distinguishable in these simulations,

at least in these log-log plots aimed at defining scaling relations. The intimate relation between diffusivity and eddy kinetic energy level described by Eq. (2.1) is then supported with either definition. Taking advantages of its simplicity, we then retain the use of total eddy kinetic energy (i.e., EKE= V_t^2) as in BCT02 in the following analysis, but we also caution that there is no specific reason to assume that the two eddy velocities would always give qualitatively similar diffusivity predictions.

2.4.2 Relating kinetic energy level to the rate of kinetic energy dissipation

Having checked Eq. (2.1), we next test Eq. (2.2), the relation between kinetic energy level (V^2) to the strength of the kinetic energy cycle (ϵ). In the middle panel of Fig. 2.2, we plot the simulated EKE (V_t^2) against its corresponding prediction by Eq. (2.2), with ϵ calculated as globally averaged total kinetic energy dissipation (ϵ_d). It is seen that in these simulations, EKE increases with Δ_y and is well predicted by Eq. (2.2). This scaling relation, based on the assumption on the barotropic inverse cascade and Kolmogorov's inertial range theory (Section 2.1), seems to work straightforwardly here. Nevertheless, as we will show in Section 2.5, it may become a crucial problem when applying to the varying Ω simulations.

2.4.3 Estimating kinetic energy dissipation from entropy and kinetic energy budgets

We now shift our focus to Eq. (2.3), which is the assumption that links the kinetic energy dissipation (ϵ_d) to the global entropy budget in BCT02. This assumption is the step that BCT02 argued is distinctive compared to HL96's theory which uses the global APE or kinetic energy budget to quantify ϵ_d instead. However, LH03 has found that this argument is not convincing by showing that APE and kinetic energy

budget is essentially the entropy budget for the two-layer QG models. The idealized GCM considered here has an unambiguous entropy budget, providing an opportunity to address this issue.

For this purpose, in the bottom panel of Fig. 2.2, we plot the simulated ϵ_d against two different predictions based on the dominant term that balances it in the entropy and kinetic energy budgets. The first set of predictions scales ϵ_d to the globally averaged entropy destruction rate ($\dot{s}$; filled circles) in the entropy budget, that is, Eq. (2.3) with the assumption $T_\epsilon \sim T_0$ as a constant. The second set of predictions is calculated from the globally averaged conversion rate from eddy APE to EKE (ϵ_p; open circles) in the kinetic energy budget. We note that ϵ_d by definition equals the total energy conversion, in the eddies and in the zonal mean. However, the zonal energy conversion is zero in the homogeneous two-layer QG models to which we hope to make contact through the theory of HL96. Therefore, it is of interest to see the implications of focusing only on the eddy production in the analysis of the idealized GCM.

Similar to the simulated EKE in the middle panel of Fig. 2.2, the bottom panel of Fig. 2.2 shows that the simulated ϵ_d increases with Δ_y. We also see that the two sets of predictions are comparable in their accuracy in explaining the parameter dependence. They both capture the increasing trend of ϵ_d with Δ_y, but both very slightly overestimate the sensitivity to Δ_y. By construction, these prediction errors must come from the neglected terms in these budgets. To get a better idea on how they emerge, we have explicitly calculated and examined the simulated entropy and kinetic energy budgets (results shown in Appendix 2A). In the entropy budget, entropy production is not only due to frictional dissipative heating in the idealized GCM. The other entropy source term, diabatic entropy production due to eddy thermal damping, are found to be nonnegligible as well. Therefore, $\dot{s}$ (total entropy destruction) is only a crude approximation of entropy production due to frictional dissipative heating. In addition,

for the latter to scale with ϵ_d, T_ϵ should be mostly independent of the parameters. This implicit assumption is not satisfied in the simulations, either. Relatively, the changes in T_ϵ contributes little to the total errors, and it is mostly the presence of additional entropy sources that causes Eq. (2.3) to be inprecise. As for the mismatch between ϵ_d and ϵ_p, it is due to the considerable contribution of energy conversion from zonal APE to zonal kinetic energy in the kinetic energy budget. Although small, this term is seen to change from positive to negative when Δ_y increases, resulting in ϵ_p to overestimate ϵ_d's sensitivity to Δ_y.

2.4.4 Relating entropy destruction to the mean thermal structure

Together, Fig. 2.2 summarizes the fits of Eqs. (2.1)-(2.3) in the varying Δ_y simulations. These results suggest that none of these scaling relations seems to be seriously violated and sensitive to the different interpretations in BCT02 and HL96. It leaves the last part of the theories as the only potential distinction between the two theories. That is, how to relate $\dot{s}$ back to the mean thermal structure. In Fig. 2.3, we show three $\dot{s}$ estimates from Eqs. (2.9)-(2.11) using the working definitions described in Section 2.3. The first is the benchmark calculation with ξ estimated as $\tilde{\xi}$ from each simulation (colored filled circles), representing the highest possible accuracy of these diagnoses. It fits very well in these simulations. Overall, we interpret this result as reasonable enough, given all the uncertainties that one can think of in these diagnoses.

The other two estimates are to test Eq. (2.10) (black open circles) and Eq. (2.11) (colored open circles). As explained in Section 2.3, Eq. (2.10) is equivalent to Eq. (2.5), i.e., HL96's scaling. Its predictions fit well in the simulations except for a slight loss of accuracy when Δ_y is larger than the control simulation. On the other hand, Eq. (2.11) is equivalent to Eq. (2.4), i.e., BCT02's scaling, and it systematically overestimates the sensitivity of $\dot{s}$ to Δ_y. This oversensitivity can be understood

from the observed constant isentropic slope and the increased meridional temperature gradient when Δ_y increases (Schneider and Walker 2006; Zurita-Gotor 2008). Since Eq. (2.10) explicitly depends on the isentropic slope and fits well to the simulations, Eq. (2.11) which depends on the meridional temperature gradient must become oversensitive to Δ_y.

The finding here is a key result of this study. It presents a vivid counterexample to BCT02's argument, as HL96's scaling better explains these simulations than that of BCT02. In fact, we have argued that neither should work for all the simulations as they are based on approximations to Eq. (2.9) that are not expected to be of general validity. To further support this point, we show the results of the varying Ω simulations in the next section, where this time it is rather BCT02's scaling that performs better than HL96's one as argued by BCT02.

2.5 Validating individual scaling relations: varying Ω simulations

BCT02 showed that their theory explains their comprehensive GCM simulations with Ω increases from the Earth's one (Ω_e) to about twice the value. To check whether our model behave in the same way, we conduct a set of the simulations where we vary Ω as well. We also explore a larger Ω range (from 0.25Ω to 7Ω) to study the extent to which their theory holds so that we can better convey its limitation.

Similar to Fig. 2.3, Fig. 2.4 shows the simulated $\dot{s}$ plotted against the predictions by Eqs. (2.9)-(2.11). We first note that the simulated $\dot{s}$ decreases as Ω increases, but with a moderate change compared to the one for varying Δ_y. Partly due to this insensitivity, it is more difficult for Eq. (2.9) to predict the simulated $\dot{s}$ as accurate as seen in Fig. 2.3. In general, Eq. (2.9) still explains the simulations reasonably well and remains as the best fit among the three predictions. By contrast, Eq. (2.10)

overestimates the sensitivity of $\dot{s}$ to Ω. This suggests the temperature gradient along the mixing surface varies in a way differs from the one along the isentropic surface, so HL96's scaling would not work in these simulations. Relatively speaking, Eq. (2.11), the equivalence of BCT02's scaling, better predicts the simulations instead. It is especially useful for the cases with Ω close to Ω_e, indicating the temperature gradient along the mixing surface in these cases can be well approximated by the meridional temperature gradient. These results are therefore broadly consistent with the results of BCT02, who showed that their scaling indeed outperforms HL96's one in this specific range of Ω. We also confirm that their scaling remains as an approximation whose precision quickly drops once Ω becomes much larger or smaller than Ω_e. They then lead to the same conclusion drawn from the varying Δ_y simulations.

Unlike the above results for Eqs. (2.9)-(2.11), the varying Ω simulations can however encode very different information from the varying Δ_y simulations about the validity of Eqs. (2.1)-(2.3). Similar to Fig. 2.2, Fig. 2.5 shows how well these scaling relations predict the varying Ω simulations. In these simulations, the diffusivity D decreases as Ω increases. This is still consistent with Eq. (2.1) irrespective of the velocity definition one chooses (although the ratio between V_t and V_b is no longer constant). It is particularly impressive that this Rhines scale fit works for smaller as well as larger Ω.

Yet, Eqs. (2.2) and (2.3) are clearly seen to break down in the cases with Ω smaller than Ω_e, where they even fail to explain the increases of EKE and ϵ_d with increasing Ω in this parameter range. Actually, within the full Ω range we explore, EKE and ϵ_d changes nonmonotonically with Ω and have their maxima at a Ω slightly smaller than Ω_e. On the other hand, both $\dot{s}$ and ϵ_p monotonically decrease as Ω increases, so Eq. (2.3) with either of them is obviously inapplicable to the smaller Ω cases. For Eq. (2.2), it is noted that β depends explicitly on Ω. Thus, although ϵ_d can

potentially capture EKE's nonmonotonic dependence, the dominance of β makes Eq. (2.2) predicts a monotonic decrease of EKE with increasing Ω.

The breakdown of Eq. (2.3) can be attributed to the discrepancy in the various budget terms as discussed for the varying Δ_y simulations (Section 2.4.3). Nonetheless, the breakdown of Eq. (2.2) is more confusing. Presumably, it should be related to the absence of a well-defined Kolmogorov's inertial range for the inverse cascade discussed in LH03, for reasons such as that friction or planetary radius becomes important in halting the cascade and β is no longer relevant. Yet, if this is the case, we then lose the associated reasoning for why Eq. (2.1), i.e., mixing length being set by Rhines scale, is seen to hold in these slowly rotating simulations. A potential solution to this dilemma is that the latter's continuing relevance is justified by a different reasoning. For instance, an alternative argument could be that the mixing length is set by the meridional spacing scale of the jets, which then equals to Rhines scale due to the mechanisms not depending on the inverse cascade (e.g. Panetta 1993; Farrell and Ioannou 2008). Some studies have indeed found that the Rhines scale remains as the energy containing zonal wavenumber and jet spacing scale in quasi-linear simulations (in which one removes all wave-wave interactions), using models similar to the one used in this study (e.g. Chai and Vallis 2014; Chemke and Kaspi 2015). By design, there is no inverse energy cascade in those simulations, but whether and which of these other arguments captures the underlying physics of the Rhines scale's surprising general applicability remains to be clarified.

On top of that, we note that there is also a possibility that the diagnostics we use to evaluate Eq. (2.2) here is misleading. Specifically, the global average picture may not hold much physical meaning in the simulations with considerable changes in spatial structures, such as the ones with smaller Ω. It is known in this model that the Hadley cell expands substantially towards the pole as Ω is reduced, with the baroclinic eddies confining in a narrow latitude band at high latitudes and playing proportionally less

of a role in the poleward heat transport. However, the globally averaged eddy kinetic energy generation becomes larger for smaller Ω (within the examined Ω range) and predominantly controls the overall strength of the kinetic energy cycle and ϵ_d (Fig. 2.9). Such a counterintuitive dependence of the eddy statistics and energetics in the globally averaged view may be suggesting a need of more careful interpretations in this parameter range. We therefore leave this particular aspect of the results unexplained.

2.6 Overall performance as a closed theory

2.6.1 Approximating total heat flux as eddy heat flux

In Section 2.4 and Section 2.5, we have evaluated the individual assumptions in the scaling theories by testing them against the simulations. Previously, we have focused on uncovering the differences between BCT02 and HL96 and understanding the relationship between the two theories. During the process, a variety of errors are found in these theoretical assumptions. Some of these errors seem small and others are clearly seen to be nonnegligible, leading to quantitatively or even qualitatively inaccurate predictions (Figs. 2.2-2.5). However, when viewed individually, it is difficult to judge which are more important for the final prediction for diffusivity, which requires one to take into account the exact way how the scaling relations combine into a diffusivity closure.

As we have discussed in Section 2.3, to close the theory with Eqs. (2.1)-(2.3) and (2.9), we need to further relate the total heat flux ($\mathcal{F}$) in Eq. (2.9) back to D in Eq. (2.1). This involves an additional assumption that $\mathcal{F}$ can be approximated or scaled as eddy heat flux,

$$\mathcal{F} \sim -c_p D \frac{\partial \bar{T}}{\partial y}. \tag{2.12}$$

How well Eq. (2.12) fits to the simulations is shown in Fig. 2.6, where we see it works fairly well in varying Ω simulations and only slightly overestimates $\mathcal{F}$'s sensitivity to Δ_y. With this last assumption, we now start to piece together the different parts of the theory and discuss how the individual errors affect its overall performance as a closure.

2.6.2 Error assessment

To assess the actual error contribution made in each scaling relation to the diffusivity prediction, we plot in Fig. 2.7 a series of one-on-one comparison between the two diffusivity estimates whose difference come from a single scaling relation. In doing so, we can then isolate the errors brought in by each scaling relation and identify the major culprit for why the scaling theory may underperform as a whole. For the varying Δ_y simulations, we see the theory systematically overestimates the simulated D's sensitivity mostly because of the errors from Eq. (2.3) ($\epsilon_d \sim \dot{s}T_0^{-1}$; the second row) and Eq. (2.12) ($\mathcal{F} \sim -c_p D\partial_y \bar{T}$; the fourth row). The former is owing to the extra entropy source and the latter is owing to the extra mechanism for heat transport in the idealized GCM. Both are absent in the homogeneous two-layer QG model, so the breakdown of the theory in the varying Δ_y simulations can be attributed to the extra physics in the more complicated system.

For the varying Ω simulations, we also see the theory systematically overestimates the simulated D's sensitivity, especially for Ω smaller than the control. This is nonetheless not due to the uncertainties in estimating ϵ_d, that is, neither the difference in entropy versus APE budgets argued by BCT02 (i.e., Eq. (2.3)) nor the difficulties in diagnosing $\mathcal{M}$ in Eq. (2.9). Instead, it is because of Eq. (2.2)'s breakdown in the very beginning ($V_t^2 \sim \beta^{-2/5}\epsilon_d^{4/5}$; the first row). As we have discussed in Section 2.5, the reason for this breakdown remains unclear to us. It can either be the global average is inappropriate in these Ω simulations, pressing the need to explicitly

address the spatial inhomogeneity and the extra complexities in the model that are missing in the homogeneous two-layer QG dynamics. It can also be related to that the turbulence scaling of HL96 is found to be problematic in a broader parameter space in the homogeneous two-layer QG model when bottom friction plays a nonnegligible role (Thompson and Young 2007). Along with the mystery about Eq. (2.1)'s nice fit, this seems that one has to sort out these more fundamental aspect of uncertainty in the theory, in order to tackle the former and distinguish the two theories. It therefore provides a good reason to revisit the problem in the simpler models and work more systematically up from the bottom of the model hierarchy, as we do in Chapter 3 and Chapter 4 to follow.

2.6.3 Closure form

Finally, we move toward the closure form of the theory. We replot the predictions by the second scaling with D in both sides (open circles) in the fourth row of Fig. 2.7 again in Fig. 2.8 as filled circles. At this step, we have in principle related back to D and closed the theory. Yet, we can further rearrange the scaling to get rid of D in the rhs and obtain a new expression,

$$D \sim \beta^{-2} \left(c_p \frac{\partial \bar{T}}{\partial y} \left. \frac{\partial \ln \bar{T}}{\partial y} \right|_m \right)^{3/2} \tag{2.13}$$

Now the rhs consists of the variables we assume to be known a priori and can be used directly to predict D. We also plot the estimates by this expression in Fig. 2.8 as open circles. From the equations themselves, we expect errors to be magnified by $5/2$ times using Eq. (2.13) in the log-log view, consistent in the figure. As the two set of predictions are using identical theoretical assumptions, this cautions that the use of different ways of visualizing and interpreting the performance of the scaling theories can affect one's impression of the theories' value.

Written as Eq. (2.13), we can also see more straightforwardly how Eq. (2.13) is modified from the closure form of LH96, i.e., $D \sim \beta^{-2}\tau^{-3}$ with τ the inverse Eady growth rate (Section 2.1). Specifically, the only change is that τ is replaced by the timescale

$$\tau_e \equiv \left(c_p \frac{\partial \bar{T}}{\partial y} \left. \frac{\partial \ln \bar{T}}{\partial y} \right|_m \right)^{-1/2}. \tag{2.14}$$

This is also relatively easy to see how this might be extended to a moist system. As discussed in Held (2007), if we replace dry variables by moist variables in all the involved thermodynamic definitions, the additional complexity that may be introduced by transitioning from a dry to a moist system is yet another entropy source term associated with moisture diffusion that will appear in entropy budget and potentially complicate Eq. (2.3). To the extent that Eq. (2.3) still holds reasonably well, then Eqs. (2.13)-(2.14) would directly apply to a moist system as well. Thus, we expect that the investigation here is still relevant to or at least can be largely extended to BCT02's moist model simulations.

2.7 Conclusions

Motivated by the success of Barry et al. (2002, hereafter BCT02)'s diffusivity theory in explaining a comprehensive GCM's poleward eddy heat transport and the mysteries about how their theory is related to the theory proposed by Held and Larichev (1996, hereafter HL96) for the homogeneous two-layer QG turbulence, Lapeyre and Held (2003) performed a deeper investigation on the determination of eddy scaling in the homogeneous two-layer QG model. Expanding upon their work, this study conducts a thorough assessment on the two theories in an idealized dry GCM forced by Held-Suarez physics, focusing on the analyses of its global scale characteristics. The obtained results can be summarized as the following aspects.

First, we demonstrate that the two theories are both special cases of a more general theory. The most important (and to some extent the only fundamental) difference between the two studies is the different approximations they have made on the effective temperature difference along the direction of the heat flux, i.e., $\partial_y \ln \bar{T}|_m$, when they tried to estimate the kinetic energy dissipation (ϵ_d) through thermodynamic budgets. In particular, HL96 assumed that the mean mixing surface where the heat flux is aligned the same as mean isentropes while BCT02 assumed that it is horizontal. We show neither of these assumptions are consistently very good approximations in our idealized GCM simulations. Overall, both approximations fit to the simulations worse than the general form with the effective mixing surface being explicitly diagnosed. However, issues remain on how to best calculate the effective mixing slope in these simulations.

Second, we evaluate each assumption in the two theories extensively with our idealized GCM simulations. This is to study in what aspect the extra dynamics in this model, relative to the homogeneous two-layer QG, brings in nonnegligible complexities to the scaling theory. Among these complexities, an important one is the presence of mean meridional circulation and the associated poleward and upward heat transport. Another is presumably the presence of thermal damping on the eddies, which causes the effective mixing surface to deviate from the mean isentropic surface and produces entropy additionally. These complicate the global budgets of total potential energy, kinetic energy, and entropy, reducing the accuracy of the scaling relations. As a result, estimating ϵ_d becomes less straightforward either from APE generation or entropy destruction. Also, since it is the total poleward heat flux to be related to the heating in the total potential energy budget, one unfortunately loses the precise connection of ϵ_d back to diffusivity, just as the scaling expression of BCT02. One could potentially still incorporate this eddy heat flux theory into an axisymmetric model that generates the mean meridional flow itself from the axisymmetric dynamics, but in practice this

would involve a closure for eddy momentum as well as heat fluxes, which we have not addressed here.

Third, we examine the simulations that span a relatively wider parameter space than those in BCT02 (and likely also different from those in HL96) to investigate how these theories can potentially break down, especially for the part that is based on the two-dimensional (barotropic) turbulence theory. It is found that these turbulence scaling relations, i.e., $D \sim V^{3/2}\beta^{-1/2}$ and $V^2 \sim \epsilon^{4/5}\beta^{-2/5}$, hold fairly well in the simulations running at Earth's rotation rate but forced with various radiative-equilibrium equator-to-pole temperature differences (Δ_y). The scaling $V^2 \sim \epsilon^{4/5}\beta^{-2/5}$ fits loosely in the simulations forced with Earth-like Δ_y but when rotation rate (Ω) is greater than the Earth's. But for smaller Ω, it cannot even give a qualitatively correct prediction. We have not been able to identify the clear boundaries setting apart the parameter spaces where the scaling should work or not and the reasons for the discrepancies. Yet, we recognize that they may potentially agree with the findings in the previous two-layer QG studies on their limitation in explaining some parameter regimes (Lapeyre and Held 2003; Thompson and Young 2007). Also, despite these issues with $V^2 \sim \epsilon^{4/5}\beta^{-2/5}$, the Rhines scaling $D \sim V^{3/2}\beta^{-1/2}$ is well-behaved in all the simulations examined. The fact that $D \sim V^{3/2}\beta^{-1/2}$ can be more general than $V^2 \sim \epsilon^{4/5}\beta^{-2/5}$ (and their combination $D \sim \epsilon^{3/5}\beta^{-4/5}$) may imply the mixing length equal to Rhines scale is not because of energy inverse cascade being halted by β effect in all parts of parameter space but some other mechanisms that are yet to be clarified (e.g. Panetta 1993; Farrell and Ioannou 2008; Chai and Vallis 2014; Chemke and Kaspi 2015).

Last, we want to underscore the theory's potential in consolidating our understanding of the dry and moist systems. In its essence, the theory is based on the nature of the atmospheric circulation being a thermally driven heat engine, where its strength, set by heating and temperature distribution, are determined internally by

the circulation itself. This two-way relationship between dynamics and thermodynamics provides the physical basis for the (quasi-)two-dimensional turbulence scaling (i.e., scaling for D determined by ϵ) and the conservation of entropy and energy (i.e., scaling for ϵ determined by D) used in the theory to constrain the system. Since these constraints do not depend on composition of the air, the theory can apply to the moist atmospheres as well. Hence, while our numerical analyses are limited to a dry system, we do not see fundamental complications to extend the calculations to moist models, including the one studied in Barry et al. (2002). If taking the nice fit of their $\partial_y \ln \bar{T}|_m$ approximation to their model simulations seriously, it is suggestive that the role of thermal stratification may not be particularly important for the scaling relations in moist comprehensive models. This is a topic that would be interesting to be further explored.

There are many incremental steps toward closing the full knowledge gap between homogeneous two-layer QG models and comprehensive GCMs. As we have introduced in Chapter 1, in between these two limits of the model complexity, many previous studies have also investigated the scaling theory of Held and Larichev (1996) in the models with various levels of complexities. They have also worked on elucidating to what extent the theory's assumptions and implications can be directly carried over from one model to another or require further modification to consider new dynamics and physics. With the particular focus on the idealized dry GCM, we hope to help reframe and sharpen the existing questions and identify new important ones. In fact, these results are the direct motivation for the work reported in the following chapters. We will refer back to this chapter whenever it is relevant.

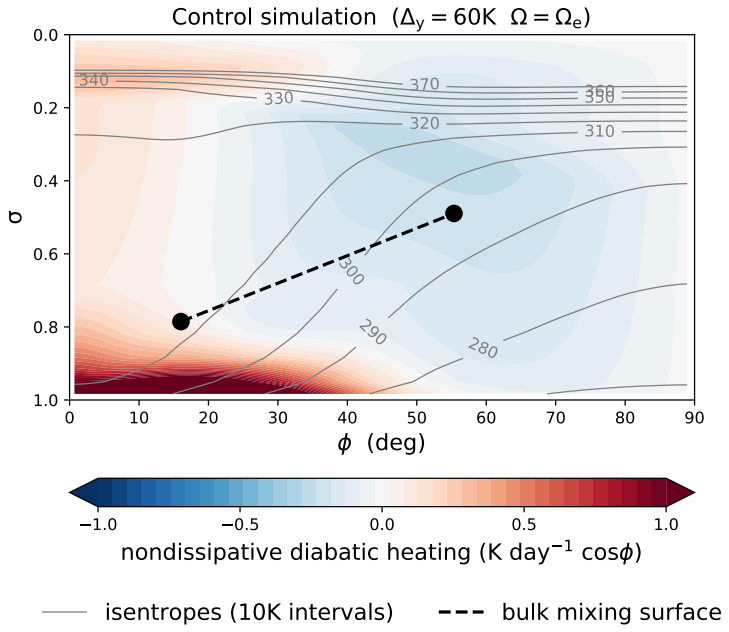

Figure 2.1: Mean thermal structure of the control simulation (Δ_y =60K and $\Omega = \Omega_e$). The potential temperature is plotted as the gray contours with a 10K interval, and the nondissipative diabatic heating is plotted as the colored shading with its magnitude indicated by the colorbar. The two black dots denote for the centroids of heating and cooling, respectively, and the dashed line linking them is the bulk mixing surface defined accordingly. The detailed definitions are described in the text.

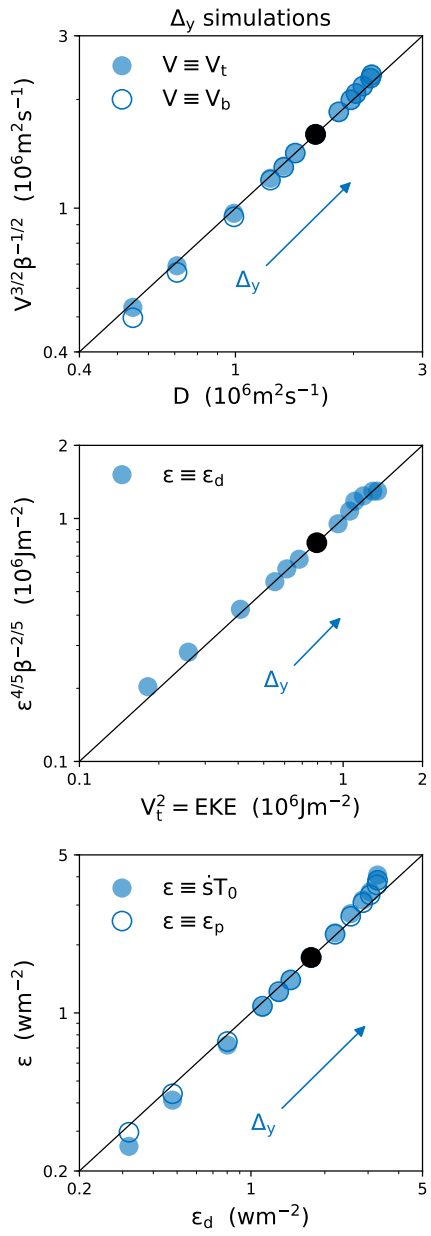

Figure 2.2: Diffusivity (D), eddy kinetic energy (EKE), and kinetic energy dissipation (ϵ_d) in the varying Δ_y simulations: the log-log plots of the simulations versus the predictions based on the scaling relations. In the top panel, two D predictions are provided by Eq. (2.1) with V estimated as the squared root of the EKE in two different ways: one is the total EKE (V_t; filled circles) and the other is the barotropic EKE (V_b; open circles). In the middle panel, the V_t^2 prediction is provided by Eq. (2.2) with ϵ estimated as ϵ_d. In the bottom panel, two ϵ_d predictions are provided. The first is from Eq. (2.3) the simulated globally averaged entropy destruction with a constant reference temperature ($\dot{s}$ times T_0; filled circles), and the second is the globally averaged eddy kinetic energy generation (ϵ_p; open circles). All the predicted values are multiplied by a constant such that the prediction for the control simulation (black filled) equals to the simulated value. The arrows indicate the direction where Δ_y increases.

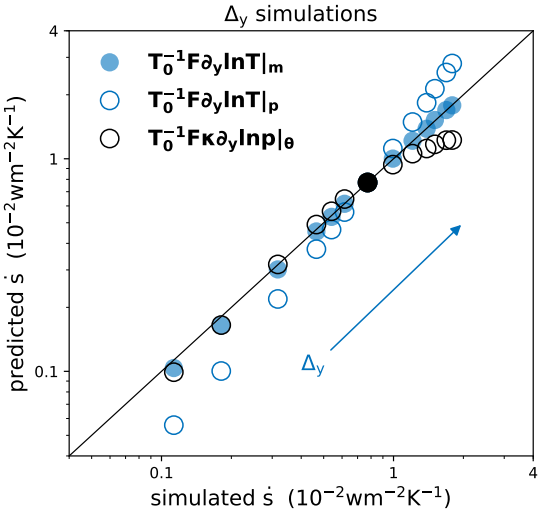

Figure 2.3: Globally averaged entropy destruction ($\dot{s}$) in the varying Δ_y simulations: the log-log plots of the simulated $\dot{s}$ versus three different predictions based on Eq. (2.9) (${T_0}^{-1}\mathcal{F}\ \partial_y \ln \bar{T}\big|_m$; colored filled) , Eq. (2.11) (${T_0}^{-1}\mathcal{F}\ \partial_y \ln \bar{T}\big|_p$; colored open), and Eq. (2.10) (${T_0}^{-1}\mathcal{F}\kappa\ \partial_y \ln \bar{p}|_\theta$; black open). All the relevant quantities are diagnosed from the simulations with the details described in the text. All the predicted values are multiplied by a constant such that the prediction for the control simulation (black filled) equals to the simulated $\dot{s}$. The arrows indicate the direction where Δ_y increases.

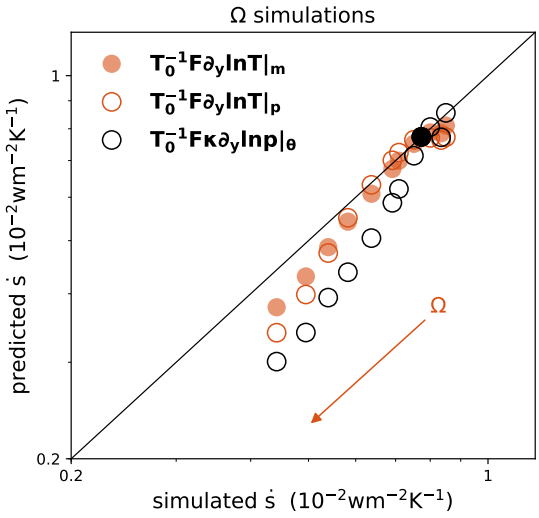

Figure 2.4: As in Fig. 2.3, but for the varying Ω simulations.

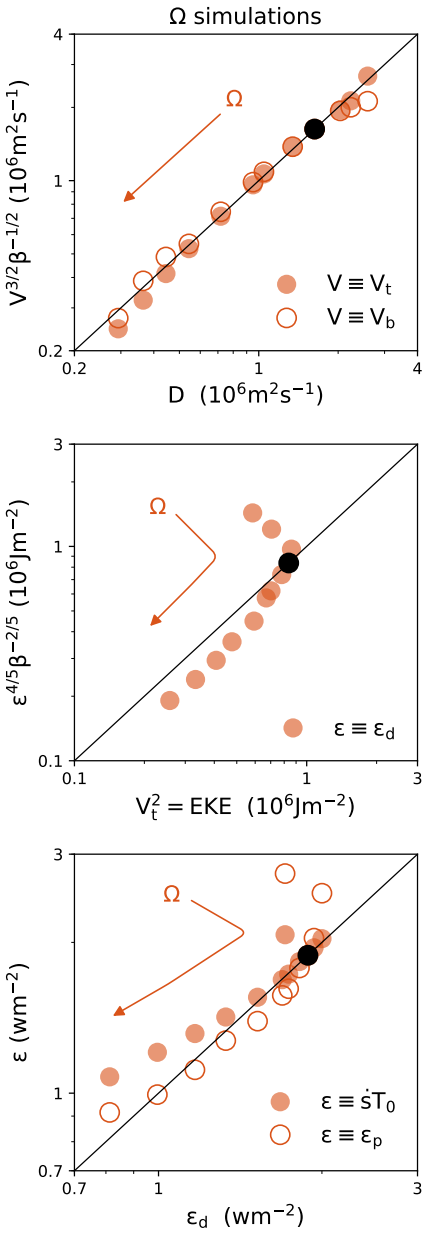

Figure 2.5: As in Fig. 2.2, but for the varying Ω simulations.

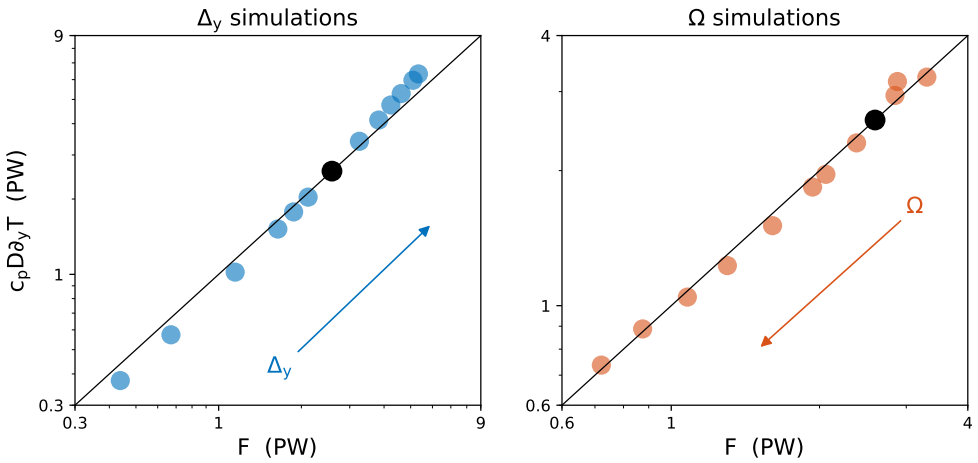

Figure 2.6: Total heat fluxes in the varying Δ_y (blue) and Ω (red) simulations: the log-log plots of the simulated total heat flux ($\mathcal{F}$) versus the predictions by Eq. (2.12). All the predicted values are multiplied by a constant such that the prediction for the control simulation (black filled) equals to the simulated $\mathcal{F}$. The arrows indicate the direction that the parameters' value increases.

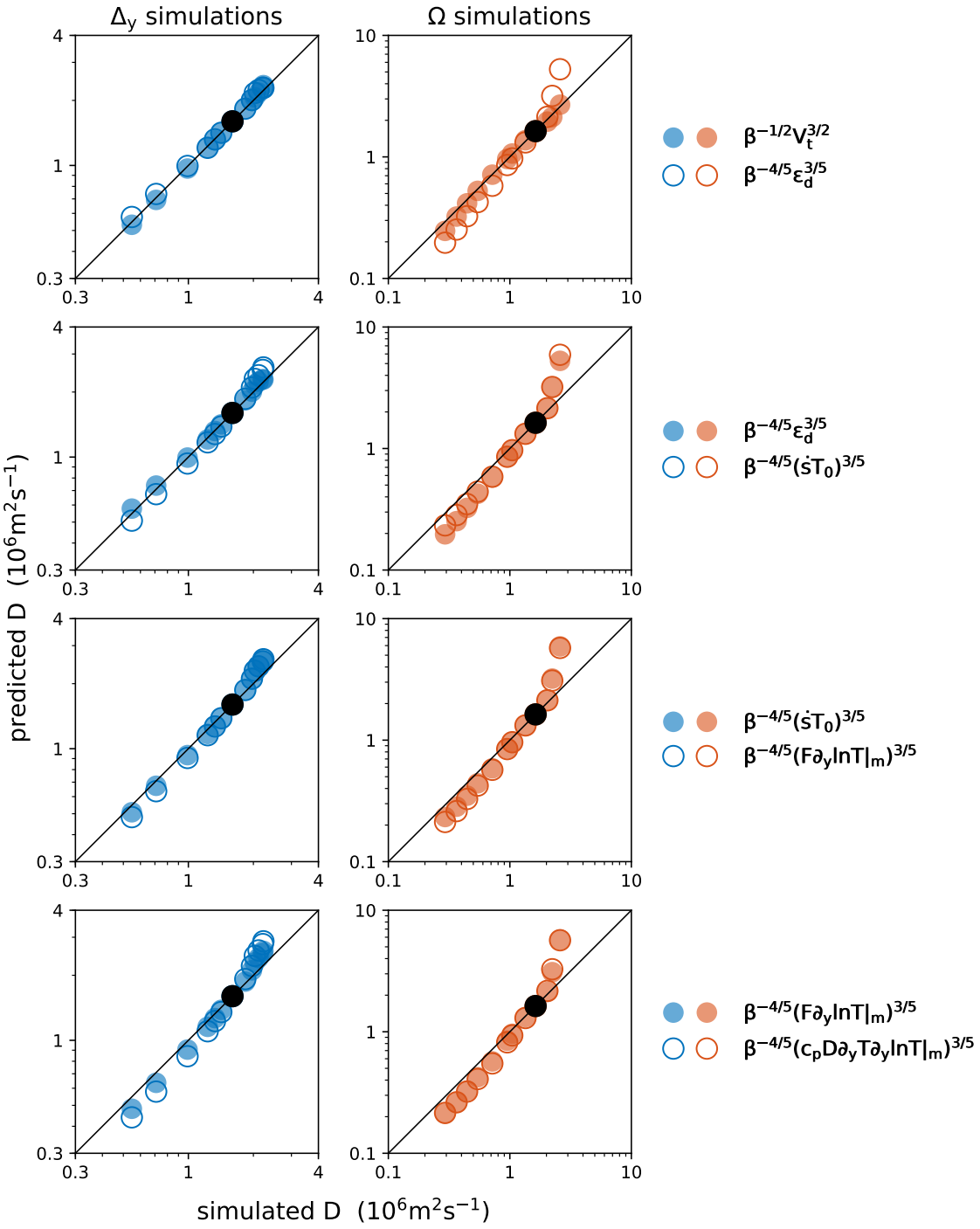

Figure 2.7: Error contribution by each scaling assumption to diffusivity prediction in the varying Δ_y (blue) and Ω (red) simulations: the log-log plots of the simulated diffusivity (D) versus the predictions based on the various combinations of the acaling relations. All the predicted values are multiplied by a constant such that the prediction for the control simulation (black filled) equals to the simulated D.

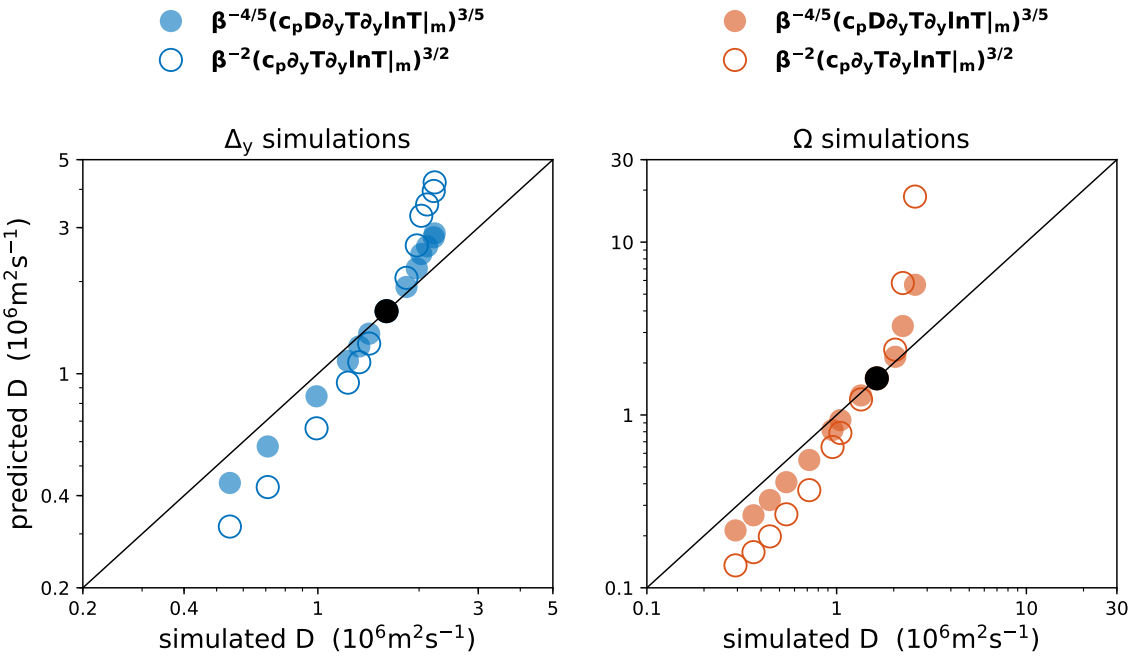

Figure 2.8: Final results of diffusivity prediction by the closure form in the varying Δ_y (blue) and Ω (red) simulations: the log-log plots of the simulated diffusivity (D) versus its predictions in two different ways of visualization. All the predicted values are multiplied by a constant such that the prediction for the control simulation (black filled) equals to the simulated D.

2A Calculations of global kinetic energy and entropy budgets

In the idealized GCM, global kinetic energy generation is equal to the net energy conversion from potential energy to kinetic energy, since the atmosphere as a whole is not mechanically forced. With the aid of temperature equation, we can calculate the time averaged equation of global kinetic energy as

$$\langle \bar{\omega}\bar{\alpha} \rangle + \langle \overline{\omega'\alpha'} \rangle = \epsilon_d, \tag{2.15}$$

where $\omega = dp/dt$ is pressure velocity, α is the inverse of density, and the angle brackets $\langle\ \rangle$ denotes the mass-weighted integral over the atmosphere. Its lhs is the total energy conversion from potential energy to kinetic energy, and its rhs is total kinetic energy dissipation. We can further partition the energy conversion into the one from mean potential energy to mean kinetic energy ($\langle \bar{\omega}\bar{\alpha} \rangle$) and the one from eddy potential energy to eddy kinetic energy ($\langle \overline{\omega'\alpha'} \rangle = \epsilon_p$). Their parameter dependence are shown in Fig. 2.9.

The steady state global entropy budget of this model is calculated following Zurita-Gotor et al. (2015),

$$\dot{s} \equiv -\left\langle \frac{\bar{Q}}{\bar{T}} \right\rangle = \left\langle \overline{\frac{Q}{T} - \frac{\bar{Q}}{\bar{T}}} \right\rangle + \left\langle \overline{\frac{Q_f}{T}} \right\rangle + \left\langle \overline{\frac{Q_{h,T}}{T}} \right\rangle, \tag{2.16}$$

where Q, Q_f, $Q_{h,T}$, and T denote for the heating due to Newtonian relaxation (defined in Section 2.2), heating due to kinetic energy dissipation (from both Rayleigh drag and hyperviscosity), heating due to temperature hyperdiffusion, and temperature, respectively. The lhs of the equation is the time mean diabatic entropy destruction, which is the only destruction term and denoted as $\dot{s}$ in the main text. The other terms in the rhs are production terms. They are, from left to right, the eddy diabatic

entropy production, the mechanical entropy production, and the entropy production of temperature diffusion. Except the last term, they are shown in Fig. 2.9 for all the simulations.

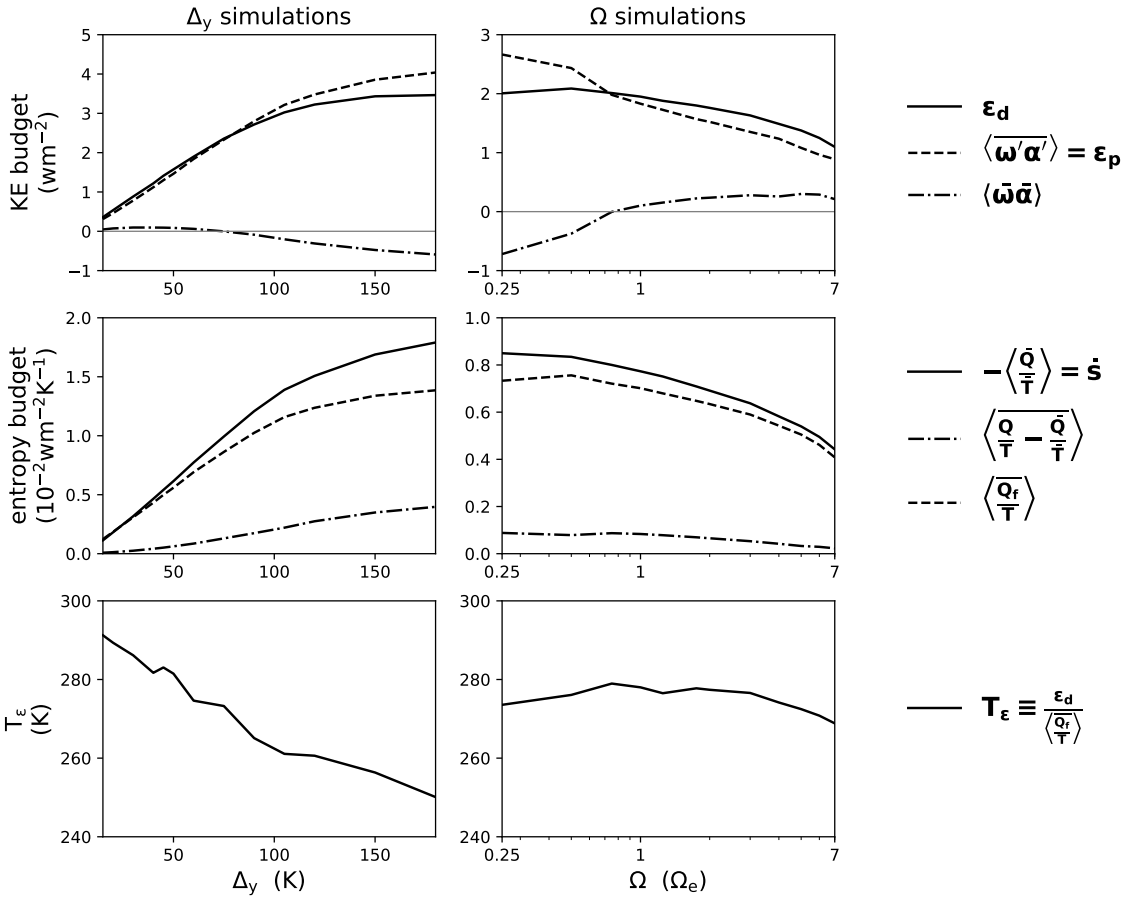

Figure 2.9: Budget analysis for the varying Δ_y (left) and Ω (right) simulations: (from top to bottom) the global kinetic energy budget, the global entropy budget, and the averaged dissipative temperature (T_ϵ). The definitions of the terms are described in Appendix 2A.

Chapter 3

Eddy equilibration in two-layer QG models: the roles of surface friction

Motivated by the problem on the barotropic inverse cascade argument identified in Chapter 2, this chapter returns to the homogeneous two-layer QG model where the argument is first proposed. We first investigate the model at the $\beta = 0$ limit to study eddy equilibration when the only process stopping the inverse cascade is surface friction.

3.1 Introduction

Ever since Phillips (1956)' pioneering work, the quasigeostrophic two-layer model has repeatedly proven itself to be useful for understanding the baroclinic eddy dynamics in the extratropical troposphere. To better study how eddy statistics depend on mean flows, the model can be further simplified with a fixed background zonal flow with vertical shear that is independent of latitude, and that assumes the deviations from this flow to be horizontally homogeneous. This is known as the homogeneous quasigeostrophic two-layer model, and it has also provided some insights into the dependence of eddy amplitudes and eddy fluxes on the background state (Haidvogel and

Held 1980; Larichev and Held 1995; Held and Larichev 1996; Thompson and Young 2006, 2007). However, the flows in this idealized system are still complex enough to prevent us from fully understanding the control of eddy scales by the parameters of interest. One such parameter is the meridional gradient of Coriolis parameter (β). The presence of β introduces flow anisotropy, Rossby waves, coherent structure as zonal jets, and asymmetry between the two layers. These complexities have raised challenging questions as well as stimulated theories that attempt to address them from different perspectives. Yet, the theories differ from each other, and a general consensus has not been reached (Held and Larichev 1996; Lapeyre and Held 2003; Thompson and Young 2007; Chai 2016).

To test our understanding of the homogeneous quasigeostrophic two-layer model, reconciling these theories is important. It is nonetheless also very difficult. To reduce the problem to a smaller one in which we can likely make progress, we focus on the homogeneous quasigeostrophic two-layer model in the limit of $\beta = 0$. At the very least, eliminating β enables us to gain a better sense of the extent of complexities that are not directly associated with β. In particular, large-scale surface friction and its roles in affecting the eddy statistics often receive less attention when β is present. For a strongly baroclinically unstable flow, the scale of energy containing eddies is determined by the mechanism stopping the barotropic inverse energy cascade (Rhines 1977; Salmon 1978, 1980). This can either be β or friction (or both), but it is often assumed that β is large enough to stop the cascade, that is, channel the energy into zonal flows that do not contribute to meridional transport, before friction becomes significant (e.g. Rhines 1975). To make further progress in understanding how the cascade is terminated when both are present, we need to better understand how friction alone stops the cascade. This understanding will help us determine if this limiting case might itself have some relevance in some atmospheric (and oceanic) circulations of potential interest.

In the attempt to assess the importance of surface friction in this respect, Held (1999, hereafter H99) proposed a scaling theory to estimate the eddy scales when the cascade stopping mechanism is nonlinear (quadratic) friction. The friction in the atmospheric planetary boundary layer is typically parameterized as a quadratic drag. When imposing quadratic drag on layer models of the sort considered here, one needs to divide the nondimensional drag coefficient (C_D) in the surface stress law by the depth of the lowest model layer (H), since it is only in this combination that the surface stress is felt by the model. This results in an inverse frictional length, $L_D^{-1} \equiv C_D H^{-1}$. The strength of this type of frictional damping is then determined by L_D. If the large-scale drag is responsible for essentially all of the dissipation of kinetic energy (ϵ_d), then we expect that ϵ_d is scaled as

$$\epsilon_d \sim L_D^{-1} V^3, \tag{3.1}$$

where V is a characteristic velocity scale. According to Larichev and Held (1995, hereafter LH95), if the two-layer baroclinic turbulence is sufficiently unstable so that kinetic energy is mostly barotropic, V can be thought as the typical velocity in the barotropic flow at the energy-containing eddy length scale (L). Suppose that the barotropic energy spectrum is well approximated by Kolmogorov's inertial range theory, then V can be solely determined by L and the rate of inverse energy cascade (ϵ_c) via dimensional analysis,

$$V \sim L^{1/3} \epsilon_c^{1/3}. \tag{3.2}$$

Given $\epsilon_d \approx \epsilon_c$, Eqs. (3.1) and (3.2) together indicate that, if the cascade is stopped by quadratic drag alone, the energy-containing eddy length scale should be proportional to the frictional length,

$$L \sim L_D, \tag{3.3}$$

which is the same as the eddy scaling for two-dimensional turbulence stirred at small scales and damped by quadratic drag (Grianik et al. 2004). Building on this scaling relation, one can further estimate an eddy diffusivity (D) from mixing length theory,

$$D \sim VL. \tag{3.4}$$

If the eddy heat fluxes are mostly due to the passive mixing of temperature (the baroclinic streamfunction in the two-layer model) by the energy-containing barotropic eddies and therefore are diffusive-like, the available potential energy production (ϵ_p) in the homogeneous quasigeostrophic two-layer model can be expressed as

$$\epsilon_p \sim DU^2\lambda^{-2}, \tag{3.5}$$

where U is the imposed vertical shear (proportional to temperature gradient) and λ is the radius of deformation (prescribed in a quasigeostrophic model). One factor of U in this expression arises from the temperature gradient in the expression for available potential energy generation; the other arises from expressing the eddy heat flux as a diffusivity times a temperature gradient. (We note that this is exactly the two-layer QG version of Eq. (2.5).) Provided that $\epsilon_p \approx \epsilon_d$, Eqs. (3.1), (3.2), (3.4), (3.5) together also suggest that

$$V \sim L_D U\lambda^{-1}, \tag{3.6}$$

$$D \sim L_D^2 U\lambda^{-1}. \tag{3.7}$$

This theory can therefore predict how the characteristic eddy length, velocity and diffusivity change with L_D. To see this more clearly, we can also nondimensionalize Eqs. (3.3), (3.6), and (3.7) with U and λ. This nondimensionalization has the effect of clarifying the difference between this theory and Stone (1972)'s, in which λ and U

are assumed to be the scales for L and V. The H99 scaling predicts that $L\lambda^{-1}$ and VU^{-1} are both proportional to $L_D\lambda^{-1}$ which is a measure of the strength of inverse cascade. A corollary of this result is that an inverse cascade is only expected when L_D is larger than λ.

Another way of stating the above prediction is that the extent of an inverse energy cascade depends on the ratio of two dimensionless numbers: the Prandtl ratio (f/N) and the nondimensional drag coefficient (C_D). Recall $L_D^{-1} \equiv C_D H^{-1}$ and suppose that the same H appears in the definition of $\lambda \equiv NH/f$ (while they do not need to be the same in general), then the ratio $L_D\lambda^{-1} = (f/N)C_D^{-1}$. For the typical atmospheric values, $f/N \approx 10^{-2}$. If $C_D \approx 10^{-3}$ such as over the oceans, this theory suggests that there should be a significant inverse energy cascade; in contrast, if $C_D \approx 10^{-2}$ such as over the land surface, there should be little cascade. The relevance of this ratio of the nondimensional drag coefficient and the Prandtl ratio for whether or not the eddies are strongly damped in this sense is therefore an interesting implication of this scaling argument.

There have been some numerical studies on how eddy scales depend on quadratic drag (in the absence of β), but none of their simulations fully support H99's eddy scaling or the suppression of inverse cascade when drag becomes sufficiently large (Arbic and Scott 2008; Jansen et al. 2015). A possible explanation for this simulation-theory inconsistency is that the theory fails to distinguish the diverse velocity scales in the two-layer system. It oversimplifies the difference between the velocity scale relevant for frictional dissipation (in Eq. (3.1)) and the velocity scale relevant for inverse cascade (in Eq. (3.2)). Compared to the two-dimensional system, this additional level of complexity may be attributed to the layer asymmetry caused by friction only appearing in the bottom layer. If friction appears symmetrically between the two layers, eddy statistics in the two layers would be identical. This, along with the fact that most kinetic energy is barotropic when friction is weak, implies all the velocities

should scale closely with each other. However, even if the eddy statistics in the two layers are indeed identical, the two-layer system still has two degrees of freedom in the vertical. Interactions between barotropic and baroclinic modes can still result in eddy statistics of the barotropic mode in this two-layer system differing considerably from eddy statistics of a two-dimensional system (i.e. Eq. (3.2) may be invalid). If the theory fails only due to the layer asymmetry, improving the theory would only require an extra consideration on the bottom heaviness of friction. If it also has to do with the latter, we would need to reassess the assumptions in LH95 more fundamentally.

In fact, if one had considered the case of linear drag and tried to use the assumptions made in LH95 to derive a scaling theory that is analog to H99's theory for quadratic drag, one would have arrived at a conclusion that the linear drag (alone) cannot halt the inverse energy cascade and the system would not equilibrate. In such a scenario, there would be no statistically steady state unless the effect of finite domain size is considered. A related aspect of why LH95 theory with linear damping may be invalid has indeed been addressed in Thompson and Young (2006, hereafter TY06), who studied the simulations that are conducted with the model configuration similar to LH95 and with the bottom linear drag strong enough to prevent the eddy mixing length reaching the domain size. They have found that the model did equilibrate with well-defined eddy statistics. Also, different from what is expected by LH95, most temperature anomalies are seen to be concentrated in the cores of the coherent vortices persisting in the domain. This leads them to argue that the heat transport is due to the drift of these vortices, rather than temperatures being passively mixed by the barotropic eddies. It therefore questions the relevance of the "dual-cascade" picture on which LH95 and H99 are based.

The goal of this study is to determine whether and how these different complexities lead to the breakdown of H99's theory, and we consider the homogeneous quasigeostrophic two-layer model in the limit of $\beta = 0$ with quadratic drag as the

ideal system to tackle the problem. To study how the layer asymmetry caused by the bottom friction affects the eddy scaling, we conduct numerical simulations with two types of frictional damping: one with quadratic drag appearing in the bottom layer only (referred to as asymmetric drag) and the other with quadratic drag appearing symmetrically between the two layers (referred to as symmetric drag). In Section 3.2, we diagnose the eddy scales in these two sets of simulations and compare their dependence on the nondimensional damping strength to discern the differences resulting from layer asymmetry. Since the layer asymmetry is completely removed in the symmetric drag configuration, we can also test its eddy scaling with H99's theoretical prediction more cleanly to isolate the other complexities related to the uncertainties in the theory. The observed deviations of symmetric drag simulations from the prediction has motivated a heuristic theory that is modified from LH95's assumptions to take the spectral nonlocality of barotropic energy input into account. We present this modified theory in Section 3.3 and check it with the asymmetric drag simulations in Section 3.4 to verify whether the complexity due to the spectral nonlocality can be well separated from the complexity due to the layer asymmetry. We also investigate the strong symmetric drag regime where the eddies equilibrate without an inverse cascade. The eddy scaling and the sensitivity of equilibrated eddy statistics to initial conditions in this regime are explained (Section 3.5).

Built on these quadratic drag results, we then discuss how the modified theory, because of the departure from H99 scaling, can make a well-defined prediction for the case with linear damping (Section 3.6). After clarifying the relations between quadratic and linear drag, we are eventually better posited to address the question why the modified scaling, which is still based on the LH95's physical picture, can be useful despite its apparent conflict with TY06's findings. We discuss this issue in Section 3.7. Finally, we show an example of a series of simulations in an inhomogeneous channel model with $\beta = 0$ to illustrate that the diffusivity obtained from the

homogeneous model can be used to predict the behavior of the baroclinic unstable jets in these inhomogeneous simulations (Section 3.8). We conclude with the discussion of some implications and remaining questions on understanding the baroclinic eddy scales in more complicated and realistic flows (Section 3.9).

3.2 Asymmetric versus symmetric drag simulations

We set up the homogeneous two-layer quasigeostrophic model in a way that closely resembles the one investigated by LH95. The model solves the same set of the equations as in LH95 (c.f. their Eqs. (1)-(3)) except for the replacement of the large-scale dissipation in the linear drag form with the quadratic drag form described in Grianik et al. (2004). The model equations are presented in the Appendix 3A along with details of the numerics. As noted there, the value of U is irrelevant in the case with quadratic drag since there are no timescales, only length scales, defined by the model (changing U only has the effect of renormalizing velocities as shown in Arbic and Scott (2008)). Following LH95's notations, we express the model parameters in the length unit as wavenumbers (k; the first wavenumber $k = 1$ is the wavenumber of the domain length): k_d denotes the wavenumber of λ and c_D denotes the wavenumber of L_D. Hence, the single nondimensional parameter characterizing the system is $c_D k_d^{-1}$, whose physical meaning is essentially the nondimensional damping strength. Varying the value of $c_D k_d^{-1}$, we conduct a series of model simulations (Fig. 3.1). We initialize the model from infinitesimal perturbations in the streamfunction field, and we compute the eddy statistics from the timeseries of the statistically steady state. These eddy statistics include the characteristic eddy length scale (L), velocity (V), and diffusivity (D) that we have introduced in Section 3.1 and will now be more

precisely defined in the same way as TY06,

$$L \equiv \left\langle \tau^2 \right\rangle^{1/2} U^{-1} \tag{3.8a}$$

$$V \equiv \left\langle (\partial_x \psi)^2 \right\rangle^{1/2} \tag{3.8b}$$

$$D \equiv \langle (\partial_x \psi)\, \tau \rangle U^{-1} \tag{3.8c}$$

where ψ and τ are the barotropic and baroclinic streamfunction, respectively, and $\langle\rangle$ refers to domain average. The diagnosed eddy scales (nondimensionalized by U and k_d) are plotted in Fig. 3.2 as a function of $c_D k_d^{-1}$. The results of asymmetric drag are shown in red and the results of symmetric drag are shown in black. Different symbols indicate slightly different model settings with different domain sizes and resolutions (Fig. 3.1), which are examined to ensure the results are to a large extent not affected by the choice of these additional parameters with less physical interest. Also, we note that the asymmetric drag results are purposely plotted at $c_D k_d^{-1}/2$ as opposed to $c_D k_d^{-1}$ for a reason that we explain shortly, and this does not change the interpretation of the scaling relations.

We first draw the attention to the asymmetric drag results. As shown in Fig. 3.2, all the eddy scales in the asymmetric drag simulations decrease with increasing $c_D k_d^{-1}$ when $c_D k_d^{-1}$ is small. When $c_D k_d^{-1}$ gets closer to 10^0, this decreasing trend slows down, so the eddy scales can be described as exhibiting an exponential dependence over a limited range of damping. The case of $c_D k_d^{-1} = 10^0$ seems to be an interesting transition point where both L and V reach their minimum. As $c_D k_d^{-1}$ continues to increase from 10^0, L and V become larger again while D still keeps decreasing. Here the bottom flows are strongly damped by friction and most kinetic energy is stored in the top layer. The strong asymmetry between the two layers led Arbic and Scott (2008) to argue that the theory based on barotropic-baroclinic decomposition is less relevant in this limit. They assumed instead that the inverse cascade occurs in the top

layer and closed the theory with a diagnostic relation based on the primary balance in the bottom layer potential vorticity equation. These revised assumptions result in a new set of scaling laws, $D \sim c_D^{-1/5}$ and $L \sim c_D^{1/5}$. We find that it fits qualitatively to our simulations and apparently explains why the simulated D and L have opposite dependence on $c_D k_d^{-1}$. This reaffirms the crucial role played by layer asymmetry in this regime.

As a strong contrast, all the eddy scales in the symmetric drag simulations decrease monotonically when $c_D k_d^{-1}$ increases within the explored range. In the limit of small $c_D k_d^{-1}$, the symmetric drag results coincide with the asymmetric drag results. This is because most kinetic energy is barotropic and is equally partitioned between the two layers. The damping appearing in only the bottom layer is equivalent to the effective damping appearing in both layers but with a half of the damping strength (i.e. $c_D k_d^{-1}$). Hence, they are better aligned with each other when we shift the asymmetric drag results from $c_D k_d^{-1}$ to $c_D k_d^{-1}/2$. As $c_D k_d^{-1}$ increases, unlike the exponential relation seen in asymmetric drag simulations, eddy scales for symmetric drag simply follow a power law dependence on $c_D k_d^{-1}$ until $c_D k_d^{-1}$ reaches about 10^0. Beyond this value, another power law relation with a different slope is observed. The latter marks a new dynamical regime where the solution equilibrates without an inverse cascade. We analyze these simulations in more details in Section 3.5.

Based on the above results, we can now summarize the impact of layer asymmetry on eddy scaling into a few key findings. First, the asymmetry between the two layers as well as its impact is amplified when the damping is stronger. Second, the layer asymmetry is responsible for replacing a simple power law scaling (as would have been predicted by the theory) with a more complicated transition between two different scaling regimes that in between could be approximated as exponential. Third, the layer asymmetry allows the inverse cascade to continue to occur in the upper layer even when $c_D k_d^{-1}$ exceeds one. After isolating the sources of complexity by comparing

the asymmetric and symmetric drag simulations, we next examine the remaining complexities via comparing the symmetric drag simulations to the theoretical prediction by H99.

3.3 Symmetric drag simulations versus theoretical prediction

Without layer asymmetry, the two-layer system with symmetric drag seems more comparable to the two-dimensional system. It can therefore help better clarify the differences between the two systems that the theories of H99 and LH95 may have overlooked. Looking at the symmetric drag results in Fig. 3.2, we notice that for $c_D k_d^{-1} < 10^0$ the nondimensional characteristic scales of eddies can all be expressed as $\sim c_D^{-\mu}$. The exponent μ estimated from the least-squared fit using the data of $k_d = 50$ simulations is indicated in Fig. 3.2. These estimates are smaller than predicted by Eqs. (3.3), (3.6), and (3.7): $L \sim c_D^{-0.58}$, $V \sim c_D^{-0.78}$, $D \sim c_D^{-1.24}$ versus $L \sim c_D^{-1}$, $V \sim c_D^{-1}$, $D \sim c_D^{-2}$ (we note that the wavenumber c_D is inversely proportional to the length scale L_D). The simulated eddy scaling dependence on the damping strength is consistently weaker than the theoretical prediction, so some assumptions in the theory must be violated.

To address this discrepancy, we believe a good starting point is to recognize that L and V scale differently with $c_D k_d^{-1}$. The fact that L and V are not proportional to each other contradicts an important implication by LH95, that is the eddy timescale ($T \equiv LV^{-1}$) should scale with inverse Eady growth rate,

$$T \sim (Uk_d)^{-1}. \tag{3.9}$$

Since U and k_d are fixed in each set of our simulations, Eq. (3.9) requires L and V to change proportionally if the theory of LH95 holds well. Eq. (3.9) can be derived from Eqs. (3.2), (3.4), (3.5) together with $\epsilon_c \approx \epsilon_p$. Using the definitions of L and V in Eq. (3.8), Eq. (3.9) can also be phrased as a constraint on the partitioning between barotropic kinetic energy ($\langle E_\psi \rangle \approx V^2$) and baroclinic available potential energy ($\langle E_\tau \rangle = (LUk_d)^2$) of isotropic eddies,

$$\langle E_\psi \rangle / \langle E_\tau \rangle \sim cons. \tag{3.10}$$

Evidently, because L and V change differently with $c_D k_d^{-1}$, this energy ratio varies and in fact increases along with L in the simulations. A similar relation between $\langle E_\psi \rangle / \langle E_\tau \rangle$ and L is documented by LH95 for their bottom linear drag simulations, where they also found that $\langle E_\psi \rangle / \langle E_\tau \rangle$ increases as energy containing wavenumber becomes smaller. They have connected this behavior to the observed shape of the energy spectra. In their simulations, they recognized that the slope of barotropic energy spectrum is slightly steeper than $-5/3$ and the slope of baroclinic energy spectrum is slightly flatter than $-5/3$ (c.f. their Fig. 4). This deviation from Kolmogorov's theory is likely associated with a wide spread of energy injection from baroclinic to barotropic mode in wavenumber space. Taking the barotropic energy input's spectral nonlocality into account, they proposed a qualitative argument to explain the length scale dependence of energy ratio. We have attempted to make this argument more quantitative to explain the weaker c_D dependence of eddy scales that is observed in our simulations.

To illustrate how this argument based on spectral nonlocality modifies the original scaling, we follow LH95's derivation to first obtain its modification to Eq. (3.9). The essence of this argument is to allow an underdetermined wavenumber (k) dependence in barotropic energy spectrum $E_\psi(k)$. The theory of LH95 originally assumes that

energy transfer from baroclinic to barotropic mode is confined at k_d (Rhines 1977; Salmon 1978, 1980) so a Kolmogorov's inertial range exists and we expect $E_\psi(k) \sim \epsilon_\psi^{2/3} k^{-5/3}$, where barotropic cascade energy flux (ϵ_ψ) is independent of k. With the single dominant scale approximation, this directly leads to Eq. (3.2). However, if energy input is broadly spread among a range of wavenumbers and the local cascade energy flux picks up local energy injection as energy moves to smaller wavenumber, we may assume locally

$$\epsilon_\psi(k) = \epsilon_{\psi 0} k_d^x k^{-x}, \tag{3.11}$$

with $x > 0$ (we normalize k by k_d so that $\epsilon_{\psi 0}$ has the unit of energy flux); the modified barotropic energy spectrum would therefore become

$$E_\psi(k) \sim \epsilon_{\psi 0}^{2/3} k_d^{2x/3} k^{-(5+2x)/3}. \tag{3.12}$$

Then supposing that the baroclinic mode still acts like a passive tracer that is advected by the barotropic mode, the baroclinic energy spectrum would still follow $E_\tau(k) \sim \epsilon_\tau T(k) k^{-1}$, where the baroclinic cascade energy flux ϵ_τ is constant and local eddy turnover time $T(k)$ is determined by the advection field. With the modified barotropic energy spectrum, $T(k) \sim (\epsilon_{\psi 0}^{2/3} k_d^{2x/3} k^{2(2-x)/3})^{-1/2}$, the modified baroclinic energy spectrum becomes

$$E_\tau(k) \sim \epsilon_\tau \epsilon_{\psi 0}^{-1/3} k_d^{-x/3} k^{-(5-x)/3}. \tag{3.13}$$

Therefore, $x > 0$ implies a steeper barotropic energy spectrum and a flatter baroclinic energy spectrum. An immediate result that follows this modification, supposing the bulk energies predominantly reside at a single wavenumber that is associated with L and $\epsilon_{\psi 0} \approx \epsilon_\tau$, is that

$$\langle E_\psi \rangle / \langle E_\tau \rangle \sim (L k_d)^x, \tag{3.14}$$

and the ratio between barotropic kinetic energy and baroclinic available potential energy should increase with L. With the definition of T, we obtain a modified scaling replacing Eq. (3.9),

$$T \sim (Lk_d)^{-x/2}(Uk_d)^{-1}. \tag{3.15}$$

Compared with Eq. (3.9), Eq. (3.15) suggests T is no longer a constant and depends on L and x, which measures the broadness of energy input in the barotropic energy spectrum. Combining Eq. (3.15) with Eqs. (3.1), (3.4) and (3.5) gives the modified power law dependence of eddy scales on c_D,

$$L \sim c_D^{\frac{-1}{(1+x)}} \tag{3.16a}$$

$$V \sim c_D^{\frac{-(2+x)}{2(1+x)}} \tag{3.16b}$$

$$D \sim c_D^{\frac{-(4+x)}{2(1+x)}}. \tag{3.16c}$$

Hence, $x > 0$ also implies a weaker c_D dependence for L, V, and D.

To see if this modified scaling applies to our simulations, we estimate x using Eq. (3.16) with the simulated scaling relation $L \sim c_D^{-0.58}$ to obtain $x \approx 0.72$. This estimate is then compared with the slopes of energy spectra to verify the self-consistency of the assumptions we have made on the spectral slopes. From Eqs. (3.12) and (3.13), we expect

$$(E_\psi(k)k^{5/3})^{3/2} \sim k^{-x} \tag{3.17a}$$

$$(E_\tau(k)k^{5/3})^{3} \sim k^{x} \tag{3.17b}$$

near the energy-containing scale. These simulated spectra ($(E_\psi(k)k^{5/3})^{3/2}$ and $(E_\tau(k)k^{5/3})^{3}$) are plotted in Fig. 3.3's first and second rows. Although a single slope assumption does not fit to their shapes that well, $x \approx 0.72$ at least matches

qualitatively to the observed bulk spectral slopes (for simplicity, only the set of $k_d = 50$ simulations is shown).

In the third and fourth rows of Fig. 3.3, the simulated barotropic energy spectrum ($E_\psi(k)$) and the simulated barotropic energy flux ($\epsilon_\psi(k)$; calculated as described in LH95's Fig. 4) are further examined. To connect $E_\psi(k)$ back to $\epsilon_\psi(k)$, we have compared the simulated $E_\psi(k)$ with the prediction $C_\psi \epsilon_\psi(k)^{2/3} k^{-5/3}$ computed from the simulated $\epsilon_\psi(k)$ and the universal constant $C_\psi = 7$ chosen to give a reasonable fit. The latter is a good approximation for the former in the range of wavenumbers between the energy-containing scale (the peak of the spectrum) and $k_d = 50$, confirming that energy level at these wavenumbers is solely determined by the local upscale cascade. The observed steepness of the spectral slope from $-5/3$ is then due to the k dependence in $\epsilon_\psi(k)$, which if to be approximated by k^{-x} (i.e. Eq. (3.11)) is roughly consistent with the estimated $x \approx 0.72$.

Looking closely at the simulated $\epsilon_\psi(k)$, we shall note that its spectrum is actually not so well described as k^{-x}. If all the energy is both input at a single wavenumber and then removed at a single smaller wavenumber, $\epsilon_\psi(k)$ would be flat between these two wavenumbers. Instead, the actual spectral slope varies smoothly from negative to positive as k decreases. Both barotropic energy input due to triad interactions involving the baroclinic mode, whose spectral structures look very similar to the ones reported in LH95 (c.f. their Figs. 4 and 5), and the energy removal by quadratic frictional dissipation are nonlocal in wavenumber space, with the former dominant in the region of most interest, producing a negative slope. There is therefore no obvious physical basis for the use of the simple power law approximation (i.e. k^{-x}) as compared to a more general functional shape that can better describe $\epsilon_\psi(k)$'s spectrum. We emphasize that k^{-x} in Eq. (3.11) is thus better regarded as a heuristic assumption that we choose for its simplicity and effectiveness to study the complexities that lead to the deviations from the original theoretical prediction.

We also note that in the above derivation for Eq. (3.16) we have ignored the change of the correlation between barotropic velocity and baroclinic streamfunction ($r \equiv D/(VL)$) as a way to violate Eq. (3.4). From the estimated scaling fits (i.e. $\sim c_D^{-\mu}$) in Fig. 3.2, we can obtain $r \sim c_D^{0.12}$. The dependence of r on c_D could bring in uncertainty that leads to different estimates of x when we fit the simulated V and D using Eq. (3.16) instead: $x \approx 0.79$ from simulated V and $x \approx 1.03$ from simulated D. While this uncertainty range seems large for x itself, it translates into much smaller ones in the estimated scaling exponents in Eq. (3.16) because of the specific way they depend on x. Its effect on the scaling argument is thus weak compared to the effects of the modified spectral slopes described above.

3.4 Asymmetric drag simulations versus modified prediction

When analyzing the spectra of the symmetric drag simulations, we have also checked the spectra of the asymmetric drag simulations. A finding from this analysis is that there is no obvious difference between the spectral slopes of the two sets of simulations (Fig. 3.3). This makes us suspect that the broad energy input in the barotropic energy spectrum remains as a key source of complexity in the asymmetric drag simulations and its effect may be largely separated from the effects of layer asymmetry. If we try to estimate x in the modified scaling prediction for the asymmetric drag simulations, the resulted x value is then hopefully similar to the one for the symmetric drag.

To test the hypothesis, we cannot estimate x from Eq. (3.16). This is due to the fact that Eq. (3.16) is derived from Eq. (3.1) and that Eq. (3.1) with V defined in Eq. (3.8) does not hold with asymmetric friction. We instead estimate x directly from Eq. (3.15), the scaling relation between T and L, without a reference to c_D. The simulated T itself turns out to be more sensitive to domain size and resolution

than L and V individually, but their impact on the scaling is small. For simplicity, we only show T for the sets of $k_d = 50$ simulations in Fig. 3.4. Indeed, plotting T against L reveals that the asymmetric and symmetric drags behave more or less the same: T scales with L in a similar manner regardless the complexities of layer asymmetry. Fitting the data from both the asymmetric and symmetric results gives $T \sim L^{-0.36}$ and $x \approx 0.72$, which is consistent with the estimate from the symmetric results alone.

Considering that T defined using V in Eq. (3.8) may have little relevance when the asymmetry becomes too strong, we have also tried avoiding V in the calculations by examining the simulated relation of D and L directly. As seen in Fig. 3.4, D has a simple power law dependence on L, and this dependence is very similar between symmetric drag and asymmetric drag simulations. A fit of the simulated D on L gives $D \sim L^{2.19}$. This result underscores that, while we cannot identified the relevant eddy velocity responsible for mixing in asymmetric drag simulations, at the very least D itself scales as L to some exponent which is close to (and thus can potentially be predicted by) the one for symmetric drag simulations.

Therefore, the moderate success of the modified scaling in predicting the symmetric as well as asymmetric drag results suggests the complexities due to the spectral nonlocality can be superposed on the complexities due to the layer asymmetry. The layer asymmetry affects the ability of drag to stop the cascade and results in different L between asymmetric and asymmetric drag simulations, but it does not change the scaling relations between L and other eddy statistics. Instead, the latter is primarily controlled by the effect of spectral nonlocality of barotropic energy input.

3.5 Equilibration without an inverse cascade

In this section, we investigate the distinct regime in the model with symmetric damping where the flows equilibrate without an inverse cascade. The fact that there is no inverse cascade can be told from the results in Fig. 3.2 that Lk_d is about the same as or even smaller than 10^0 in the symmetric drag simulations when $c_D k_d^{-1} > 10^0$. However, some seeming contradictions appear in this finding. The disappearance of inverse cascade when $c_D k_d^{-1} > 10^0$ is predicted by H99's theory, which argues that the friction becomes strong enough to directly stop the inverse cascade at the scale of deformation radius. Without an inverse cascade, Stone (1972)'s quasi-linear theory predicts that eddy scales and amplitudes would be determined by the properties of linear unstable modes and the given basic state. Therefore, they should be independent of the frictional strength. In these simulations, L, the meridional length scale of eddy mixing, can nonetheless become much smaller than k_d when the friction strengthens, and V and D can also be smaller than U and Uk_d^{-1}, respectively. Surprisingly, the eddy scaling in this regime matches the theoretical prediction by H99 (i.e. Eqs. (3.3), (3.6), and (3.7)). We here explain how these counterintuitive results emerge by examining the equilibration mechanism of these flows.

To study how the two-layer system equilibrates with a strong symmetric quadratic drag, we have taken a close look at the instantaneous streamfunction in these simulations. The simulated streamfunction has no meridional structure and tends to lock to certain zonal wavenumbers, indicating that the flows are dominated by the baroclinically unstable modes with gravest meridional wavenumber rather than isotropic eddies. This also suggests that it is the friction alone that directly stops the unstable modes from continuing to grow. The nonlinear terms and secondary instabilities do not have a chance to emerge so as to modulate the meridional scale of eddies and make it comparable to the zonal scale.

In addition to the instantaneous streamfunction fields, we can also see the dominance of meridional velocity (v) over zonal velocity (u) in the eddies and the dominance of baroclinic over barotropic component in the kinetic energy partitioning (Fig. 3.5). Consequently, the eddy fluxes can no longer be thought of as barotropic flows stirring baroclinic streamfunction (as in H99). It is also less meaningful to try to relate the zonal energy containing scale to meridional mixing because the zonal scale has no direct relation to the meridional scale. While the zonal eddy scale is controlled by the wavelength of linear unstable modes, the assumption that eddies would be isotropic, which is implicitly included in Stone (1972), does not apply to these simulations. Thus, Stone (1972)'s theory is inapplicable here.

What the linear dynamics of baroclinic instability controls here is instead the baroclinic eddy timescale ($T_\tau \equiv L/V_\tau$) defined by baroclinic meridional velocity (V_τ). This timescale represents the inverse linear growth rate of the system's gravest unstable modes. Equating T_τ to the timescale of frictional damping $(c_D V_\tau)^{-1}$ yields $L \sim c_D^{-1}$, which leads to a recovery of Eq. (3.3). If we further consider that baroclinic kinetic energy is proportional to the barotropic kinetic energy in baroclinic waves, $V_\tau \sim V$, then we can follow the same derivation described in Section 3.1 to regain Eqs. (3.6) and (3.7). Therefore, the eddy scaling in this regime is the same as the H99's prediction because of the same timescale constraint but with the eddy timescale determined by linear instability rather than turbulent cascade.

Additionally, it is worth noting that since the flows equilibrate directly with the gravest unstable modes, the equilibrated eddy statistics are sensitive to initial conditions. The simulations analyzed above are all integrated from the infinitesimal perturbations and go through the same linear baroclinic growth stage, so the excited modes and T_τ in these simulations are the same (Fig. 3.5). To demonstrate the initial condition dependence, we have integrated another set of simulations with varying c_D. These new simulations are initiated with the streamfunction field at the last output

time step of the $c_D k_d^{-1} = 10^{-1}$ simulation integrated from infinitesimal perturbations until statistically steady state (i.e. from the set of simulations analyzed in Fig. 3.2). They are then integrated until the new statistically steady state is achieved. During this transition, the flows initially occupied by isotropic eddies and filaments gradually spin down and are eventually taken over by the unstable modes. Therefore, the meridional-to-zonal kinetic energy ratio is still close to one. However, the unstable modes emerged at the statistically steady state are different, in general, so the ratio of baroclinic-to-barotropic kinetic energy and T_τ exhibit sensitivity to initial conditions (Fig. 3.5).

3.6 Linear versus quadratic drag

While our analysis focus on the simulations with the more geophysically relevant quadratic drag, it is the linear drag that is more commonly used in previous studies of this type. To better link our results to this literature, we have conducted additional simulations with linear drag. We plot the diffusivity D diagnosed from these linear drag simulations along with the ones from the quadratic drag simulations in Fig. 3.6. The two set of simulations share the identical setting except for the form of drag. The key distinction of a linear drag from a quadratic drag is that it defines a timescale rather than a length scale. Its strength is measured by the inverse damping timescale (κ as defined in LH95). To allow a straightforward comparison between two forms of drag, we define an effective damping timescale $\kappa_e \equiv c_D|\nabla\psi_2|$ for the quadratic drag simulations, where $|\nabla\psi_2|$ is the bottom layer rms velocity horizontally averaged over the domain (an internal scale diagnosed from the simulations). With this definition, the results of quadratic and linear collapse to a single line in Fig. 3.6, indicating they share the same eddy scale dependence on damping strength.

The possibility to map the linear to quadratic drag simulations further suggests that the scaling relations and theoretical consideration in this study may also help explain the dependence on linear drag, such as why the linear drag itself can stop the cascade alone (Smith and Vallis 2002). If we take the theory with the modified spectral slopes described in Section 3.3, but in addition use the approximation $c_D \sim \kappa V^{-1}$ in the expression for V in Eq. (3.16) we get

$$V \sim \kappa^{-(2+x)/x} \tag{3.18}$$

As expected, this is indeterminate for x = 0 (the H99 scaling) but is well-defined for $x > 0$. Substituting this scaling for V into the expression for L and D, we find

$$L \sim \kappa^{-2/x}, \tag{3.19}$$

$$D \sim \kappa^{-(4+x)/x}. \tag{3.20}$$

For $x \approx 1.03$ estimated from the D of symmetric quadratic drag simulations in Section 3.3, this implies $D \sim \kappa^{-4.88}$. This scaling is indicated with the sloping line in Fig. 3.6 and is close to the least-squared estimate obtained from the symmetric linear drag simulations, $D \sim \kappa^{-4.52}$. The reasonable fit to the simulated results suggests that this way of describing the results in terms of a modified spectral slope is consistent between the simulations with two forms of drag.

There is however a particular aspect of which the linear drag acts differently from the quadratic drag. While in strong symmetric quadratic drag simulations the eddies equilibrate linearly, they are damped to zero in strong symmetric linear drag simulations when the inverse damping timescale is larger than the growth rate of the most unstable modes. (With linear potential vorticity damping, that is, with equal damping of winds and temperature, stabilization occurs precisely when the damping

is larger than the growth rate of most unstable inviscid mode, but equal frictional damping in both layers with no thermal damping is sufficient to produce the same qualitative result.) In contrast, quadratic damping can never stabilize a flow that is unstable in the absence of the damping, since the strength of the damping is infinitesimal when the wave is infinitesimal. It only interferes with the baroclinic instability once the wave grows sufficiently that the damping timescale and the timescale of baroclinic growth become comparable.

3.7 A comparison with TY06

The modified scaling argument present in this study shares with LH95 the same physical picture for eddy heat fluxes, which are interpreted as generated by the stirring of background mean temperature (baroclinic streamfunction) gradient by the barotropic energy-containing eddies. We have proposed that focusing on the spectral shapes and their departure from Kolmogorov's scaling is a useful way of obtaining modified scaling to fit our simulations, with quadratic symmetric, quadratic asymmetric, linear symmetric, and linear asymmetric drags. However, its relevance to the linear asymmetric drag case is confusing given the findings in TY06, where the eddy heat fluxes are described as due to the systematic meridional drift of coherent vortices carrying temperature signatures.

In TY06's analyses, they described a strong anticorrelation between the instantaneous baroclinic streamfunction (τ) and barotropic vorticity ($\nabla^2\psi$) (c.f. their Fig. 4) to emphasize this role of vortices in heat transport. Similar to those shown in TY06, in Fig. 3.7, we present scatterplots of τ and $\nabla^2\psi$ (normalized by k_d and U) along with the snapshots of the two fields that are used to generate these scatterplots (to allow the finer structure in the snapshots to be recognized more easily, only one-ninth of the entire domain is shown). We have examined all our simulations and have se-

lected two of them as examples for this purpose. The two selected simulations are both with linear damping: the one with asymmetric drag has $\kappa k_d^{-1} U^{-1} = 0.25$ and the one with symmetric drag has $\kappa k_d^{-1} U^{-1} = 0.16$. We choose the former as it is among our simulations most comparable to the simulation shown in Fig. 4 of TY06. Accordingly, we then choose the later case that uses symmetric drag and has similar eddy scales (e.g. the simulated D for the two cases are similar as shown in Fig. 3.6).

For the asymmetric drag case, we see a scatterplot similar to the one shown in TY06 with the data partly organized into a few branches that correspond to individual vortices. It also confirms the presence of the anticorrelation between τ and $\nabla^2\psi$ as identified by TY06. When we look at the scatterplot of the symmetric drag case, there is however no evidence that τ and $\nabla^2\psi$ are correlated. The disappearance of the anticorrelation does not imply the disappearance of the coherent vortices, though. For both simulations, we have observed a hierarchy of vortices with different sizes in the snapshots of $\nabla^2\psi$ that look indistinguishable. Only when turning to the τ field, their differences start to be revealed. For the asymmetric drag case, the vortex structures are vivid in τ, with the warm core anticyclonic signature expected. By contrast, it is more difficult to identify the vortices in the symmetric drag case's τ field. Even if they exists, the sign of τ and $\nabla^2\psi$ at their cores is not systematic. Instead, there is a cluster of data around the origin in the $\tau - \nabla^2\psi$ scatterplots, corresponding to the long thin filaments occupying most of the domain and seen in both $\nabla^2\psi$ and τ fields. In this regard, a nonnegligible portion of τ anomalies is not within the vortices but is within the filaments aroused from the baroclinic forward cascade. One key to reconcile these two viewpoints would therefore be an understanding of the partitioning of the heat transport between vortices and passive filaments.

The simplest explanation for the thermal structure of the vortices described in TY06 is that the lower level winds in the vortices that would otherwise be barotropic are damped by friction, creating top-heavy equivalent barotropic vortices. Consistent

with thermal wind, this results in warm core anticyclones and cold core cyclones. Given these thermal signatures, the vortex dynamics in the presence of the mean thermal wind becomes a candidate for organizing heat transfer, in competition with the passive tracer-like advection of the temperature field. Yet, in the case of symmetric damping there is no reason to expect this kind of equivalent barotropic structure. By symmetry, the eddy kinetic energies in the two layers must have identical statistics in this case. This may explain why we only observe the anticorrelation of τ and $\nabla^2\psi$ in the asymmetric but symmetric drag case. Moreover, in our results, the scaling relationships for diffusivity and the eddy scales look identical in the symmetric and asymmetric drag cases in the limit of weak damping (Figs. 2 and 6). If the vortices in the symmetric drag cases can have no systematic temperature signal, a vortex-dominated heat flux is difficult to visualize. By implication, if we plausibly want the very similar results with asymmetric drag to have the same physical explanation as in the symmetric drag case, it seems justified to consider both as dominated by the same dynamics when damping is weak.

For stronger damping, there are clearly important differences between the symmetric and asymmetric drag cases (Figs. 2 and 6). When the nondimensional damping strength is larger than one, the flows are at another limit described in Arbic and Scott (2008) and Arbic and Flierl (2004). Our current speculation is that TY06 dynamics is relevant for intermediate values of the damping strength in the asymmetric drag case, interpolating between that limit of strong damping and the weak damping regime for which the scaling relations discussed here are relevant. (We restrict our discussion to cases in which the domain size is not a relevant parameter). This intermediate regime is very important, being in a meteorological and oceanic relevant parameter range (H99; Arbic and Scott 2008). The analysis in TY06 likely provides more insights to the dynamics in this regime, even though we cannot at this time offer a coherent theory that simultaneously covers all of these regimes.

3.8 Homogeneous and inhomogeneous comparison

It is natural to question how these homogeneous turbulence results carry over to inhomogeneous flows. As the first step, we have explored an inhomogeneous two-layer quasigeostrophic model with channel geometry. The equation of the model is

$$\frac{\partial q_i}{\partial t} + J(\psi_i, q_i) = -\kappa_T(-1)^i \frac{(\tau - \tau_E)}{\lambda^2} + \delta_{i2}\mathcal{D}_i(c_D) - \nu\nabla^6\psi_i, \tag{3.21}$$

where $q_i = \nabla^2\psi_i + (-1)^i(\psi_1 - \psi_2)/(2\lambda^2)$ is potential vorticity and ψ_i is streamfunction for upper ($i = 1$) and lower ($i = 2$) layers. $\mathcal{D}(c_D)$ represents the quadratic drag in the same form as Eq.(3.26) and $\nu\nabla^6\psi$ is the hyperviscosity term. Except the hyperviscosity term, the inhomogeneous model is only distinct from the homogeneous model in that its baroclinic streamfunction ($\tau = (\psi_1 - \psi_2)/2$) is relaxed to a zonally symmetric profile that produces a baroclinic jet. As this thermal relaxation is controlled by the inverse thermal damping timescale κ_T and the thermal equilibrium profile τ_E, we can construct a diffusive model (in the direction y) of the form

$$\frac{\partial \tau(y)}{\partial t} = \frac{\partial}{\partial y}(D_e(y)\frac{\partial \tau(y)}{\partial y}) - \kappa_T(\tau(y) - \tau_E(y)) \tag{3.22}$$

where D_e is the effective dimensional diffusivity in the form $D_e(y) = -\partial_y\tau(y)\lambda d$ and d is the nondimensional diffusivity measured from the homogeneous model. That is, given that the two models have the same nondimensional frictional damping strength (i.e. $c_D k_d^{-1} = c_D\lambda$), we can obtain $d = Dk_dU^{-1}$ from the simulated diffusivity D, k_d, and U in the corresponding homogeneous model simulation to solve Eq. (3.22) for the equilibrated temperature and eddy heat flux.

Fig. 3.8 shows how the eddy heat fluxes predicted by this diffusive model compare to the inhomogeneous model simulations with the parameters $\beta = 0$, $\lambda = \sqrt{2}^{-1}700\ km$, $\kappa_T^{-1} = 20\ days$, $\tau_E = -U_E\sigma\tanh(y/\sigma)$, and $U_E = 20\ ms^{-1}$. These

are chosen to be mostly the same as in Zurita-Gotor et al. (2014), and the eddy heat fluxes are also shown in the temperature (θ) unit (K) through the conversion $\theta \equiv \tau\psi_0^{-1}\theta_0$ with $\theta_0 = 290K$ and $\psi_0 = 2.45 \times 10^8\ m^2 s^{-1}$. The inhomogeneous model's resolution and domain size in the zonal direction are also kept the same as the homogeneous model after nondimensionalized. This is to ensure the results are not affected by these model details. Evidently, the diffusive model successfully predicts the eddy heat flux's meridional structure both when the radiative equilibrium width of baroclinic jet (σ) and when the frictional (quadratic) damping strength (c_D) are varied.

This comparison has previously been provided by Pavan and Held (1996) with non-zero β and linear damping (c.f. their Fig. 9). Our case with zero β is even simpler in the sense that there is no ambiguity whether to diffuse temperature or potential vorticity, since the temperature and the potential vorticity in both layers are all proportional to each other in this limit of the homogeneous model. In the inhomogeneous model simulations we analyzed, the eddy momentum fluxes are also negligible. Consistent with Pavan and Held (1996), our result again supports the relevance of homogeneous scaling for inhomogeneous flows. We note that, as in Pavan and Held (1996), thermal damping has been added to the homogeneous model when calculating d as this is an essential feature of how the inhomogeneous model is forced. Since the thermal damping is not included in the homogeneous simulations analyzed in the previous sections, the d obtained from the homogeneous simulations with thermal damping in general is different from those without thermal damping and reported in Fig. 3.2. In the case considered here, it has a very modest effect on the eddy scales and fluxes, so d remains close to the value that we have shown there. Yet, some systematic deviations from the homogeneous predictions, possibly due to this extra parameter or other subtle differences between the two models, are under investigation.

3.9 Discussion and conclusions

We have studied the statistically steady state solutions of a $\beta = 0$ homogeneous two-layer quasigeostrophic model with quadratic drag. In this model, the statistically steady state is a function of a single parameter, the ratio of a frictional length scale $L_D = C_D^{-1}H$ (where C_D is the nondimensional coefficient in the surface stress and H is the depth of the layer to which the stress applied) and the radius of deformation $\lambda = NH/f$ or, equivalently in terms of our model notations, the ratio of their wavenumbers: $c_D k_d^{-1}$. We have run the model with a range of $c_D k_d^{-1}$ in the attempt to understand the aspects of its dynamics that complicate the eddy scaling theory proposed by Held (1999, hereafter H99).

The first aspect we focus on are the asymmetry between upper and lower layers caused by the presence of drag in the lower layer only. This layer asymmetry in drag makes the flow equivalent barotropic. Therefore, when the damping is stronger, while both asymmetric and symmetric drag become more efficient at stopping the inverse cascade, the former is relatively more inefficient than the latter. Eddy scales are then decreasing less slowly with the damping strength in the cases with asymmetric than with symmetric drag. On the other hand, when the damping is weak and the flow is largely barotropic, there is little difference between models with asymmetric or symmetric drag, as long as one rescales the strength of the damping so that the barotropic flow is damped at the same strength in each case.

In the second aspect, we argue that the spectrally nonlocal baroclinic-to-barotropic energy transfer results in the deviation from Kolmogorov's inertial range theory, which is a central assumption in Larichev and Held (1995, hereafter LH95) that is then considered in H99. A modest modification on this assumption and then H99's scaling by assuming barotropic spectral energy flux has a wavenumber dependence (k^{-x}) is adopted to explain the observed weaker power law dependence of eddy scales on the damping strength ($L \sim c_D^{-0.58}$, $V \sim c_D^{-0.78}$, and $D \sim c_D^{-1.24}$). We do not provide a

theory for x, but find that this expression, with $x \approx 0.72$ directly estimated from the simulations, gives self-consistent fits to the simulations, although some uncertainty exists on how it is best estimated. We also confirm that the same modified scaling applies to both the symmetric and asymmetric drag simulations when the damping is weak, so the complexity related to the spectral nonlocality can be largely distinguished from the one related to the layer asymmetry. Finally, with sufficiently strong symmetric damping a regime is found in which the equilibrated flows are dominated by the linear unstable modes directly stabilized by friction, so the linear dynamics controls the eddy scaling and the solutions are initial-condition dependent.

In addition to quadratic drag, we examine the homogeneous model simulations with linear drag and find that their eddy scales are very similar to those in the quadratic drag simulations once a proper relation between the damping strengths of the two forms of drag is defined. Due to this simplicity, the modified scaling for the quadratic drag case also predicts the scaling for the linear drag case, which resolves the problem of the original theories of LH95 and H99 that struggle to provide a well-defined prediction when the halting mechanism is linear drag. After that, we discuss the alternative approach of Thompson and Young (2006), in which heat transport in their bottom linear drag simulations is found to be due to the drift of vortices with systematic temperature signatures. This is also observed in our asymmetric drag simulations. However, the similarity in the behavior of our model with symmetric and asymmetric drags when the damping is weak, makes it hard to interpret our results in this fashion, since the model with symmetric drag produces vortices with no systematic temperature signals. Therefore, we leave this issue unresolved.

Last, following the approach of Pavan and Held (1996), we compare a set of inhomogeneous channel model simulations with bottom quadratic drag to the solution of a diffusive energy balance model with its diffusivity predicted by the homogeneous model. At least for the cases that we have looked into, we obtain some encouraging

results. In fact, with $\beta = 0$, this is an especially simple system to perform such a comparison, in large part because eddy momentum fluxes play less of a role here than in the case with non-zero β, resulting in the absence of eddy-driven jets. Further study of this comparison in this idealized system could shed light on any fundamental limitations to the value of the homogeneous limit.

Together these results help us to better interpret H99's estimate on the extent of inverse cascade controlled by surface friction in idealized models of the extratropical troposphere. Relative to Eq. (3.3)'s prediction, accounting for spectral nonlocality helps the cascade stop earlier, while introducing layer asymmetry allows a larger cascade range. The two counteracting effects both operate at $L_D\lambda^{-1} = (f/N)C_D^{-1} \approx 10$, the relevant regime for the extratropical troposphere over oceans ($f/N \approx 10^{-2}$ and $C_D \approx 10^{-3}$), so Eq. (3.3) ends up being a fair estimate. If a higher surface roughness, such as for the typical land surface value ($C_D \approx 10^{-2}$), is considered, the prediction by Eq. (3.3) may underestimate the eddy length scale at which the surface friction halts the cascade. The eddy kinetic energy and diffusivity may also be larger than expected. As it is a meteorological relevant regime, the effects of friction being confined near the surface clearly need a better quantification for a more precise estimate. This is not addressed here and is a limitation of this study.

Another limitation we emphasize is that the modified scaling presented in this study is not a predictive theory but rather an economical description, as we directly estimate the wavenumber dependence of the barotropic spectral energy flux (i.e. k^{-x}) from the simulations. To understand how this flux is determined, one would have to study the triad interactions and the associated spectral energy transfers into the barotropic mode. Added on these uncertainties are also the somewhat fuzzy connection assumed in LH95 between the spectrally local and spectrally integrated properties, where the assumption that the energy containing eddies producing the eddy heat flux can be described by a single wavenumber (Smith and Vallis 2002) and the

variations of correlation between the barotropic velocity and baroclinic streamfunction in the mixing length theory. Still, we are convinced that this modification of LH95's scaling may capture some of the important physics. The exponent of the simulated power law relation is reasonably well-defined and the spectral slope discrepancy between the simulations and theory is qualitatively consistent between our simulations and those reported by LH95. It at the very least helps us better connect the understanding of two-layer baroclinic turbulence and of barotropic turbulence.

These baroclinically unstable homogeneous models are also potentially relevant to the ocean mesoscale eddy parameterization problem. In this regard, it is useful to compare our results to those in Jansen et al. (2015). They have parameterized the eddy heat fluxes in a two-layer primitive-equation channel model using an empirical fit to relate barotropic and bottom kinetic energies as a key assumption. In the limit of $\beta = 0$, they use the constant eddy timescale assumption proposed by LH95 (i.e. Eq. (3.9)) to form a closure. Their scheme takes into account layer asymmetry due to the bottom drag (and the different layer depths) but assumes no further adjustments to LH95's scaling. This assumption may be adequate for parameterizations in which there are many other uncertainties, but the constant eddy timescale in LH95 is not supported by our results. Jansen et al. (2015) has also found some issues with LH95's scaling when nonzero β is included. There are a number of results in the literature, using a variety of models, that differ regarding the utility of Held and Larichev (1996) theory, the extension to nonzero β of the LH95's scaling (Smith and Vallis 2002; Barry et al. 2002; Lapeyre and Held 2003; Zurita-Gotor 2007; Thompson and Young 2007; Jansen and Ferrari 2013a; Jansen et al. 2015; Chai 2016). A natural question is then how much of the mismatch to LH95's theory with nonzero β can be attributed to deficiencies that are already present in the absence of β. Building on the results presented here, we will address parts of this question in the next chapter.

In the context of studies on eddy scaling in the homogeneous two-layer quasi-geostrophic model, this work resides at the simplest extreme on the model hierarchy. In fact, we have taken an extra step backward to investigate a more unrealistic model with mechanical drag appearing symmetrically between the two layers. This even simpler model configuration, in which all eddy statistics are identical in the two layers, offers the potential for a cleaner comparison between a self-stirred baroclinically unstable flow and the stirred barotropic model. By studying this limit, we have emphasized knowledge gaps between baroclinic and barotropic turbulence. We believe that this is a relevant limit in which to try to solidify our understanding of eddy statistics in these turbulent baroclinically unstable flows and to provide a more solid foundation for our understanding of more realistic models.

	Form of Friction	k_{max}	k_d	IC	Damping Strength
◯	asym. quadratic	128	50	I	$10^{-3} \leq c_D k_d^{-1} \leq 10^{0}$
◯	sym. quadratic	128	50	I	$10^{-3} \leq c_D k_d^{-1} \leq 10^{0}$
+	asym. quadratic	256	100	I	$10^{-4} \leq c_D k_d^{-1} \leq 10^{-0.5}$
+	sym. quadratic	256	100	I	$10^{-4} \leq c_D k_d^{-1} \leq 10^{-0.5}$
×	asym. quadratic	128	10	I	$10^{-1.5} \leq c_D k_d^{-1} \leq 10^{2}$
×	sym. quadratic	128	10	I	$10^{-1.5} \leq c_D k_d^{-1} \leq 10^{2}$
△	sym. quadratic	128	10	S	$10^{-1} \leq c_D k_d^{-1} \leq 10^{2}$
□	asym. linear	128	50	I	$10^{-1} \leq \kappa k_d^{-1} U^{-1} \leq 10^{0}$
□	sym. linear	128	50	I	$10^{-1} \leq \kappa k_d^{-1} U^{-1} \leq 10^{0}$

Figure 3.1: A summary of the parameter settings for each set of numerical simulations: (from left to right) the chosen form of large scale friction, maximum wavenumber resolved (k_{max}), wavenumber of deformation radius (k_d), initial condition (IC), and the explored range of nondimensionalized damping strength. For initial condition, "I" refers to the simulations integrated from the infinitesimal perturbations prescribed in the same way as LH95, and "S" refers to the simulations integrated from the simulated streamfunction field taken from the $c_D k_d^{-1} = 10^{-1}$ run that is integrated from the first initial condition until statistically steady state.

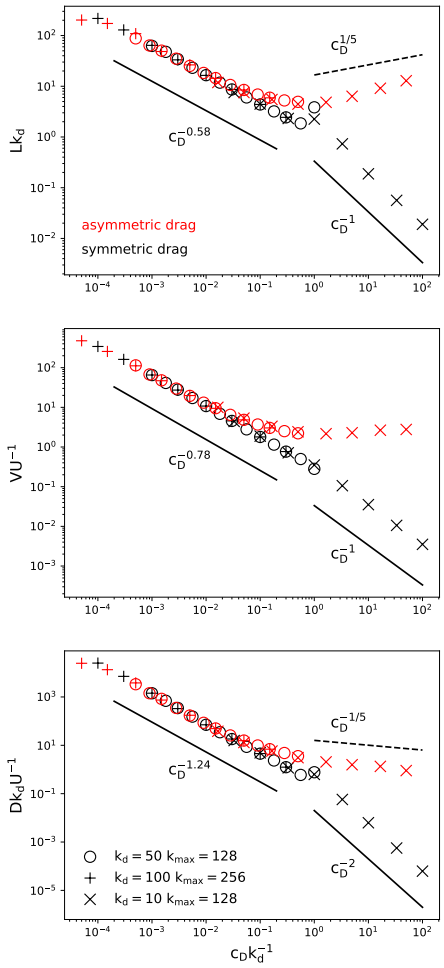

Figure 3.2: Eddy scales in the asymmetric and symmetric drag simulations: (from top to bottom) eddy length scale (L), velocity scale (V), and diffusivity (D) as a function of damping strength ($c_D k_d^{-1}$). Simulations with the asymmetric drag are colored as red and with the symmetric drag are colored as black. The different symbols refer to the model settings with different domain sizes and spectral resolutions (Fig. 1). For an easier comparison, all the asymmetric drag results are shifted by a factor of two along x-axis, i.e. from $c_D k_d^{-1}$ to $c_D k_d^{-1}/2$ (which would be the effective drag if the drag was symmetric). In each panel, the top left solid line indicates the power law scaling estimated from a least-squared fit of the data in the $k_d = 50$, $c_D k_d^{-1} < 10^0$ symmetric drag simulations. The bottom right solid line indicates the power law scaling predicted by H99's theory, and the top right dashed line indicates the scaling proposed by Arbic and Scott (2008) in the strong asymmetric drag limit.

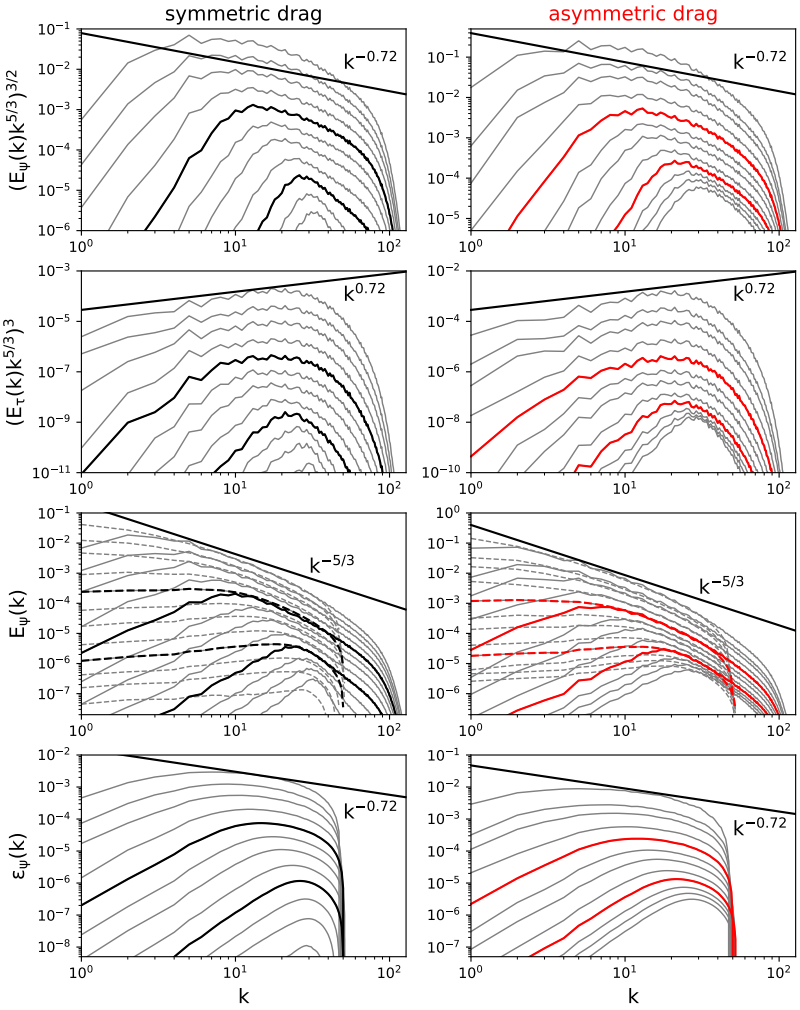

Figure 3.3: Deviations of the simulated spectrum shapes from the theory in the symmetric and asymmetric drag simulations ($k_d = 50$ only): (from top to bottom) compensate spectra of barotropic energy $(E_\psi(k)k^{5/3})^{3/2}$, compensate spectra of baroclinic available potential energy $(E_\tau(k)k^{5/3})^3$, barotropic energy spectra $E_\psi(k)$ (solid) versus the corresponding predictions by $C_\psi\epsilon_\psi(k)^{2/3}k^{-5/3}$ (dashed), and barotropic energy flux spectra $\epsilon_\psi(k)$. In each panel, the spectra for the $c_D k_d^{-1} = 10^{-1}$ and $c_D k_d^{-1} = 10^{-2}$ simulations are colored, with the rest of the cases plotted in gray. We have chosen $C_\psi = 7$ to obtain an overall reasonable fit for both sets of simulations, but we notice that this results in a slight overestimation for the symmetric drag simulations and a slight underestimation for the asymmetric drag simulations (for reasons unclear to us). The black solid line indicating the slope k^{-x} or k^x with $x \approx 0.72$ is estimated from the simulated L using Eq. (3.16) (see text for more details).

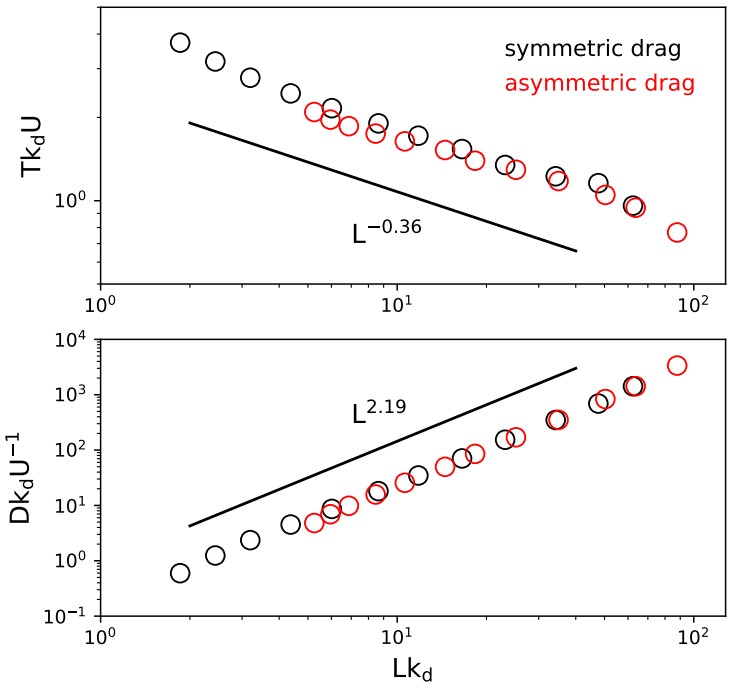

Figure 3.4: Relations among eddy scales in the asymmetric and symmetric drag simulations ($k_d = 50$ only): relations of eddy timescale (T) and eddy diffusivity (D) with eddy length scale (L). The slope of the black line is computed from the least-squared fit of the data from both the asymmetric and symmetric drag simulations (i.e. all the data points shown in the plot).

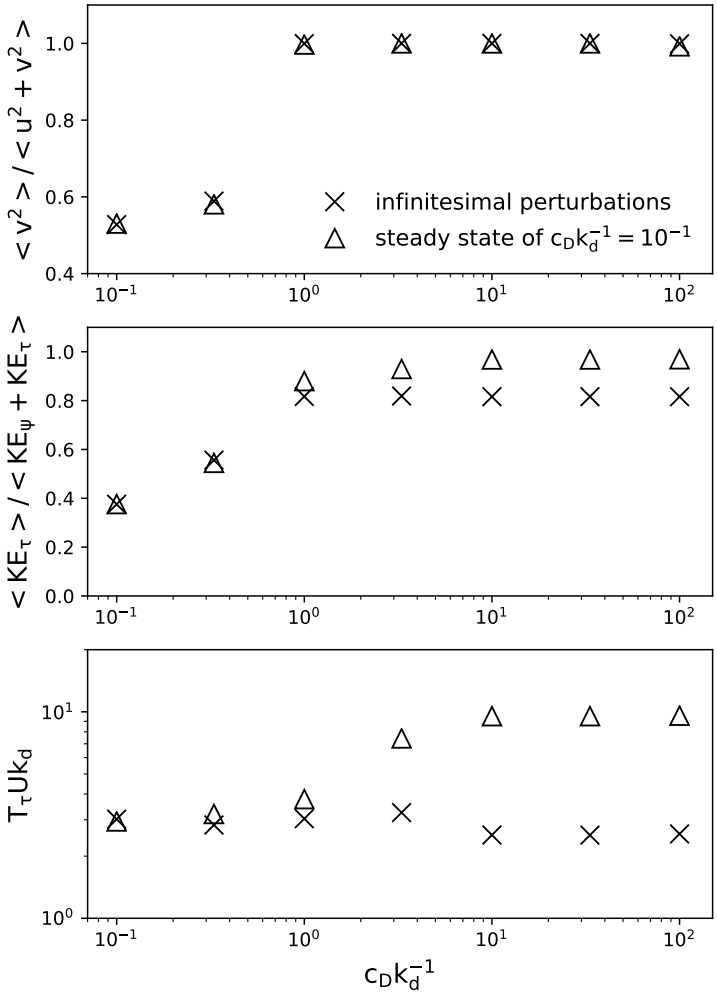

Figure 3.5: Initial condition dependence of steady state flow properties in the strong symmetric drag regime ($k_d = 10$ only): (from top to bottom) meridional kinetic energy ($\langle v^2 \rangle /2$) to total kinetic energy ($\langle u^2 + v^2 \rangle /2$) ratio, baroclinic kinetic energy ($\langle KE_\tau \rangle$) to total kinetic energy ($\langle KE_\psi + KE_\tau \rangle$) ratio, and baroclinic timescale (T_τ defined as the ratio of eddy length scale L and baroclinic meridional velocity V_τ) as a function of $c_D k_d^{-1}$. Two initial conditions are considered: the one with infinitesimal perturbations in the streamfunction field as described in LH95 (cross) and the other one as the steady state streamfunction field taken from the $c_D k_d^{-1} = 10^{-1}$ simulation (triangle).

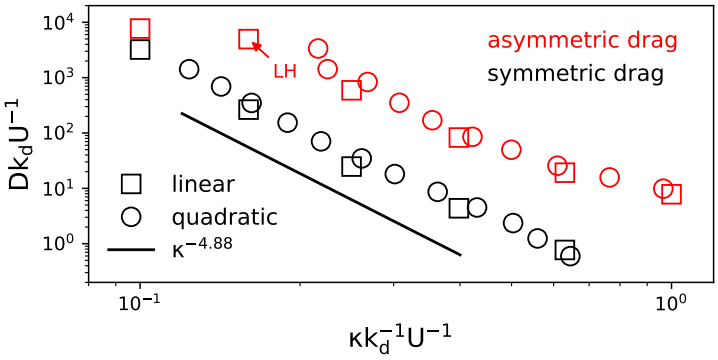

Figure 3.6: Eddy scales in the linear and quadratic drag simulations: diffusivity (D) diagnosed from linear (square) and quadratic (circle) drag simulations as a function of linear damping strength $\kappa k_d^{-1} U^{-1}$. The two set of simulations are mapped to each other by comparing κ to the effective linear damping strength (κ_e, defined in the text) for the quadratic drag simulations. LH denotes for the run that shares the same parameter setting as the case I simulation in LH95. The solid line indicates the scaling prediction discussed in the text.

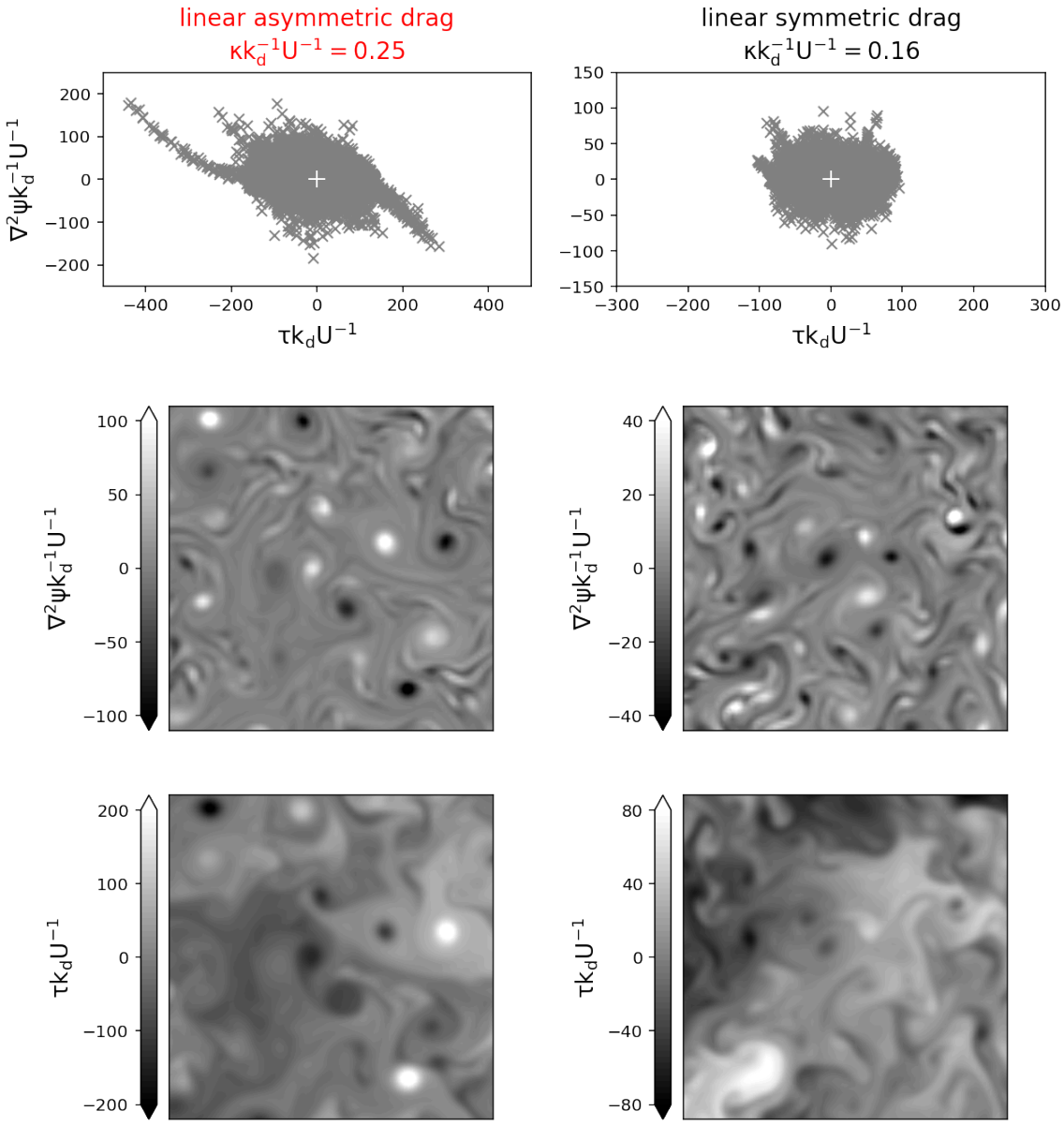

Figure 3.7: Scatterplots of baroclinic streamfunction (τ) and barotropic vorticity ($\nabla^2\psi$) and the snapshots of the two fields: a simulation using linear asymmetric drag with $\kappa k_d^{-1}U^{-1} = 0.25$ (left) and another using linear symmetric drag with $\kappa k_d^{-1}U^{-1} = 0.16$ (right) are shown to compare with the simulations of Thompson and Young (2006).

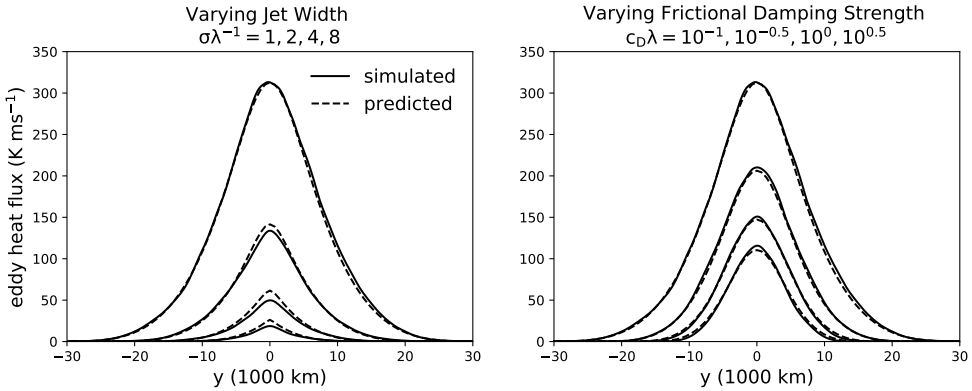

Figure 3.8: Eddy heat fluxes in the channel model simulations: the meridional structure of eddy heat fluxes simulated from the channel model (Eq. (3.21); solid) and the predictions by a diffusive energy balance model with the diffusivity predicted by our homogeneous model simulations (Eq. (3.22); dashed). Two sets of simulations are examined: one with varying jet width at radiative equilibrium (σ) and one with varying frictional quadratic damping strength (c_D). The first set of simulations has a fixed $c_D\lambda = 10^{-1}$ and $\sigma\lambda^{-1} = 1, 2, 4, 8$ (left); the second set of simulations has a fixed $\sigma\lambda^{-1} = 8$ and $c_D\lambda = 10^{-1}, 10^{-0.5}, 10^{0}, 10^{0.5}$ (right). λ is deformation radius. The rest of the model parameters is described in the text.

3A Equations of the model

Following the notations of LH95, the potential vorticity (Q) equations for the two equal-depth layers are

$$\partial_t Q_1 + J(\Psi_1, Q_1) = -\nu\nabla^8 Q_1 + \mathcal{D}_1, \tag{3.23a}$$

$$\partial_t Q_2 + J(\Psi_2, Q_2) = -\nu\nabla^8 Q_2 + \mathcal{D}_2, \tag{3.23b}$$

where the subscripts 1 and 2 refer to the top and bottom layers, respectively. The potential vorticity Q are related to the total streamfunction Ψ by

$$Q_1 = \nabla^2\Psi_1 + k_d^2(\Psi_2 - \Psi_1)/2, \tag{3.24a}$$

$$Q_2 = \nabla^2\Psi_2 + k_d^2(\Psi_1 - \Psi_2)/2, \tag{3.24b}$$

and Ψ contains a prescribed zonal mean part and an eddy part that varies in time and space,

$$\Psi_1 = -Uy + \psi_1(x, y, t), \tag{3.25a}$$

$$\Psi_2 = Uy + \psi_2(x, y, t). \tag{3.25b}$$

In the r.h.s. of Eq. (A1), the subgrid-scale dissipation is parameterized as a ∇^8 hyperviscosity and the large-scale dissipation $\mathcal{D}$ is in a specific form of quadratic drag that assumes the surface stress is parallel to the eddy velocity (Grianik et al. 2004; Arbic and Scott 2008),

$$\mathcal{D}_1 = -c_D(\partial_x(|\nabla\psi_1|\partial_x\psi_1) + \partial_y(|\nabla\psi_1|\partial_y\psi_1)), \tag{3.26a}$$

$$\mathcal{D}_2 = -c_D(\partial_x(|\nabla\psi_2|\partial_x\psi_2) + \partial_y(|\nabla\psi_2|\partial_y\psi_2)). \tag{3.26b}$$

Altogether, the set of equations has four parameters: the wavenumber of deformation radius k_d, the mean vertical shear U, the hyperviscosity coefficient ν, and the wavenumber of frictional length c_D. We choose to nondimensionalize the equations by k_d and U and leave the two dimensionless parameters as $\nu U^{-1} k_d^7$ and $c_D k_d^{-1}$. In this study, we have assumed the solutions (in the parameter space we explore) have no dependence on $\nu U^{-1} k_d^7$, since ν is set adaptively during the integration as described in Smith and Vallis (2002) and we do not have an explicit control on its value. This also assumes the solutions after nondimensionalization is independent of U, which is confirmed by Arbic and Scott (2008). The value of $U = 0.005$ that we use is simply chosen for convenience in the comparison with the LH95 simulations.

Chapter 4

Eddy equilibration in two-layer QG models: the roles of β

Expanding on the revised argument proposed for the $\beta = 0$ limit in Chapter 3, this chapter proceeds to study the roles of β in the homogeneous two-layer QG model. We focus particularly on restoring the connection between the diffusivity scaling in barotropic turbulence, in which the turbulence is generated by stirring that is localized in wavenumber space, and diffusivity scaling in two-layer turbulence, in which the turbulence is generated by baroclinic instability, as well as between $\beta = 0$ and nonzero β.

4.1 Introduction

As discussed in the previous chapters, the maintenance of global climate is in a large part determined by the heat fluxes of baroclinic eddies in the atmosphere and ocean. Thinking of these eddies as macroturbulence and their heat fluxes as turbulent diffusion, the pursue of a quantitative understanding of these fluxes has had a long history (Held 1999). To date, our theoretical framework for them is mostly founded on the seminal work by Rhines (1975, 1977) and Salmon (1978, 1980), where they studied

the homogeneous two-layer quasigeostrophic (QG) turbulence as the prototype of the complex geophysical flows in the real world. In these papers, they established the theoretical connection between the two-layer QG turbulence and the barotropic QG turbulence. They postulated that the energy in the two-layer turbulence is initially generated in the baroclinic mode and transferred to barotropic mode at the deformation radius. Similar to the barotropic turbulence constrained by the two-dimensional geometrical effect, they further proposed that barotropic eddy kinetic energy in the two-layer turbulence also cascades inversely to larger horizontal and vertical scales. This results in most of energy being barotropic and predominately at larger scale in the two-layer turbulence, and the baroclinic streamfunction (an analog of temperature) acts essentially like a passive tracer in the barotropic turbulence mixed by the barotropic flows. A useful starting point for studying the diffusivity for the heat flux in the two-layer turbulence is therefore to quantify the diffusivity for the passive tracer in the barotropic turbulence.

For barotropic turbulence to maintain a statistically steady state, energy is typically input at a small forcing scale with a prescribed constant energy injection rate (ϵ). To the extent that most energy cascade to large scales, ϵ can also be approximated as the rate of inverse cascade. This inverse cascade can be halted by two mechanisms, and the equilibrated eddy scales and the fluxes of passive tracers then depend on how they halt the cascade. The first mechanism is the large-scale friction, which stops the cascade by dissipating and removing the energy from the system. When the friction is in the form of quadratic drag, the frictional damping strength is an inverse length scale or a wavenumber (c_D), as discussed in Chapter 3. Suppose the forcing scale and domain size are irrelevant in the parameter regime of interest. The system is then characterized by only two parameters: ϵ and c_D. By dimensional analysis, the eddy diffusivity (D) should scale as

$$D \sim \epsilon^{1/3} c_D^{-4/3} \tag{4.1}$$

(Grianik et al. 2004). While we did not explicitly discuss this expression in Chapter 3, it is equivalent to the combination of Eqs. (3.2)-(3.4). The dimensional analysis here merely provides a shortcut for its derivation. The second mechanism is the effect of prescribed mean meridional planetary vorticity gradient (β). The presence of β breaks the isotropy of the equations and channels the energy into Rossby waves and zonal jets that do not participate directly in meridional mixing. When β is large enough to prevent the cascade alone, it is expected the diffusivity to be depended on β rather than friction. Then, by dimensional analysis, the diffusivity should scale as

$$D \sim \epsilon^{3/5}\beta^{-4/5} \tag{4.2}$$

(Smith et al. 2002). Again, this expression was not extensively discussed in Chapter 2, but it is equal to the combination of Eqs. (2.1)-(2.2).

Considering the full parameter range where both halting mechanisms may play a role, Kong and Jansen (2017, hereafter KJ17) found in the numerical simulations that the diffusivity normalized by Eq. (4.1) can be solely described as a function of a single nondimensional parameter $\epsilon^{-1/5}\beta^{3/5}c_D^{-1}$ (c.f. their Fig. 3). Suppose the forcing scale and domain size are not relevant, this parameter is the only dimensionless form in all the possible combination of ϵ, β, and c_D. Physically, it can be interpreted as the ratio of the characteristic halting wavenumber in the two limits, c_D and $\epsilon^{-1/5}\beta^{3/5}$, so it measures the relative importance of c_D and β in halting the cascade. In the limit that either of the two scales and its corresponding halting mechanism dominate, the functional form of diffusivity is expected to be the power law scaling in either Eq. (4.1) or (4.2). Connecting the two limits is a transition regime that is described by the theory in KJ17, in which they proposed that the diffusivity's parameter dependence has to be understood by examining the full wavenumber spectrum of the tracer flux, or, equivalently, the diffusivity spectrum. This is due to fact that the diffusivity in

this regime is sensitive to the collective effects of eddies at different wavenumbers propagating zonally at different phase speeds. Given the same eddy kinetic energy, the eddies mix the tracers less efficiently in the meridional when they propagate in the zonal direction and transport the tracers in a shorter meridional distance. This reduction in the effective correlation time between the eddies and the tracers is then determined by the extent of their zonal propagation, whose suppression on meridional mixing then differs according to the eddy phase speeds (Ferrari and Nikurashin 2010; Klocker et al. 2012; Chai 2016).

Applying the above barotropic turbulence's diffusivity theory to the two-layer turbulence requires two extra steps that take two notable differences between the two systems into account. The first is that energy input in the system and ϵ are not prescribed in the two-layer turbulence. For the two-layer (homogeneous) turbulence, the mean vertical shear (U), equivalently the mean gradient of baroclinic streamfunction, is externally given. The energy is generated through the eddy mixing that taps the available potential energy associated with the mean vertical shear,

$$\epsilon_p \equiv D_\tau U^2 k_d^2, \tag{4.3}$$

where D_τ is the heat flux diffusivity and k_d is the wavenumber of deformation radius (prescribed under QG assumption). Note that Eq. (4.3) is identical to Eq. (2.5), as the former is in terms of the two-layer QG model and the latter is of the continuously stratified Boussinesq system. Combining this energetic relation with Eq. (4.2) and taking $D = D_\tau$, Held and Larichev (1996) derived a closure theory for the two-layer turbulence. A potential pitfall in this theory stems from another notable difference between the barotropic and two-layer turbulence, where the latter has three distinct diffusivities. That is, D_τ for the heat flux, and D_u and D_l for upper and lower layer potential vorticity (PV) fluxes, respectively. The three diffusivities are intimately

related due to the vanishing of domain mean momentum and PV fluxes,

$$D_\tau \equiv D_u(1+\xi^{-1}) \equiv D_l(1-\xi^{-1}), \tag{4.4}$$

and they are identical only when the criticality ($\xi \equiv \beta^{-1}Uk_d^2$) approaches to infinity. Thus, without further justification, Held and Larichev (1996)'s theory is better regarded as being applied to only the strongly unstable flows where ξ is large. As for $\xi \approx O(1)$, Lapeyre and Held (2003, hereafter LH03) found in the numerical simulations that Eq. (4.2) actually fits best to D_l, the diffusivity for the lower layer PV flux. While there is still lack of sound reasoning for which (if any) of the three diffusivities in the two-layer turbulence Eq. (4.2) is best compliant to when ξ is not very large, this theory (and its variants) has indeed been shown capable of at least qualitatively explaining the eddy heat flux diffusivity in more sophisticated systems, including the two-layer QG channel model (Pavan and Held 1996; Zurita-Gotor 2007), the multi-layer Boussinesq channel model (Jansen and Ferrari 2013a), and a comprehensive global climate model (Barry et al. 2002). This continuing relevance over a spectrum of models then suggests that Eq. (4.2) and the dynamics of the barotropic turbulence alone are sufficient to explain the eddy heat flux in the β dominated regime.

Meanwhile, to study the diffusivity dependence on friction, Thompson and Young (2007, hereafter TY07) investigated the two-layer simulations with varying frictional damping strength of the bottom linear drag. They found that Eq. (4.2) with D identified as D_τ is only valid in a small range of intermediate β at best, so Eq. (4.2) is not the asymptotic limit as in the barotropic turbulence. More surprisingly, there appears to be no corner in the parameter space that D_τ is totally independent of friction: D_τ decreases with stronger damping for relatively small β but increases with stronger damping for relatively large β (c.f. their Fig. 3). This complicated friction dependence of the two-layer turbulence clearly is unexplained by the barotropic turbulence

theory. To develop a more complete theory for it requires a better clarification on how the two-layer turbulence is related to the barotropic turbulence.

In the attempt to fill this knowledge gap, we have, in Chapter 3, purposely studied a non-Earth-like setting of the homogeneous two-layer QG model that is arguably the simplest nontrivial limit one can get to isolate the essential differences between the two-layer and barotropic turbulence. The model is set up with quadratic drag appearing symmetrically between the two layers and β is set to zero, which ensures the eddy statistics in the two layers are identical and $D_\tau = D_u = D_l$. It is seen that the barotropic eddy kinetic energy spectrum of the flows does not develop a well-defined Kolmogorov's inertial range of inverse cascade that is typically seen in the barotropic turbulence stirred at small scales. Varying the strength of the quadratic drag, we also found the emergent diffusivity scaling dependence on the friction is different from the barotropic one, i.e., Eq. (4.1). There, we provided a heuristic argument that allow us to connect the two phenomena. In this chapter, we study how these findings about the differences in the $\beta = 0$ limit can be further extended to understand the differences when β is nonzero.

With the same quadratic damping strength in the two layers, we conduct a series of simulations where c_D and β are varied. In Section 4.2, we describe the c_D and β dependence of the simulated heat flux diffusivity (D_τ). We begin by presenting an overview of how our simulations compare with those in TY07 and KJ17. As in KJ17, we use the simulated barotropic eddy kinetic energy spectrum to estimate D_τ and to study the effect of mixing suppression due to the eddy propagation. Then we explore the potential of KJ17's generalized theory, modified with an extra assumption to take account of the deviation of barotropic eddy kinetic energy spectrum from Kolmogorov's theory, in predicting D_τ.

After that, we proceed to assess two scaling relations reported by previous studies in Section 4.3. We first discuss the performance of an empirical fit that is obtained in

Section 4.2 as a benchmark calculation. We then compare it to the fitting results of Eq. (4.2) with the simulated D_τ and D_l to illustrate how they can be reconciled with LH03's argument. This is followed by an analysis on the simulated variables related to the bulk mixing length theory and a brief investigation on the diffusivity scaling based on Rhines (1975)'s scale. Last, in Section 4.4, we summarize these findings and discuss their relations back to more realistic geophysical flows.

Before starting, we would like to underscore that our primary goal here is to report and describe the simulations in a context that could offer a cleaner comparison between the arguments and results of the previous studies. We do not attempt to provide a complete explanation or theory for our results. However, we believe the calculations and analyses presented in this study can serve as the stepping stone toward those ultimate goals.

4.2 Parameter dependence of D_τ

4.2.1 Overview of the simulations

We use the same model described in Chapter 3 to conduct a series of simulations in the parameter range: $10^{-3} \leq \tilde{c}_D \equiv c_D k_d^{-1} \leq 10^{-1}$ and $0 \leq \tilde{\beta} \equiv \beta k_d^{-2} U^{-1} < 1$. The tilde represents the nondimensionalization by U and k_d. All these simulations have quadratic drag with the same damping strength appearing in the two layers, and the $\tilde{\beta} = 0$ cases are exactly those reported in Fig. 3.2. We also noted that, because the drag appears in both layers, frictional destabilization in the subcritical flows is prevented and the $\tilde{\beta}$ range considered is the full range of the unstable flows. A careful check on the $\tilde{\beta} = 1$ simulations has confirmed that perturbations do not grow and the flows are stable. The definitions of the variables diagnosed from the statistically steady state of the simulations and discussed below are given in Table 4.1. We note

that they simply share the same definitions as in Eq. (3.8) but are recast in different notation in this chapter.

Fig. 4.1 provides an overview of all our simulations. In the left panel, we plot the nondimensionalized heat flux diffusivity ($\tilde{D}_\tau \equiv D_\tau k_d U^{-1}$) against $\tilde{\beta}$ and use different symbols to indicate the different values of $\tilde{c}_D$. This is purposely done for a direct comparison with Fig. 3 of TY07, whose simulations are conducted in the conventional way that has linear drag implemented only in the lower layer. In spite of the difference in the frictional form, the $\tilde{D}_\tau$ dependence in our simulations very much resembles to theirs. It is seen that $\tilde{D}_\tau$ is always reduced with increasing $\tilde{\beta}$ for a given damping strength, i.e., $\tilde{c}_D$. A characteristic $\tilde{\beta}$ where $\tilde{D}_\tau$ is insensitive to $\tilde{c}_D$ is also identified around $\tilde{\beta} \approx 0.4$ and $\tilde{D}_\tau \approx 1$. Smaller than this $\tilde{\beta}$, $\tilde{D}_\tau$ decreases as $\tilde{c}_D$ increases; larger than this $\tilde{\beta}$, $\tilde{D}_\tau$ increases as $\tilde{c}_D$ increases. These features for the drag dependence are qualitatively consistent with TY07's results, indicating that they are not due to either the choice of linear versus quadratic drag or that the drag is only present in the lower layer.

Having verified their robustness, we next try to look at how these features manifest as a function of the dimensionless parameter identified in KJ17, i.e., $\epsilon^{-1/5}\beta^{3/5}c_D^{-1}$. It is noted that since ϵ is internally solved for in this two-layer system, $\epsilon^{-1/5}\beta^{3/5}c_D^{-1}$ can no longer be regarded as an external parameter as it is in the stirred barotropic turbulence. Though, $\epsilon^{-1/5}\beta^{3/5}c_D^{-1}$ is still the only dimensionless form in all the combination of ϵ, β, and c_D in the two-layer system. In addition, in our model we have the quadratic drag with the same c_D present in the two layers, so c_D is presumably unambiguously defined (that is, we do not have to decide if the damping strength in the lower layer or the vertically average damping strength is more appropriate for scaling purposes). Following KJ17, we plot $\tilde{D}_\tau$ normalized by $\tilde{\epsilon}^{1/3}\tilde{c}_D^{-4/3}$ against $\epsilon^{-1/5}\beta^{3/5}c_D^{-1}$ in the right panel of Fig. 4.1, with ϵ computed as ϵ_p, the rate of production of eddy available potential energy (Eq. (4.3)). We present the data in a log-log plot as in

KJ17, so the $\tilde{\beta} = 0$ cases are automatically omitted. Unlike what is observed in KJ17's Fig. 3, we clearly do not see all the simulations collapse into one curve. There are instead three distinct curves. Each associates with a particular value of c_D and is displaced by roughly a constant spacing from the others, both in the x- and y-axes.

To understand this scattering of the results, we recall the physical reasoning underlying the expectation of the collapse to a single curve. In KJ17's argument, the ratio of the diffusivity at $\tilde{\beta} \neq 0$ and at $\tilde{\beta} = 0$ is characterized by the ratio of their corresponding halting wavenumbers. Suppose the halting wavenumber for the $\tilde{\beta} \neq 0$ cases is $\epsilon^{-1/5}\beta^{3/5}$. In the barotropic model with no β, the diffusivity scales as Eq. (4.1) and the halting wavenumber scales as c_D. This is why, when the former is plotted against the latter, all the data fall into a line in KJ17's Fig. 3. On the other hand, in our two-layer model with friction applying to both layers at $\tilde{\beta} = 0$, we have shown in Chapter 3 that the scaling for the diffusivity differs from Eq. (4.1). Specifically, we found that the scaling for diffusivity and mixing length can be described as (c.f. Eq. (3.16))

$$\tilde{D} \sim \tilde{c}_D^{-(4+x)/(1+x)/2} \tag{4.5}$$

and

$$\tilde{L} \sim \tilde{c}_D^{-1/(1+x)} \tag{4.6}$$

respectively, with the value $x \approx 1$ measured from the simulations (the physical meaning of x has been discussed in Section 3.3 but will be returned to later in Section 4.2.3). Therefore, the scattering is reflecting important information on how these two-layer simulations behave differently from their barotropic counterparts.

Taking account of these differences, we make two modifications to allow a more straightforward comparison to KJ17's barotropic results. First, instead of Eq. (4.1), we use the diffusivity measured at $\tilde{\beta} = 0$ (denoted as $\tilde{D}_\tau|_{\beta=0}$) to normalize $\tilde{D}_\tau$ for nonzero $\tilde{\beta}$. Second, we assume the halting wavenumber at $\tilde{\beta} = 0$ is inversely propor-

tional to the mixing length. This implies that it scales as $c_D^{1/2} k_d^{1/2}$ if we choose $x = 1$ in Eq. (4.6). For the halting wavenumber with nonzero $\tilde{\beta}$, we keep it as $\epsilon^{-1/5}\beta^{3/5}$ and with ϵ identified as ϵ_p. With these two updates, we can then define a revised dimensionless parameter

$$\mu \equiv \epsilon_p^{-1/5} \beta^{3/5} c_D^{-1/2} k_d^{-1/2} \tag{4.7}$$

that is a better analog, in its physical meaning, to the one in KJ17. It is interesting to notice that the k_d dependence is implicitly introduced by the consideration of the frictional halting wavenumber and the $\tilde{\beta} = 0$ diffusivity. In this way it reflects explicitly the proposed nature of the two-layer system that has to be characterized by this extra parameter.

The modified picture, with the ratio $\tilde{D}_\tau / \tilde{D}_\tau|_{\beta=0}$ plotted against μ, is shown in the left panel of Fig. 4.2. This way of visualization now offers a more compact view on D_τ's parameter dependence than the one plotted against $\epsilon^{-1/5}\beta^{3/5}c_D^{-1}$. For convenience in describing this result, and for potential parameterization purposes it is helpful to fit this curve with a nonlinear function,

$$\log_{10}\left(\tilde{D}_\tau / \tilde{D}_\tau|_{\beta=0}\right) = f(\mu) = \frac{A}{1 + e^{-B(\log_{10}\mu - C)}}, \tag{4.8}$$

with the constants $A = -6$, $B = 2.4$, $C = 1.2$ obtained from the least-squared fit (indicated as the gray line in Fig. 4.2).

We note that since by definition μ is a function of ϵ_p (Eq. (4.7)), and ϵ_p is related to D_τ via Eq. (4.3), Eq. (4.8) is in fact an implicit equation for D_τ. Given β and c_D, we have to solve these equations iteratively to get the predicted D_τ. With the empirical fit $x = 1$ in Eq. (4.5), or $\tilde{D}_\tau|_{\beta=0} = 0.25\tilde{c}_D^{-5/4}$, the predictions obtained accordingly are shown in Fig. 4.2's right panel (as a function of β and c_D). As the errors are amplified when these different constraints couple together, a larger discrepancy from the simulations is seen. Yet, the predictions do capture the basic structure of the

parameter dependence, especially the overall nonmonotonic c_D dependence and the significant sensitivity to β even when β is close to zero. It therefore give us some confidence that understanding D_τ from the perspective of μ is worth a closer look.

However, it is important to note that we have chosen the functional form in Eq. (4.8) simply because of its good fit to the data, but not because of some thorough theoretical consideration. In fact, we can easily point out an issue with this functional form. It is recognized that this functional form is a logistic function, so it requires $\tilde{D}_\tau/\tilde{D}_\tau|_{\beta=0}$ approaches to 10^A when $\mu \to \infty$. For finite c_D and β, $\mu \to \infty$ occurs only when $\epsilon_p \sim D_\tau \to 0$ because $\tilde{\beta} \to 1$ and the flow becomes stable. Eq. (4.8)'s prediction thus contradicts the fact that $\tilde{D}_\tau$ actually approaches to zero at this limit. Therefore, Eq. (4.8) should be regarded as an empirical fit and is not directly helpful for understanding the underlying dynamics.

To do better than the empirical fit, the natural next step is then to provide a physical explanation for the shape of this curve from some theories. At zeroth order, this curve looks qualitatively similar to the one shown in KJ17. By construction, at the limit of $\mu \to 0$, the ratio of $\tilde{D}_\tau$ and $\tilde{D}_\tau|_{\beta=0}$ approaches to one. As μ increases, this ratio remains relatively constant until $\mu \approx 1$, that is, the halting wavenumber at $\tilde{\beta} = 0$ which is set by friction halting wavenumber becoming comparable to the halting wavenumber set by the β effect. This indicates that there is a friction dominated regime where diffusivity is mostly independent of β. The same is shown in KJ17. When μ continues to increase beyond one, the β effect begins to play a role to suppress the mixing and gradually reduce $\tilde{D}_\tau$ from $\tilde{D}_\tau|_{\beta=0}$. This transition regime also appears in the barotropic results of KJ17.

When μ becomes even larger, the diffusivity ratio looks like it is approaching to a power law scaling in terms of μ. In KJ17's barotropic results, the exponent of the power law is $-3/4$. Some algebraic manipulation shows that this is consistent with $D \sim \epsilon^{3/5}\beta^{-4/5}$, i.e., Eq. (4.2). The emergence of Eq. (4.2) is the indication of the

presence of a β dominated regime, where D becomes completely independent of c_D. To achieve the same independence on drag in our two-layer model, we expect that the relevant limit to be observed is $\mu^{-5/2}$ if we approximate $\tilde{D}|_{\beta=0} \sim \tilde{c}_D^{-5/4}$ (i.e., using the approximation $x = 1$ in Eq. (4.5) once again). However, the expected $\mu^{-5/2}$ scaling is not observed in our results. Recall the nonlinear functional form that we have used for the empirical fit earlier. The coefficient $AB/4$ represents the maximum slope of this function and its value is very close to $-7/2$ for the empirical fit. This indicates the strongest μ dependence of $\tilde{D}_\tau/\tilde{D}_\tau|_{\beta=0}$ is close to $\mu^{-7/2}$ and clearly stronger than $\mu^{-5/2}$.

To understand the physical significance of this difference between the two-layer and the barotropic results, in the rest of this section, we perform a more detailed investigation on the determination of the shape of the curve. We will largely follow KJ17's approach so that we can continue comparing our results with theirs in a clean manner.

4.2.2 The propagation-suppression effect

KJ17 proposed a theory for the diffusion of a passive tracer in their barotropic model by thinking of this diffusivity, or eddy flux, as an integral over the total horizontal wavenumber k of a diffusivity spectrum. Inspired by Ferrari and Nikurashin (2010) and assuming that nonlinear eddy-eddy interaction in the barotropic PV equation can be parameterized as a linear damping component plus a stochastic white noise, KJ17 derived an equation for the diffusivity spectrum that depends on the barotropic eddy kinetic energy spectrum (c.f. their Eq. (35)). Their proposal for the diffusivity spectrum can be expressed as

$$D_{sml}(k) = \left(1 + \frac{c_2\beta^2}{2c_1^2 V_\psi^2(k)k^5}\right)^{-1} D_{ml}(k), \tag{4.9}$$

where the constants c_1 and c_2 are underdetermined, $V_\psi^2(k)$ is the spectrum of the barotropic meridional velocity variance, and

$$D_{ml}(k) = c_1^{-1} V_\psi^2(k)^{1/2} k^{-3/2} \tag{4.10}$$

is the diffusivity obtained from a traditional mixing length theory, assuming the diffusivity is determined solely by the local wavenumber and the characteristic meridional velocity at that wavenumber, $(V_\psi^2(k)k)^{1/2} \equiv \mathcal{V}(k)$. The full diffusivity, $D_{sml}(k)$, is suppressed below this mixing length expression by an extra factor that accounts for the decrease in eddy correlation time due to the zonal propagation of the eddies. Specifically, this factor is the inverse of $(1 + (c_2/(2c_1^2))(c_\beta(k)/\mathcal{V}(k))^2)$, where $c_\beta(k) = \beta k^{-2}$ is the Rossby wave's phase speed. This phase speed is larger for smaller k, so $D_{sml}(k)$ is reduced more from $D_{ml}(k)$. When $\tilde{\beta} = 0$, $D_{sml}(k)$ is simply equal to $D_{ml}(k)$.

Assuming that two-layer baroclinic streamfunction acts very much like a passive tracer in the barotropic model, this then allow us to compute $D_\tau(k)$ from the simulated $V_\psi^2(k)$ and integrate over all the wavenumbers to get a prediction for D_τ. In Fig. 4.3, we plot the predictions based on the spectral integral of $D_{sml}(k)$ and $D_{ml}(k)$ (with $c_1 = \sqrt{2}$ and $c_2/c_1^2 = 1$ chosen to obtain a reasonable fit) on top of the simulated D_τ. (It is emphasized again that the simulated $V_\psi^2(k)$ spectra are used as input here.) The data are present in the same way as Fig. 4.2. Focusing first on the prediction by traditional mixing length theory, i.e., $\tilde{D}_{ml}$ (red), we see that $\tilde{D}_{ml}$ decreases with $\tilde{\beta}$ for all $\tilde{c}_D$. In the limit of $\tilde{\beta} \to 1$, $\tilde{D}_{ml}$ also approaches to a single value (close to one) and thus becomes independent of $\tilde{c}_D$. When recast as a function of μ, it implies $\tilde{D}_{ml}/\tilde{D}_{ml}|_{\beta=0}$ would scale as $\mu^{-5/2}$. This $\tilde{c}_D$ independence is what we would have expected by simply arguing that friction is no longer relevant when β effect is sufficiently large, that is, as for the barotropic turbulence reported in KJ17. Its emergence is not self-evident here, but we will revisit it in the next subsection.

More importantly, the prediction by $\tilde{D}_{ml}$ is seen to systematically overestimate the simulated $\tilde{D}_\tau$ since it ignores the suppression effect due to the eddy propagation. Taking this effect into account, $\tilde{D}_{sml}$ (blue) gives a better fit to the simulated $\tilde{D}_\tau$. Some deviations are still observed: $\tilde{D}_{sml}$ tends to overestimate $\tilde{D}_\tau$ at $\tilde{\beta} = 0$ and underestimate the ratio $\tilde{D}_\tau/\tilde{D}_\tau|_{\beta=0}$ when $\mu \to 0$. Despite that, this prediction captures the overall complicated $\tilde{D}_\tau$ dependence on $\tilde{\beta}$, $\tilde{c}_D$, and μ. It is able to predict that $\tilde{D}_\tau$ can either increase or decrease with $\tilde{c}_D$ depending on the value of $\tilde{\beta}$. It also predicts the correct power law scaling for $\tilde{D}_\tau/\tilde{D}_\tau|_{\beta=0}$ in the limit of large μ.

The comparison between the diffusivity spectra, $D_\tau(k)$ and $D_{sml}(k)$, reveals more details of the story. These spectra are shown in the left column of Fig. 4.4. Each panel contains a series of simulations using the same $\tilde{c}_D$ but varying $\tilde{\beta}$. The spectra with the largest amplitude in each panel then correspond to the $\tilde{\beta} = 0$ cases. In these $\tilde{\beta} = 0$ cases, it is apparent that $D_{sml}(k)$ (which reduces to $D_{ml}(k)$ in this limit) and mixing length theory overemphasizes the contribution to the heat transport by the eddies at the smallest wavenumbers. Except for this clear discrepancy, $D_{sml}(k)$ does track the variation of $D_\tau(k)$ quite well in at least two aspects: it successfully predicts not only the magnitude but also the shape of the spectrum. We note that, since we did not vigorously check for every combination of c_1 and c_2, it could be possible to improve these predictions by selecting different c_1 and c_2. However, given that the physical basis for these constants are unclear, we think the current level of accuracy is enough for the purpose here to discuss the D_τ's qualitative parameter dependence and decide not to tune c_1 and c_2 to introduce additional uncertainties.

To briefly summarize, the analyses in this subsection confirms that, as far as it is D_τ that is concerned, the barotropic dynamics in this two-layer model can be well approximated by KJ17's linear stochastic model and the baroclinic streamfunction can be well approximated as a passive tracer, given the simulated spectrum of the meridional velocity, $V_\psi^2(k)$. An interesting finding is that, without the eddy

propagation-suppression effect, the diffusivity's behavior predicted by D_{ml} actually aligns better with the expectation from the barotropic scaling where it should become independent to c_D as β is sufficiently large. In fact, we observe that D_{ml} converges to Uk_d^{-1}, i.e., Stone (1972)'s scaling, in the limit of $\tilde{\beta} \to 1$, due to that both the energy containing velocity and length scales approaching to the scales of linear unstable mode without much inverse cascade. With the eddy propagation-suppression effect, the diffusivity's behavior predicted by D_{sml} is the one that correctly describes the simulated counterintuitive friction dependence.

4.2.3 The spectrally nonlocal barotropic energy input effect

Now that the prediction for D_τ based on D_{sml} from the simulated $V_\psi^2(k)$ has been shown to perform reasonably well, we would like to further look into the potential to predict D_τ from the kinetic energy spectrum described in Chapter 3 (i.e., Eq. (3.12)),

$$V_\psi^2(k) \sim \epsilon_{\psi 0}^{2x/3} k_d^{2x/3} k^{-(5+2x)/3}, \tag{4.11}$$

where $\epsilon_{\psi 0}$ is the overall magnitude of barotropic energy cascade flux (ϵ_ψ) and x is the parameter introduced earlier in Section 3.3 and fit to the $\beta = 0$ results of that chapter. When $x = 0$, this states that eddy kinetic energy can be described by Kolmogorov's inertial range where ϵ_ψ is invariant with k. When $x > 0$, this is intended to measure the extra wavenumber dependence in $\epsilon_\psi = \epsilon_{\psi 0}(k/k_d)^{-x}$ arising from the spectrally nonlocal energy transfer into the barotropic mode. It is the essential difference between the two-layer baroclinic and barotropic turbulence at the $\tilde{\beta} = 0$ limit that we have identified in Chapter 3, and our goal here is to investigate whether and how it would affect the scaling of D_τ with nonzero $\tilde{\beta}$.

The simulated $V_\psi^2(k)$ are shown in the right column of Fig. 4.4. The cases at $\tilde{\beta} = 0$ limit all agree reasonably to the spectrum slope $k^{-(5+2x)/3} = k^{-7/3}$ estimated with

$x = 1$. It is important to note that since we introduce x as a heuristic modification on Kolmogorov's theory, there is no prior knowledge on whether and how x would vary with $\tilde{\beta}$. Looking at the spectra for the nonzero $\tilde{\beta}$ cases, it is suggested that $x = 1$ continues to give a fair description for these spectra within the wavenumber range of inverse cascade (starting from $k_d = 50$ shown in Fig. 4.4). Although without a firm justification, we keep the assumption $x = 1$ for all the cases.

An extra complexity in using Eq. (4.11) to replace $V_\psi^2(k)$ in Eqs. (4.9) and (4.10) is the determination of $\epsilon_{\psi 0}$. Unlike the stirred barotropic models where the barotropic energy cascade flux (ϵ_ψ) is prescribed, the self-stirred two-layer models have ϵ_ψ solved internally so that $\epsilon_{\psi 0}$ varies among the simulations. By assuming $\epsilon_{\psi 0} \sim \epsilon_p$ and rewrite Eq. (4.11) with $x = 1$ as

$$V_\psi^2(k) = c_\psi \epsilon_p^{2/3} k_d^{2/3} k^{-7/3}, \tag{4.12}$$

we find that, with the simulated ϵ_p, choosing the constant $c_\psi = 0.8$ would do a decent job in approximating the simulated spectra within the range of wavenumbers from k_d up to the halting wavenumber, estimated visually as the energy containing wavenumber. Larger than k_d, we expect Eq. (4.12) to overpredict $V_\psi^2(k)$ as the spectrum in this part is controlled by the downscale energy cascade instead. This particular discrepancy is not significant, however, since $V_\psi^2(k)$ at these wavenumbers, even being overestimated, is already quite low.

A more serious potential problem with Eq. (4.12) is from the overestimation of $V_\psi^2(k)$ where k is smaller than the halting wavenumber. Beyond this wavenumber, the eddies are not participating much in heat transport. To obtain D_τ, it is necessary that we leave out these small wavenumbers when integrating over the spectrum, and to do so, we have to identify the halting wavenumber in advance. As shown in Fig. 4.4, this wavenumber clearly depends on $\tilde{c}_D$ and $\tilde{\beta}$. Following KJ17, we simplify this step by integrating to the halting wavenumber of the corresponding $\tilde{\beta} = 0$ case, assuming that, even if we overestimate $V_\psi^2(k)$ at the wavenumbers in between, the

suppression due to eddy propagation would substantially reduce its contribution to the final estimate of D_τ. Together with Eqs. (4.9), (4.10), and (4.12), we can write a prediction for D_τ as

$$D_p = \int_{k_0}^{\infty} \frac{c_\psi^{1/2} \epsilon_p^{1/3} k_d^{1/3} k^{-8/3}}{c_1 (1 + \frac{c_2 \beta^2}{2 c_1^2 c_\psi \epsilon_p^{2/3} k_d^{2/3} k^{8/3}})} dk, \tag{4.13}$$

where k_0 is the halting wavenumber corresponding to the $\tilde{\beta} = 0$ case for a given $\tilde{c}_D$. To express Eq. (4.13) as a function of μ, we define $\kappa \equiv k c_D^{-1/2} k_d^{-1/2}$ for convenience. Additionally, with the help of Eq. (4.3) to relate ϵ_p in the numerator back to D_τ and the definition of μ to eliminate ϵ_p in the denominator, we get

$$\tilde{D}_p = \tilde{c}_D^{-5/4} \left(\frac{c_\psi^{1/2}}{c_1} \int_{c_0}^{\infty} \frac{d\kappa}{\kappa^{8/3} + \frac{c_2}{2 c_1^2 c_\psi} \mu^{10/3} \tilde{c}_D^{1/3}} \right)^{3/2}, \tag{4.14}$$

or equivalently,

$$\tilde{D}_p \left(\tilde{D}_p |_{\beta=0} \right)^{-1} = \left(\frac{5 c_0^{5/3}}{3} \int_{c_0}^{\infty} \frac{d\kappa}{\kappa^{8/3} + \frac{c_2}{2 c_1^2 c_\psi} \mu^{10/3} \tilde{c}_D^{1/3}} \right)^{3/2}, \tag{4.15}$$

where $c_0 = \tilde{k}_0 \tilde{c}_D^{-1/2} \tilde{k}_d^{-1/2}$ is the dimensionless halting wavenumber.

Ideally, if the $\tilde{c}_D$ dependence of $\tilde{k}_0$ is well captured by $\tilde{c}_D^{-1/2}$, c_0 would be a constant as in KJ17. Assuming the energies at the wavenumbers smaller than $\tilde{k}_0$ are negligible, we have first tried to estimate $\tilde{k}_0$ by approximating the total energy level V_ψ^2 (i.e., as defined in Table 4.1) as the integration of Eq. (4.12) from $\tilde{k}_0$ to ∞ to get

$$\tilde{k}_0 = \left(\frac{3 c_\psi}{4 V_\psi^2} \right)^{3/4} \epsilon_p^{1/2} k_d^{1/2}.$$

With the simulated V_ψ and ϵ_p at $\tilde{\beta} = 0$, this gives a $\tilde{k}_0$ estimate that corresponds well with the observed peak for each $\tilde{c}_D$ in Fig. 4.4. Based on it, we can infer c_0 is

in the range 1.5 to 1.9, which is encouragingly of the order of unity. In practice, we find that the exact diffusivity prediction is very sensitive to the choice of c_0. While it is also affected by the choices of c_1, c_2, and c_ψ, we generally need slightly different c_0 values for the three sets of $\tilde{c}_D$ simulations to ensure that Eqs. (4.14) and (4.15) fit to the simulations. Specifically, we find that the best fit of c_0 falls in the range between 0.5 and 1 (rather than 1.5 to 1.9 estimated from $\tilde{k}_0$ above) and c_0 has to be larger for larger $\tilde{c}_D$.

In fact, an important implication one immediately gets from starring at Eq. (4.15) is that, if c_0 is independent of $\tilde{c}_D$, $\tilde{D}_\tau/\tilde{D}_\tau|_{\beta=0}$ shall be a function of $\mu^{10/3}\tilde{c}_D^{1/3}$ rather than simply a function of μ. Accordingly, we then need three different curves to describe the different μ dependence for three set of simulations with different $\tilde{c}_D$. To collapse them to a single curve that better agrees with the simulations, we then unavoidably have to bring in an additional $\tilde{c}_D$ dependence of c_0. This uncertainty in c_0 is an awkward complication, and it is very likely reflecting the errors we have introduced so far by making a series of approximations. Since the physical justifications for some of these approximations are also not well-established, it is difficult to pin down which of them is most severely violated. therefore, in the context of this thesis we have decided to refrain from pushing Eq. (4.15) further forward and to only report on our results up to this point concerning this diffusivity spectrum and the propagation-suppression approach.

Despite these limitations, we notice that Eq. (4.15) remains helpful for studying some aspects of the diffusivity's qualitative parameter dependence. When we rewrite Eq. (4.15) in terms of $\kappa' = \mu\kappa$,

$$\tilde{D}_p \left(\tilde{D}_p|_{\beta=0} \right)^{-1} = \mu^{-5/2} \left(\frac{5c_0^{5/3}}{3} \int_{c_0/\mu}^{\infty} \frac{d\kappa'}{\kappa'^{8/3} + \frac{c_2}{2c_1^2 c_\psi}\mu^{2/3}\tilde{c}_D^{1/3}} \right)^{3/2}, \tag{4.16}$$

several interesting observations can be made. First, if we ignore the second term in the denominator in the integral, that is, the term associated with the propagation-suppression effect, we see that Eq. (4.16) suggests a power law scaling $\mu^{-5/2}$ when $\mu \to \infty$. This can explain the earlier results for D_{ml} using the simulated $V_\psi^2(k)$ (Section 4.2.2). Furthermore, keeping the propagation-suppression term makes the value of the integral depends on μ as well, so the solution becomes more sensitive to μ than $\mu^{-5/2}$ when $\mu \to \infty$. This is also qualitatively consistent with the earlier results for D_{sml} using the simulated $V_\psi^2(k)$ (Section 4.2.2). Hence, we believe that Eqs. (4.13)-(4.16), based on the assumed $V_\psi^2(k)$ in Eqs. (4.11)-(4.12), do capture some of the essence of the dynamics involved. That is to say, the spectrally nonlocal barotropic energy input and the steeper barotropic energy spectrum certainly play roles in controlling the diffusivity scaling, but there may still be some effects that we have overlooked and thus a room to improve the theory.

4.3 Assessment on alternative scaling relations

4.3.1 Empirical fits

In this section, we put aside the comparison to TY07 and KJ17 and shift our focus to evaluating the two simple diffusivity scaling relations proposed by previous studies in explaining β-plane homogeneous two-layer QG simulations. As the constant factor in these scaling relations is unconstrained, an assessment of this type is usually done by comparing the scaling prediction and the simulation in a log-log plot. Our results in Section 4.2 are nonetheless mainly assessed and shown in terms of $\tilde{D}_\tau/\tilde{D}_\tau|_{\beta=0}$ as a function of μ and $\tilde{c}_D$. To allow a fair comparison to them, we first try to replot them in a log-log plot for later reference. As disclosed earlier, although the transformation into μ coordinate helps simplify the picture, we are still struggling to come up with a closed form prediction for D_τ. Therefore we set aside those unsettled theoretical

questions and take our earlier empirical fit as the baseline calculation for comparison to other scaling theories.

The upper left panel of Fig. 4.5 shows the results of simulated $\tilde{D}_\tau$ plotted against the predictions in the right panel of Fig. 4.2. Recall that this prediction is based on the nonlinear fit described by Eq. (4.8), which is an implicit equation for $\tilde{D}_\tau$, given that ϵ_p and $\tilde{D}_\tau$ are proportional to each other. The prediction is therefore obtained by solving Eq. (4.8) iteratively with other equations to eliminate ϵ_p in the predictor variables. Physically, it reconfirms that μ captures most (even though not all) the variations in $\tilde{D}_\tau/\tilde{D}_\tau|_{\beta=0}$ and represents the best prediction that we can get so far from the perspective of μ with only the knowledge of $\tilde{\beta}$ and $\tilde{c}_D$ given. While this approach does not provide us the explicit functional form for $\tilde{D}_\tau$, we emphasize that it does allow us to obtain the predicted $\tilde{D}_\tau$ without assuming that we can in priori give ourselves the simulated $\tilde{\epsilon}_p$ as a predictor variable. As we will show later on, going through this extra step to make an explicit prediction can result in noticeable differences in the fitting results (as the same issue arose concerning the analysis of Barry et al. (2002)'s theory in Chapter 2).

4.3.2 $\epsilon^{3/5}\beta^{-4/5}$ and the three diffusivities

The first scaling we would like to investigate is Eq. (4.2), i.e., $D \sim \epsilon^{3/5}\beta^{-4/5}$. As we discussed in Section 4.1, this diffusivity scaling is purely obtained by dimensional analysis assuming the only relevant parameters are ϵ and β. It thus pose a question in the two-layer turbulence context where there are three diffusivities: D_τ and the diffusivities for upper and lower layer PV fluxes, D_u and D_l, respectively. The three diffusivities are related through Eq. (4.4), and the necessity to distinguish them reflects the nature of the layer asymmetry due to β. Looking at Eq. (4.4), D_u is different from D_τ by a factor of $(1+\tilde{\beta})^{-1}$, which varies from 1 to 1/2 for $0 \leq \tilde{\beta} \leq 1$. By contrast, D_l differs from D_τ for a factor of $(1-\tilde{\beta})^{-1}$, which varies from 1 to ∞.

Hence, a significant distinction between the three diffusivities would appear at large β and between D_τ and D_l.

LH03 did find Eq. (4.2) gives a considerably better fit to D_l in their simulations with bottom linear drag (c.f. their Fig. 3). To understand whether this also applies to our simulations that have the quadratic drag appearing in both layers with the same damping strength, we have performed the same calculations. In the upper and lower right panels of Fig. 4.5, we plot the simulated D_τ and D_l against Eq. (4.2)'s prediction with $\epsilon = \epsilon_p$, respectively. Eq. (4.2) is seen to explain D_l better, especially for large β and small c_D, which is consistent with the LH03's results. The fact that this scaling fit is insensitive to the model's setup of the large-scale friction seems to affirm LH03's claim on that friction being confined in the bottom layer plays little role in the result that Eq. (4.2) is a better fit to D_l. As they argued, the distinction between upper and lower layer dynamics rather comes from the different magnitudes of mean PV gradient in the presence of β. That is, due to the smaller mean PV gradient in the lower layer waves are more likely to break and the flows are more turbulent and more plausibly approximated by a traditional turbulent diffusivity theory.

On the other hand, no matter which diffusivity is being considered, the results are not significantly better than those predicted from our empirical fit. If we take the physical picture behind the latter more seriously, we would need to exclude LH03's argument and Eq. (4.2). We will then need an alternative explanation for the seemingly good fit in Fig. 4.5. Looking at the comparison between Eq. (4.2)'s prediction and the simulated $\tilde{D}_\tau$, we see that Eq. (4.2) increasingly underestimates the sensitivity of $\tilde{D}_\tau$ when $\tilde{\beta}$ becomes larger. Particularly, at the limit of $\tilde{\beta} \to 1$, $\tilde{D}_\tau \to 0$. Yet, in the rhs of Eq. (4.2), the change of $\beta^{-4/5}$ becomes less important than the change of $\epsilon_p^{3/5}$, which is proportional $D_\tau^{3/5}$ according to Eq. (4.3) and leads to Eq. (4.2)'s increasing underestimation. Different from $\tilde{D}_\tau$, $\tilde{D}_l$ has an extra factor $(1-\tilde{\beta})^{-1}$ (i.e., Eq.(4.4)), which makes $\tilde{D}_l$ decreases less rapidly than $\tilde{D}_\tau$ when $\tilde{\beta}$ increases. That is, $\tilde{D}_l$ is less

sensitive to $\tilde{\beta}$ than $\tilde{D}_\tau$. Hence, the fact that Eq. (4.2) increasingly underestimates the sensitivity of D_τ actually allows it to better fit to the simulated weaker sensitivity of $\tilde{D}_l$ in an intermediate range of $\tilde{\beta}$. Beyond this intermediate $\tilde{\beta}$ range, the change of $(1-\tilde{\beta})^{-1}$ at large $\tilde{\beta}$ eventually overcompensates the weak sensitivity bias of Eq. (4.2) and result in Eq. (4.2) to become overestimating $\tilde{D}_\tau$'s sensitivity to $\tilde{\beta}$ instead. From this perspective, it seems the apparent agreement between the simulated $\tilde{D}_l$ and Eq. (4.2)'s prediction could likely be a coincidence. However, since we cannot fully explain D_τ's parameter dependence from μ either, it would be overstated if completely ruling out LH03's argument.

We shall also note that as $\tilde{\epsilon}_p$ is proportional to $\tilde{D}_\tau$ via Eq. (4.3), we can eliminate ϵ as a predictor variable in $D_l \sim \epsilon_p^{3/5}\beta^{-4/5}$ and rearrange to get $D_l \sim (1-\tilde{\beta})^{3/2}\beta^{-2}(Uk_d)^3$, as in LH03 (c.f. their Eq. (15)). Since Eq. (4.3) is essentially the two-layer QG version of Eq. (2.5), the spirit behind this step toward a closed form scaling expression is exactly the same as what we have done in Section 2.6. We plot this explicit prediction against the simulations in the lower left panel of Fig. 4.5, as shown in Fig. 5 of LH03. Consistent with their findings, we can see that the existing errors are substantially amplified and become more apparent from this perspective, in which one assumes that one only knows the external parameters (β, U, and k_d in this case). It is therefore a fairer comparison with the empirical fits in the upper left panel of Fig. 4.5, and it is obviously less preferable than the empirical fits.

4.3.3 Bulk mixing length theory with Rhines scale

The second scaling to be examined is derived by assuming the mixing length theory with mixing length being the Rhines scale (Rhines 1975). Rather than applying the mixing length theory to every wavenumbers (Section 4.2.2), it assumes the mixing length theory holds for the spectrally-integrated ("bulk") eddy scales. That is, D

scales as the root-mean-squared eddy velocity (V) and eddy mixing length (L),

$$D \sim VL. \tag{4.17}$$

The next step is to assume $L \sim L_R \equiv V^{1/2}\beta^{-1/2}$, a length scale proposed by Rhines (1975) as the approximation for the energy-containing scale, to get

$$D \sim V^{3/2}\beta^{-1/2}. \tag{4.18}$$

This scaling prediction has an explicit dependence on V, which must be solved for internally even in the stirred barotropic model. It is therefore not a closure in itself and could only be useful (as a predictive rather than merely diagnostic theory) if V is known by some other means. While Eq. (4.18) has implicitly or explicitly appeared as an intermediate step in the arguments of many scaling theories, to our knowledge it has rarely been tested in isolation and discussed extensively (e.g. Held and Larichev 1996; Barry et al. 2002; Jansen et al. 2015). We have already discussed Eq. (4.18) in our analysis of the idealized GCM in Chapter 2. As shown there, the Rhines scale-based diffusivity fits surprisingly well to the idealized general circulation model (GCM) simulations even though the definitions of the variables in that model may be somewhat ambiguous. This is another motivation for us to examine this diffusivity scaling relation again here, where these ambiguities are reduced.

Letting D to be D_τ, we first verify Eq. (4.17) by studying how well the bulk correlation coefficient between eddy velocity and baroclinic streamfunction, i.e., $c_\tau \equiv D_\tau(V_\psi L_\tau)^{-1}$ can be approximated as a constant. The simulated c_τ is shown in the left panel of Fig. 4.6, plotted against $\tilde{\beta}$ with different symbols denote different $\tilde{c}_D$. It is seen that c_τ is larger for larger $\tilde{\beta}$ and $\tilde{c}_D$. The range of its variation, considering the maximum and minimum in our simulations, is almost an order of magnitude. The lack of constancy of c_τ for $\tilde{\beta} = 0$ cases is discussed in Chapter 3 as a caveat of

the scaling arguments based on Eq. (4.17). It is also reported in TY07. We do not propose any simply theory for the variation of c_τ, but from the point of view of the diffusivity spectrum analyzed above, its variation with $\tilde{\beta}$ is presumably related to some average of the different effects operating at different wavenumbers. Its interpretation is therefore not straightforward.

While c_τ does depend on the parameters, its variation is generally speaking relatively smaller compared to the variations in V_ψ, which is shown in the right panel of Fig. 4.6. It is interesting to see that V_ψ has a qualitatively similar parameter dependence as D_τ. For a given $\tilde{c}_D$, V_ψ always decreases with $\tilde{\beta}$. For a given $\tilde{\beta}$, V_ψ can either increase or decrease with $\tilde{c}_D$ depending on the exact value of $\tilde{\beta}$. The value of $\tilde{\beta}$ dividing the two regimes is about 0.5 where $\tilde{V}_\tau \approx 1$. From Eq. (4.3), we can infer that ϵ_p also share the similar behavior, indicating both the baroclinic available potential energy generation and kinetic energy level can be lower when friction is weaker in a range of $\tilde{\beta}$. This picture seems to be consistent with the description of barotropic governor, which highlights the importance of barotropic shear on baroclinic instability. This would be an interesting topic for study, but for now we simply take V_ψ as given. Focusing on the scaling relation, the significance of Fig. 4.6 is that the similarity between V_ψ and D_τ does give some incentive to further check whether Eq. (4.18) with $V = V_\psi$ could indeed predict D_τ, even though we have confirmed Eq. (4.17) is hard to justify.

Fig. 4.7 shows the log-log plots of the prediction by Eq. (4.18) with $V = V_\psi$ against the three simulated diffusivities, D_τ, D_u, and D_l. We show the results for all three as there seems to be no a prior knowledge as to which one Eq. (4.18) best applies to. Generally speaking, these results look pretty much like the results of Eq. (4.2) in Fig. 4.5. Similar to Eq. (4.2), Eq. (4.18) still overestimates the sensitivity of D_τ when $\tilde{\beta}$ is large. This is then compensated by the factor of $(1-\tilde{\beta})^{-1}$ difference from D_τ for D_l in Eq. (4.4), so Eq. (4.18) fits the best to D_l. Again, some overcompensation

is observed for large $\tilde{\beta}$ and large $\tilde{c}_D$ cases. Yet, the overall performance of Eq. (4.18) is considered to be better than of Eq. (4.2). If anything, it seems more promising to pursue the study of Eq. (4.18) than Eq. (4.2). Despite only an approximation, Eq. (4.18) may have some practical values in providing a diffusivity estimate without going through the analysis from the perspective of the wavenumber spectrum (Section 4.2). We note that the recent mesoscale eddy kinetic energy budget approach of Jansen et al. (2015) to eddy closure in ocean models takes this perspective (c.f. their Fig. 6d), separating the theory for the eddy energy level from the theory for the diffusivity given this energy level. The potential and limitations of this approach are worth a better understanding.

4.4 Conclusions

Seeking a theoretical understanding of the parameter control on homogeneous quasi-geostrophic eddy diffusivity has been a long-lasting problem. The goal of this study is to connect the results and arguments in the previous two-layer studies, Thompson and Young (2007, hereafter TY07) and Lapeyre and Held (2003, hereafter LH03) in particular, to the recent advance made by Kong and Jansen (2017, hereafter KJ17) on understanding passive tracer diffusion in the barotropic externally stirred case, in the hope of shedding some lights on the overall problem. Aiming at this, we examine a set of simulations from a homogeneous two-layer quasigeostrophic model that has large-scale friction appearing in both layers. The friction is in the quadratic drag form, and its damping strength, characterized by the frictional wavenumber (c_D), is kept identical in the two layers. This unusual setup is introduced in Chapter 3 to offer a cleaner comparison between the dynamics of the turbulent flows in the self-stirred two-layer baroclinic model and stirred barotropic model. There, the c_D dependence of eddy scales and eddy fluxes in the limit of the vanishing β is studied, and a heuristic

argument is used to explain its key difference from its barotropic counterpart. Based on those findings, we extend the analyses to the cases with nonzero β and investigated the parameter dependence of eddy diffusivities on both c_D and β.

Focusing on the diffusivity for the eddy heat fluxes (D_τ), we first show that its parameter dependence in our simulations is qualitatively consistent with the one described in TY07, where their simulations are run with the conventional bottom linear drag. One important finding in both studies is that, as β becomes larger, D_τ continues to be dependent on the frictional damping strength. Furthermore, D_τ increases with stronger friction when β is beyond some value. This sensitivity to friction is conterintuitive because one would expect from what is shown in barotropic models that friction drops out of the picture when β is sufficiently large to halt the inverse energy cascade and control the eddy equilibrated scale by itself. The similarity of our simulations to TY07's results however asserts that this particular aspect of D_τ behavior is robust against the details of how friction is set up. It then provides the justification to look seriously into our simpler albeit less realistic simulations, which can be related to KJ17's barotropic results more cleanly.

Following KJ17 and making some adjustments, we showed that considering $D_\tau/D_\tau|_{\beta=0}$ as a function of c_D and $\mu = \epsilon_p^{-1/5}\beta^{3/5}c_D^{-1/2}k_d^{-1/2}$ brings a more compact and comprehensible view on D_τ's parameter dependence ($D_\tau|_{\beta=0}$ refers to the value of D_τ in the $\beta = 0$ limit). The dimensionless parameter μ is the ratio of two theoretical halting wavenumbers, i.e., $\epsilon_p^{-1/5}\beta^{3/5}$ due to β effect and $c_D^{1/2}k_d^{1/2}$ due to friction. The latter is derived from the heuristic eddy scaling presented in Chapter 3, which is proposed to take account of the barotropic eddy kinetic energy spectrum's deviation from Kolmogorov's theory due to the spectrally nonlocal barotropic energy input. With this modification, μ is chosen as analogous to the one used in KJ17 to develop a generalized theory for passive tracer diffusivity in barotropic turbulence.

Their theory assumes that, at every wavenumber, the barotropic potential vorticity (PV) equation can be approximated as a stochastic linearly damped process, and the transport of passive tracers in this flow is determined by the local eddy turnover time as well as the eddy decorrelation time. The eddy decorrelation time is effectively reduced as eddies propagate zonally in the presence of mean barotropic PV gradient, i.e., β, leading to a suppression on the meridional mixing. By considering these approximations, their theory links the diffusivity spectrum to the barotropic eddy kinetic energy spectrum. When we give ourselves the latter from the simulations, we find that their theory can reasonably predict the simulated D_τ for both its spectrum and the spectrally-integrated value. While some underdetermined constants are introduced in the derivation that require an arbitrary fitting and the theory tends to overestimate at $\beta = 0$, it is particularly useful for explaining the puzzling parameter dependence of D_τ. When strategically leaving out the term associated with the eddy propagation-suppression effect, the theory suggests that D_τ would instead become independent of c_D and converges to Stone (1972)'s diffusivity as β approaches to its stability threshold. It therefore helps elucidate that the suppression on the mixing due to eddy propagation plays a crucial role in leading to D_τ's counterintuitive behavior.

Encouraged by these results, we apply the knowledge obtained in Chapter 3 to further make an assumption concerning the barotropic eddy kinetic energy spectrum and repeated the calculations. Specifically, we find that the barotropic eddy kinetic energy spectrum in the nonzero β simulations share the same spectral slope as in the $\beta = 0$ simulations examined in Chapter 3. They are all steeper than predicted by Kolmogorov's inertial range theory due to the spectrally nonlocal energy input from the baroclinic mode. This is self-consistent with the way we chose to define μ and allows us to explicitly write down an analytic expression for D_τ (Eqs. (4.14)-(4.16)). The expression reveals the nature of how D_τ is determined by both μ and $c_D k_d^{-1}$ (nondimensionalized c_D). Particularly, it explains the μ dependence that we

have seen in the predictions using the simulated barotropic kinetic energy spectrum, reconfirming the importance of the spectrum steepness due to its nonlocal energy source.

In spite of the physical insights it provides, we have found the value of D_τ predicted by the expression is in practice sensitive to the underdetermined constants that have to be empirically constrained. Especially, a complication is related to determining the minimum wavenumber of the spectral integration. This minimum should be a constant in theory, but we find it hard not to specify different values for different c_D to fit the simulations. Since the theory has buried a substantial numbers of approximations and among them a major one is the heuristic argument made in Chapter 3 for the halting wavenumber and the spectral shape, it is difficult for us to pin down the primary source of uncertainty and to make a physically-justified improvement on this foundation. Therefore, we need to leave this promising approach in this incomplete state.

On the other hand, setting aside this theoretical approach, we have seen that the variations of the simulated D_τ normalized by $D_\tau|_{\beta=0}$ can be well explained by μ alone. This motivates an empirical fit for the functional form, $\log_{10}(D_\tau/D_\tau|_{\beta=0}) = f(\mu)$. The empirical approach indeed does a fair job in tracking D_τ's variations when presented in log-log plots, which are typically used to assess their overall fit of a scaling prediction to the simulations. Taking this empirical result as a baseline, we also study the performance of two scaling predictions proposed in previous studies. One is based on energy generation rate ϵ_p, $D \sim \epsilon_p^{3/5}\beta^{-4/5}$ (Eq. (4.2)) and the other is based on the overall barotropic eddy energy level V_ψ, $D \sim V_\psi^{3/2}\beta^{-1/2}$ (Eq. (4.18)). Overall, these predictions are not as good as the empirical result and tend to underestimate D_τ's sensitivity when β is large. These errors are however compensated and reduced when fitting to lower layer PV flux diffusivity (D_l) which varies less with β than D_τ. From this viewpoint, LH03's claim that $D \sim \epsilon_p^{3/5}\beta^{-4/5}$ can explain D_l may likely be

a coincidence. In any case, we have found $D \sim V_\psi^{3/2}\beta^{-1/2}$ outperforms $D \sim \epsilon_p^{3/5}\beta^{-4/5}$ in general, so understanding the underlying physics of $D \sim V_\psi^{3/2}\beta^{-1/2}$ may be more promising.

Putting together, our simulations and analyses help reconcile the current knowledge of the passive tracer diffusivity in the stirred barotropic model and of the heat flux diffusivity in the self-stirred two-layer model. Overall, we conclude that the two diffusivities are controlled by similar dynamics once the characteristics of the barotropic mode is correctly described, so understanding the former remains especially relevant to and beneficial for understanding the latter. This perspective agrees qualitatively with the classic picture conceptualized in Rhines and Salmon's work and formulated more formally as a scaling theory by Held and Larichev (1996). In this sense, our conclusions are not completely aligned with TY07's stand on the problem, where they dismissed this classic framework and argued the two-layer turbulence and barotropic turbulence are too different regarding their diffusivities, requiring that a new framework should be found to study the two-layer diffusivity.

We shall emphasize that TY07 were led to their stronger conclusions not only by the counterintuitive parameter dependence of diffusivity but also other significant differences identified in their two-layer simulations that distinguish from what would have been expected based on the barotropic turbulence. For instance, they discovered that the baroclinic dynamics is not only a passive provider of the energy at the deformation radius but is also actively involved in the maintenance of the coherent structures, which they argued to be closely related to heat fluxes and are equivalent barotropic in nature. For nonzero β simulations, these are the zonal jets maintained predominately by upper layer eddy momentum flux convergence. The same upper layer dominance is observed in our simulations with friction in both layers, as well as with friction only in the top or bottom layer. While the emergent evidence that the dominance tends to always be in the layer of larger PV gradient requires clarification,

it is not immediately obvious to us how this unexplained structure would refute the calculations and the theory presented in this study. Following KJ17, our concern remains to confined in the barotropic dynamics, and it is noted that the projection of the jets themselves on the vertical modes is still primarily barotropic as in TY07.

We therefore view our study as rebuilding the connection back to the classic picture, despite that it is originally inspired in a large part by TY07's work and it still leaves many questions unanswered. We believe this study, taking the advantage of the recently gained understanding of mixing suppression due to eddy zonal phase propagation (e.g. KJ17), could serve as a platform to further discuss the important details in the two-layer dynamics that are distinct from the barotropic counterpart. This includes but not limited to the nonlocal barotropic energy input, the layer asymmetry due to friction and β, and the coherent structure issues identified by TY07. For example, as in Chapter 3, we have also found that the asymmetric drag results closely resemble the symmetric drag results presented here for the smaller values of β and $c_D k_d^{-1}$. We thus expect our analysis could be largely carried over to the bottom drag simulations in this regime, and it would then be interesting to study how the bottomness of friction affects the cases with large β and strong damping. As these new complexities accumulate, it is certainly possible that we indeed end up moving farther from the classic theoretical framework focusing on energy cascades. Yet, even if that is the final case, we believe the results here are still informative on how to approach this more complete theory.

Variable
$D_\tau = \langle \tau \partial_x \psi \rangle$
$V_\psi = \sqrt{\langle \partial_x \psi^2 \rangle}$
$L_\tau = \sqrt{\langle \tau^2 \rangle} U^{-1}$

Table 4.1: A list of the examined variables and their diagnostic definitions. ψ and τ denotes for the barotropic and baroclinic streamfunction, respectively. The angle brackets refer to the domain averaged.

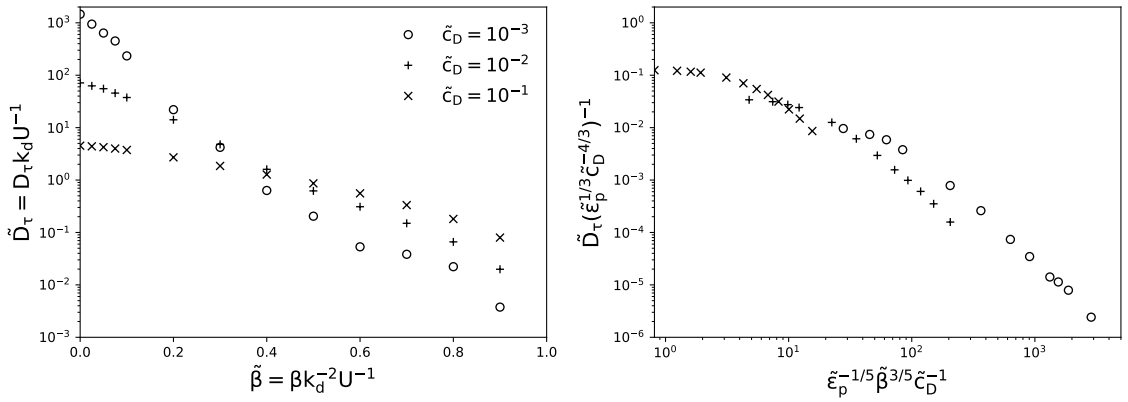

Figure 4.1: The parameter dependence of the simulated heat flux diffusivity: (left) $\tilde{D}_\tau = D_\tau k_d U^{-1}$ plotted against $\tilde{\beta} = \beta k_d^2 U^{-1}$ and (right) $\tilde{D}_\tau$ normalized by $\tilde{D}_\tau|_{\beta=0}$ plotted against the nondimensional parameter $\tilde{\epsilon}_p^{-1/5}\tilde{\beta}^{3/5}\tilde{c}_D^{-1}$. The simulations with different $\tilde{c}_D = c_D k_d^{-1}$ are indicated by different symbols. The tildes imply the nondimensionalization by k_d and U.

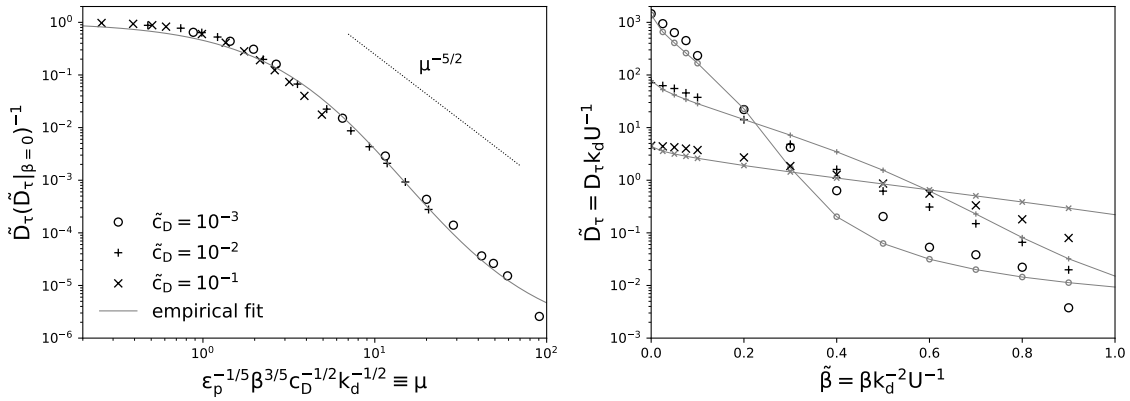

Figure 4.2: The parameter dependence of the simulated heat flux diffusivity and its empirical fit: (left) $\tilde{D}_\tau$ normalized by $\tilde{D}_\tau|_{\beta=0}$ plotted against the revised nondimensional parameter $\mu = \epsilon_p^{-1/5}\beta^{3/5}c_D^{-1/2}k_d^{-1/2}$ and (right) $\tilde{D}_\tau$ plotted against $\tilde{\beta}$. The doted line in the left panel indicates the power law scaling $\mu^{-5/2}$. The empirical fit is shown as the gray line, and its functional form $f(\mu)$ is described by Eq. (4.8). See the text for the details on the inversion of Eq. (4.8) in obtaining estimates of $\tilde{D}_\tau$ in the right panel.

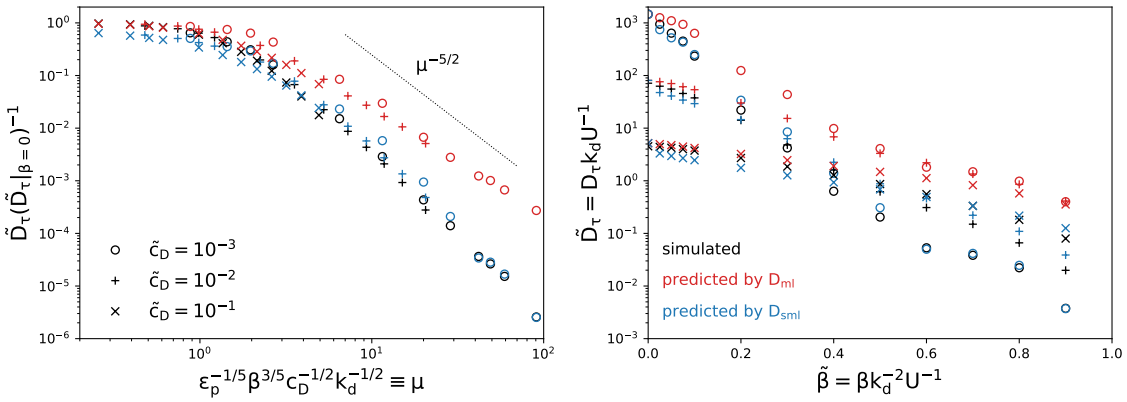

Figure 4.3: As in Fig. 4.2, but with the comparison to the two predictions based on the simulated eddy kinetic energy spectrum: the simulation (black), the prediction by the mixing length theory (D_{ml} as the integral of Eq. (4.10); red), and the prediction by the suppressed mixing length theory (D_{sml} as the integral of Eq. (4.9); blue).

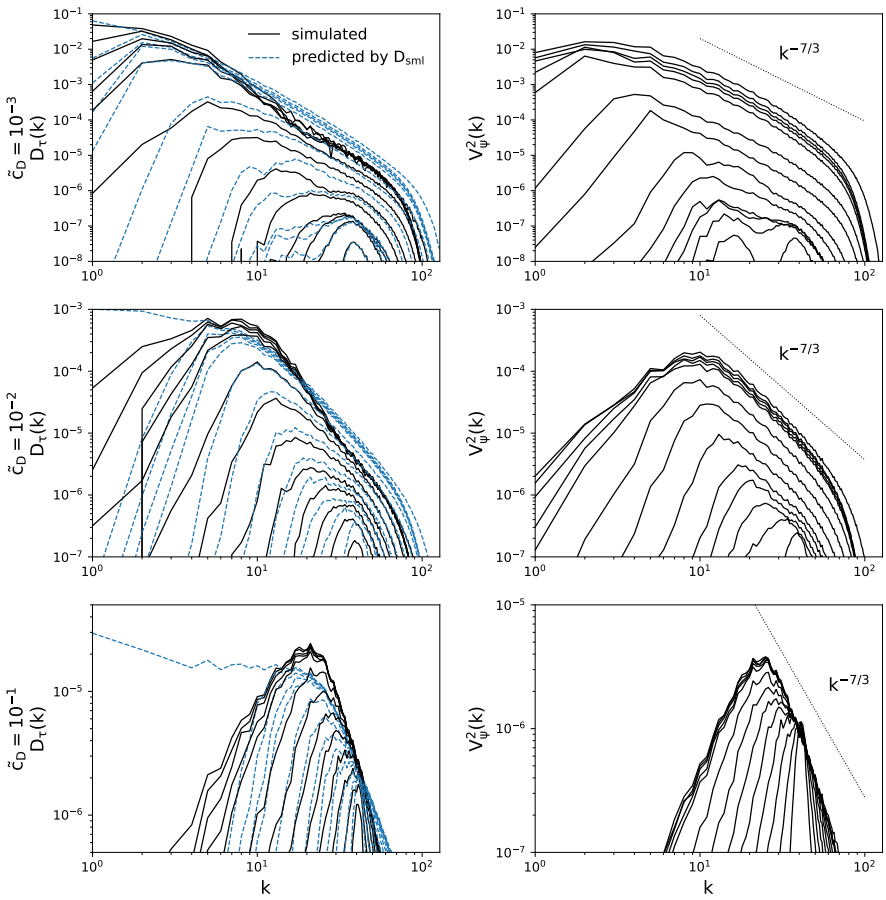

Figure 4.4: The eddy spectra as a function of the total wavenumber (k): heat flux diffusivity ($D_\tau(k)$; left) and barotropic eddy kinetic energy ($V_\psi^2(k)$; right). Each panel shows a set of simulations with a fixed $\tilde{c}_D$ but varying $\tilde{\beta}$. On the left, the simulated $D_\tau(k)$ (black solid) is plotted along with the prediction by the suppressed mixing length theory ($D_{sml}(k)$; blue dashed). On the right, the simulated $V_\psi^2(k)$ is plotted along with the predicted spectral slope $k^{-7/3}$ (dashed).

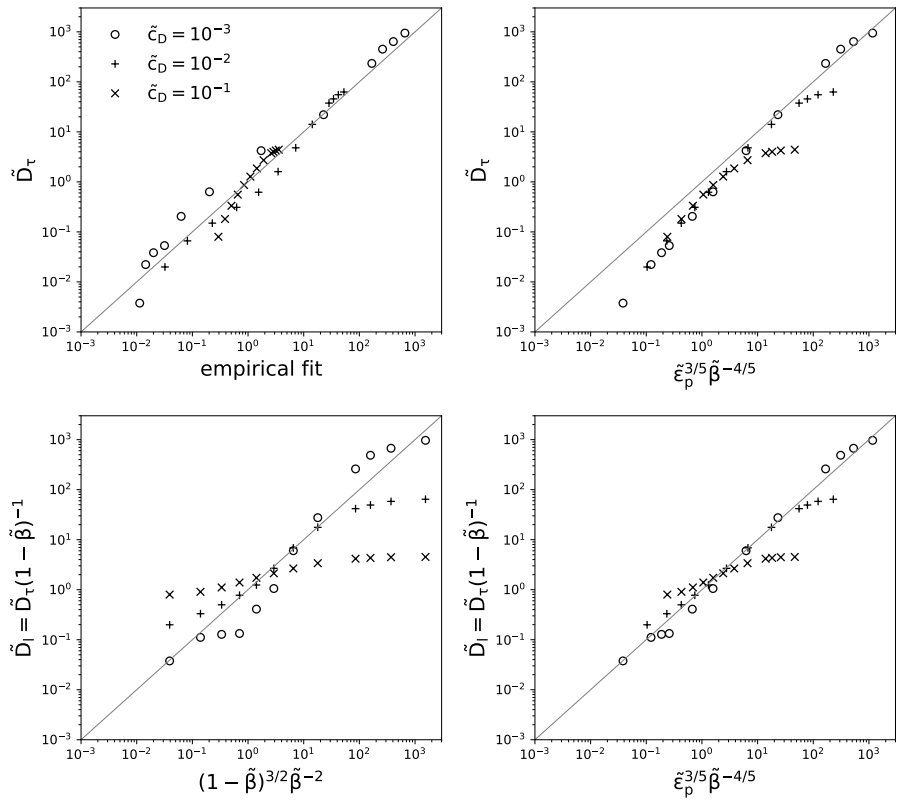

Figure 4.5: The log-log plots of the predicted versus simulated eddy diffusivities: (upper left) the empirical fits obtained in Fig. 4.2 and the simulated heat flux diffusivity ($\tilde{D}_\tau$), (upper right) $\tilde{\epsilon}_p^{3/5}\tilde{\beta}^{-4/5}$ versus simulated heat flux diffusivity ($\tilde{D}_\tau$), (lower left) $\tilde{\epsilon}_p^{3/5}\tilde{\beta}^{-4/5}$ versus simulated lower layer PV flux diffusivity ($\tilde{D}_l$), and (lower right) $(1-\tilde{\beta})^{3/2}\tilde{\beta}^{-2}$ versus simulated lower layer PV flux diffusivity ($\tilde{D}_l$).

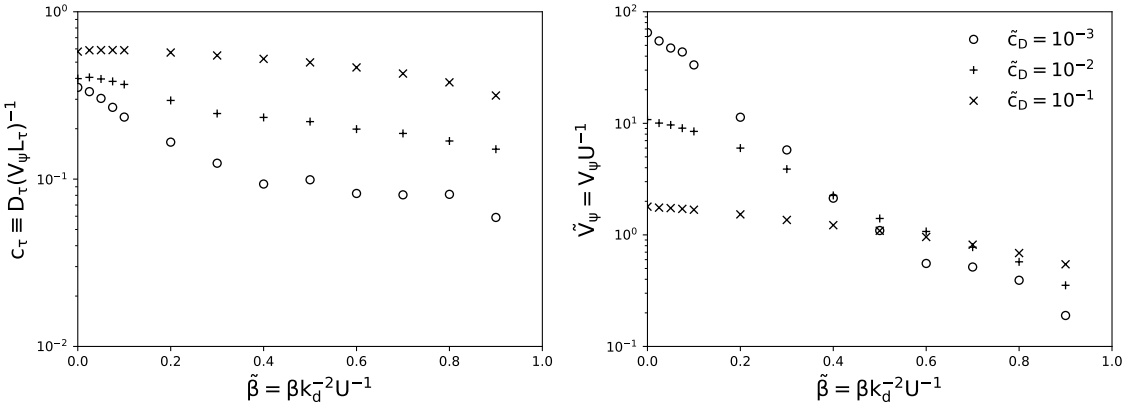

Figure 4.6: The parameter dependence of the simulated bulk correlation coefficient and eddy velocity: the correlation coefficient between barotropic meridional velocity and baroclinic streamfunction ($c_\tau = D_\tau(V_\psi L_\tau)^{-1}$; left) and barotropic meridional velocity ($\tilde{V}_\psi$; right) plotted against $\tilde{\beta} = \beta k_d^2 U^{-1}$.

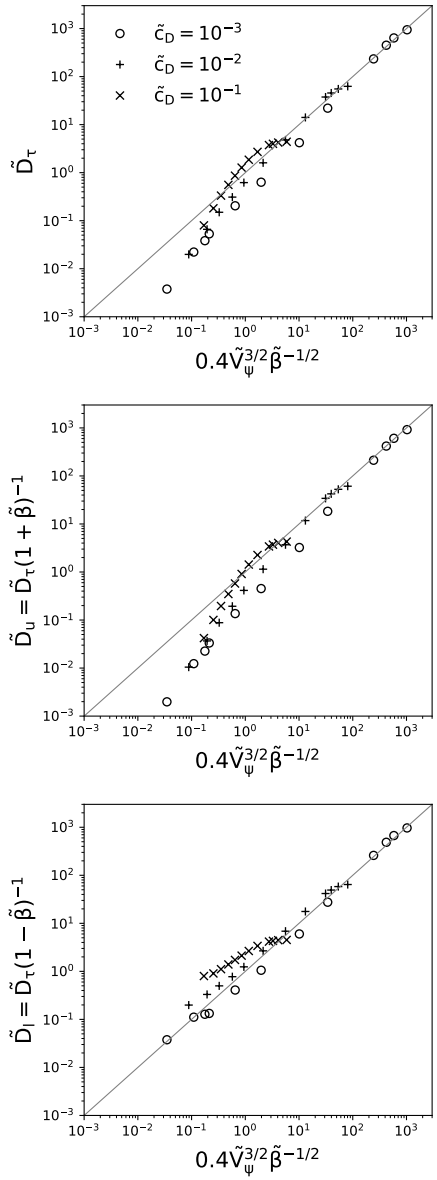

Figure 4.7: The scaling prediction by $0.4\tilde{V}_\psi^{3/2}\tilde{\beta}^{-1/2}$ versus simulated diffusivities: heat flux diffusivity ($\tilde{D}_\tau$; top), upper layer PV flux diffusivity ($\tilde{D}_u$; middle), and lower layer PV flux diffusivity ($\tilde{D}_l$; bottom). The constant 0.4 is arbitrarily chosen to shift all the data closer to the diagonal line.

Chapter 5

Maximum entropy production and the climates of the idealized GCM

We have devoted the previous chapters to understanding the dynamics behind how eddies equilibrate with mean flows and how they together set the equilibrated climate's thermal structure. As we know more about the topic, we either encounter another long-established question or a newly-identified one which we have not yet been able to solve. This chapter discusses a potential way to overcome this challenge by phrasing the overall problem inversely. We study an approach which predicts the equilibrated thermal structure from a purely thermodynamic perspective. It assumes the fluid dynamics is determined implicitly and responds passively, arguing one should rather directs attention back to some higher-level control on the maintenance of the climate.

5.1 Introduction

While we may also be interested in the eddies themselves, a primary goal studying eddy equilibration in the extratropical troposphere is to better understand how the climate maintains its mean state (Section 1.1). A grand feature of Earth's mean

climate is that the tropics is warmer than the polar regions, so there is an overall temperature gradient between equator and poles. This meridional temperature gradient owes its existence to the meridional gradient of insolation. Yet, the atmosphere is not locally in radiative equilibrium. In fact, the midlatitude baroclinic eddies play an essential role in the heat transport that balances the local surplus or deficit of the radiative energy imbalance. This has been an important reason to research the dynamics underlying these eddies, as we have been doing in the previous chapters. In addition, the radiative fluxes can also be modified by the distribution of water vapor and clouds, which is strongly affected by the motion in the atmosphere that is fundamentally controlled by fluid dynamics. At the statistically steady state, the maintenance of meridional temperature gradient ultimately depends on the interplay between numerous physical and dynamical processes in the climate system.

Given the number of dimensions involved, understanding and simulating these processes have been challenging. This challenge sparks interest in seeking a universal principle that would allow us to predict the meridional temperature gradient without studying all of these processes explicitly. An idea of this kind is based on the work by Paltridge (1975, 1978). Studying a one-dimensional (meridional) energy balance model, he found that his model makes a good prediction for the observed Earth's climate if he assumes that the equilibrated model climate has a special thermodynamic property of minimizing the globally integrated diabatic entropy destruction, or equivalently, maximizing the globally integrated entropy production, among all the candidate climates that satisfy the constraint where globally integrated incoming shortwave radiation equals to the outgoing longwave radiation.

Paltridge's results were later taken by some as an empirical evidence to motivate a hypothesis that the climate would prefer to equilibrate at the statistically steady state of maximum entropy production (MEP) rather than as just a coincidence. It has even been argued to be applicable to any nonequilibrium thermodynamic system (e.g.

Martyushev and Seleznev 2006, 2014; Dewar and Maritan 2014), but we here restrict our discussion to its applications to Earth and planetary atmospheres so as not to get mixed up with other problems. This hypothesis, referred as the MEP hypothesis, has attracted a series of studies which together give a very mixed interpretation of its validity (e.g. Ozawa et al. 2003; Goody 2007).

Most of the work supporting the claim of MEP hypothesis fall into two categories. The studies in the first category share a common use of very simple energy balance models (such as the one used by Paltridge) where the MEP climate can be solved analytically. These analytic solutions are then validated via some qualitative comparison to the observations on Earth and planetary atmospheres (Lorenz et al. 2001; Jupp and Cox 2010; Fukumura and Ozawa 2014). However, it has been questioned whether the qualitative agreements reported in these studies are truly physically significant (Goody 2007). Studies in the second category take advantage of the comprehensive GCMs that represent our state-of-the-art understanding of the climate system. Due to their complexity, solving for the MEP climate is not feasible in these models, and the validation of the MEP hypothesis relies instead on tuning the models' unconstrained parameters to verify the existence of a local maximum in entropy production as a function of these parameters (Kleidon et al. 2003, 2006; Kunz et al. 2008). However, the entropy production has also been found to depend monotonically on certain parameters, resulting in no maximum state (Pascale et al. 2012a).

Obviously, both approaches have their own caveats and ambiguity. Also, none of these studies help place the MEP hypothesis into our existing knowledge framework for the dynamics of planetary atmospheres. For the studies in the first category, their models simply do not resolve the motions in the atmosphere. It is then unclear how to discuss atmospheric dynamics in this context (e.g. Rodgers 1976; Goody 2007). For the studies in the second category, one can easily show that entropy production in GCMs depends on the external parameters whose effect on the climate involves the

fluid dynamics of the atmosphere, such as planetary rotation rate and the strength of surface friction (e.g. Pascale et al. 2013) and do not enter directly into the MEP calculation. It is again unclear why the fact that MEP hypothesis fails to predict the dependence on these external parameters is ignored in these studies. While the most appealing aspect of this hypothesis's claim is it being purely thermodynamic so that there is no need to consider the complex dynamics involved, this same aspect of the hypothesis also makes its claim very dubious when confronted with model simulations in which dynamical factors invisible to the thermodynamics clearly affect the resulting climate.

As one step toward better relating the MEP hypothesis to our understanding of the dynamics of the general circulation, an ideal system for study is the idealized GCM discussed in Chapter 2 (Held and Suarez 1994). As we explained there, this model has been one of the go-to models for studying the fundamentals of large-scale atmospheric dynamics. Many aspects of its climates, including the meridional temperature gradient, have been examined in previous studies as a function of model parameters (e.g. Schneider and Walker 2006; Zurita-Gotor 2008). The model's idealized physics has the total diabatic heating represented by a Newtonian relaxation scheme, allowing its MEP climate solution to be solved for analytically (Ito and Kleidon 2005). Also because of its idealized physics, the model's global entropy budget is well-defined and can be easily diagnosed (Zurita-Gotor et al. 2015). The model is therefore very well suited for assessing the MEP hypothesis in the context of the relatively well-studied model dynamics reported in the literature.

In the context of this idealized GCM, there have indeed been some studies on the MEP hypothesis. For instance, Kleidon et al. (2003) argued that the strength of surface friction given by Held and Suarez (1994) to simulate an Earth-like climate actually coincides with a local maximum of entropy production when they varied the friction. As we have discussed earlier, it is unclear why they interpreted this

particular result as a support for the MEP hypothesis, since the strength of surface friction is at least in part an external parameter that is a function of the physical system, specifically the roughness of the surface (Chai et al. 2016). Another example is Ito and Kleidon (2005), where the authors obtained the analytic solution for the model's MEP climate and compared directly with the numerical simulation. As we discuss later on, they miscalculated the entropy destruction in the MEP climate, which led them to conclude that the simulation is close to the MEP for standard Earth-like parameters, but actually they are far from each other.

Additionally, Ito and Kleidon (2005) explicitly discussed the differences in tropical temperature differences in the MEP and simulated Earth-like climate. They attributed this discrepancy to the fact that the MEP hypothesis does not consider angular momentum conservation. They optimistically predicted but did not demonstrate that the MEP hypothesis under such an extra constraint would still be useful. This is an example of another approach toward the MEP hypothesis, which modifies the original claim by stating that the climate maximizes entropy production subject to some constraints. The problem with the approach is a lack of guidance on how to search for these extra constraints. It can make the hypothesis difficult to disprove, since it is always possible to claim that one has not as yet uncovered the correct constraints to be applied. Furthermore, as more constraints are added to the variational calculation, the problem can eventually become fully constrained and the value of a variational principle then vanishes (Goody 2007).

Motivated by a need to better clarify these problems with the MEP hypothesis in the context of this idealized GCM, the study in this chapter is carried out for two main purposes. First, we wish to convey that the MEP climate is dramatically different from the simulated climate because it totally messes up its prediction for the thermal stratification, which plays a crucial role in determining the strength of global entropy cycle in this model. In the spirit of looking for constraints that rescue the value of

the MEP hypothesis, we demonstrate that by using the thermal stratification as a constraint, the results look superficially promising. However, upon a deeper analysis it will be shown that this promise is misleading, in that this constraint is in a sense too strong for the variational principle to be useful, at least in the particular idealized GCM under study.

The rest of the chapter is organized as follows. In Section 5.2, we begin by describing in more details the idealized GCM and its MEP solution. In Section 5.3, we explain why the MEP solution is problematic as the entropy destruction is expected to be dynamically related to the thermal stratification as well as the meridional temperature gradient. We also derive a scaling relation between the entropy destruction and the horizontal mean thermal stratification. In Section 5.4, we explore an alternative, constrained, MEP solution that satisfies this scaling relation. In Section 5.6, we further study this constrained MEP solution to better understand its properties and interpret its physical meaning. Finally, in Section 5.6, we describe and address some potential criticisms that we anticipate of our calculations and we conclude with their implications on tackling the problem of the MEP hypothesis.

5.2 The idealized GCM and its MEP solution

In Chapter 2, we have introduced the idealized GCM, which is a primitive-equation model on the sphere. Yet, to make this chapter self-contained, we here repeat some of its traits that are directly relevant to the following analysis. We note that the model is global, with the spectral prognostic variables projected onto a longitude and latitude (ϕ) grid as needed, and its vertical coordinate is described by σ levels, where $\sigma = p/p_s$ is the ratio between the pressure p and the surface pressure p_s and $0 \leq \sigma \leq 1$ at every horizontal grid point. The most idealized aspect of the model is the use of Held and Suarez (1994)'s physical package. The model is thermally forced with the

total diabatic heating (Q) parameterized as a Newtonian relaxation term,

$$Q = -c_p k_T \left(T - T_{eq}\right), \tag{5.1}$$

where T is temperature, T_{eq} is the temperature at pure radiative equilibrium, and k_T is an inverse timescale that characterizes how fast Q damps T back to T_{eq}. The constant c_p is the specific heat capacity of the dry air. The model does not include water vapor and has no latent heating. Once the circulation is generated, the associated kinetic energy is constantly removed by a hypoviscosity term at the small scales and a surface friction term at the large scales. The latter is also simply parameterized as a Rayleigh drag confined in the lowest model levels.

To ensure this set of physical parameterization produces an Earth-like climate in some basic respects, Held and Suarez (1994) defined T_{eq} and k_T as

$$T_{eq} = max\left\{200K, [315K - \Delta_y \sin^2\phi - \Delta_z log(p/p_0)\cos^2\phi](p/p_0)^\kappa\right\}, \tag{5.2a}$$

$$k_T = k_a + (k_s - k_a) max\left(0, \frac{\sigma - \sigma_b}{1 - \sigma_b}\right)\cos^4\phi, \tag{5.2b}$$

where $\kappa = R/c_p$ with R the ideal gas constant, the constants $p_0 = 1000hPa$, $\Delta_y = 60K$, $\Delta_z = 10K$, $\sigma_b = 0.7$, $k_a^{-1} = 40days$, and $k_s^{-1} = 4days$. We refer to the above parameter values as the control values and the corresponding simulation as the control simulation. Several aspects of Eq. (5.2) are worth clarifying, as they will be important for the discussion in the following sections. First, both T_{eq} and k_T are independent of time and longitude, so the model's radiative equilibrium as well as its climates are zonally symmetric and independent of time. Second, the radiative equilibrium state is statically stable in the tropics and slowly approaches to neutral in the extratropics. Because the model does not have any subgrid-scale convective adjustment, any further stabilization beyond that in radiative equilibrium is done by the resolved large-scale dynamics. Third, the uniform and relatively long timescale

in the free troposphere k_a is designed to represent radiative cooling, while a shorter timescale k_s imposed in the nominal boundary layer ($\sigma \leq \sigma_b$) is to mimic the heating by surface heat fluxes, which are larger in the tropics and decrease with the latitude. This spatial structure of k_T is important, as would be shown later, for the discussion in Section 5.5.

With the above information on Q, we now solve for the analytic solution of the model's MEP climate. Assuming that p_s can be approximated by a constant, T_{eq} and k_T are only functions of ϕ and σ. The MEP temperatures $T_{mep}(\phi, \sigma)$ is then the solution for $\bar{T}(\phi, \sigma)$ (where bar denotes for the time and zonal mean) which maximizes the global mass integral (represented by the angle brackets) of negative diabatic entropy destruction

$$S \equiv -\left\langle \frac{\bar{Q}}{\bar{T}} \right\rangle = \left\langle \frac{c_p k_T (\bar{T} - T_{eq})}{\bar{T}} \right\rangle \tag{5.3}$$

among all the possible $\bar{T}(\phi, \sigma)$ where

$$\left\langle \bar{Q} \right\rangle = -\left\langle c_p k_T (\bar{T} - T_{eq}) \right\rangle = 0. \tag{5.4}$$

Following Ito and Kleidon (2005), we can solve this variational problem using Lagrange multiplier. That is, the local $T_{ji} = T_{mep}(\phi_j, \sigma_i)$ satisfies

$$\begin{cases} f(T_{ji}) = \left\langle \frac{k_T (T_{ji} - T_{eq})}{T_{ji}} \right\rangle \\ g(T_{ji}) = -\left\langle k_T (T_{ji} - T_{eq}) \right\rangle \\ \nabla_{T_{ji}} f(T_{ji}) = \lambda \nabla_{T_{ji}} g(T_{ji}) \end{cases}$$

where λ is the Lagrange multiplier for the imposed constraint. This gives

$$T_{mep} = \lambda^{-1/2} T_{eq}^{1/2},$$

and we can solve for λ by substituting this expression into the constraint Eq. (5.4) to get

$$\lambda = \frac{\left\langle k_T T_{eq}^{1/2} \right\rangle}{\langle k_T T_{eq} \rangle}.$$

Therefore, the analytic form for T_{mep} is simply

$$T_{mep} = (\frac{\langle k_T T_{eq} \rangle}{\langle k_T T_{eq}^{1/2} \rangle})^{\frac{1}{2}} T_{eq}^{\frac{1}{2}}, \tag{5.5}$$

and a corollary that follows is

$$\frac{\partial \ln T_{mep}}{\partial \ln \phi} = \frac{1}{2} \frac{\partial \ln T_{eq}}{\partial \ln \phi}. \tag{5.6}$$

That is, the meridional temperature gradient in the MEP climate would be about half of its value at radiative equilibrium.

For the control parameters, Fig. 5.1a shows the vertically averaged meridional profiles of three temperatures: T_{eq}, T_{mep}, and the simulated $\bar{T}$ from the idealized GCM. As expected from Eq. (5.6), the meridional gradient of T_{mep} is about half of the meridional gradient of T_{eq}. Also, the meridional gradient of T_{mep} gives an excellent prediction for the meridional gradient of the simulated $\bar{T}$, which might prompt one to believe the MEP hypothesis does have some value. However, T_{mep} also shows a robust warm bias relative to $\bar{T}$. Since both T_{mep} and simulated $\bar{T}$ have to obey Eq. (5.4), this provides a hint that, while the meridional gradients of the two temperatures look similar in terms of the vertical average, their detailed spatial patterns must be quite different. To demonstrate one of these differences, we have also compared the meridional profiles of the lowest level ($\sigma = 0.98$) temperatures (Fig. 5.1b). From this view, T_{mep} exhibits a cold bias at all latitudes and substantially underestimates the meridional gradient of the simulated $\bar{T}$. It therefore indicates that T_{mep} is not as promising as one would have expected by only considering the vertical average.

Likewise, we can also look at the horizontally averaged vertical profiles of these temperatures (Fig. 5.1c). Based on the same reasoning behind Eq. (5.6), we expect the vertical temperature gradient in the MEP climate to be

$$\frac{\partial \ln T_{mep}}{\partial \ln \sigma} = \frac{1}{2}\frac{\partial \ln T_{eq}}{\partial \ln \sigma}, \tag{5.7}$$

which is also about half of its value at radiative equilibrium. On the other hand, the simulated $\bar{T}$ actually deviates little from radiative equilibrium. T_{mep} is then unquestionably much more stable than the simulated $\bar{T}$, explaining why it consistently underestimates the horizontally averaged temperatures at lower vertical levels while overestimates the vertical average. This is another way to state the important differences between the MEP climate and the simulated climate.

In fact, Pascale et al. (2012b) also reported a similar discrepancy in a different model. They compared the MEP solution of a two-dimensional (meridional and vertical) gray radiation atmosphere with its corresponding (three-dimensional) GCM simulation. They also found that the MEP solution gives a good estimate for the meridional temperature gradient but noticeable differences exist in their vertical temperature structures. In their case, the MEP's vertical temperature profile looks more troublesome than our case, as it is convectively unstable. Note from Eq. (5.2) that if the lapse rate in radiative equilibrium is sufficiently unstable, it will remain unstable in the MEP state. The MEP solution procedure knows nothing about gravitational stability. This simple point clearly shows that the MEP climate cannot always be valid.

Along with the discrepancy in the mean thermal stratification, we underline that the MEP climate is also found to overestimate the global diabatic entropy destruction (S) in our control simulation. Substituting Eq. (5.5) into Eq. (5.3) and let $p_s = p_0$, we get $S \approx 8.6\ wm^{-2}$ for the MEP climate. S is here expressed in the energy dissipation

rate unit by multiplying the entropy destruction rate with a reference temperature of $300K$ following Zurita-Gotor et al. (2015). This reference temperature is simply a way to convert the units of the entropy destruction rate to units that are more familiar. The model simulation gives the much lower value of $S \approx 2.3\ wm^{-2}$ instead. As we mentioned in Section 5.1, the same calculation has been performed by Ito and Kleidon (2005), who reported the values for the MEP and the model simulation as $S \approx 8.4\ wm^{-2}K^{-1}$ ($\sim 2.5\ wm^{-2}$) and $S \approx 6\ wm^{-2}K^{-1}$ ($\sim 1.8\ wm^{-2}$), respectively. While the difference between their and our simulated S values can be explained by the different model resolutions used (Zurita-Gotor et al. 2015), we suspect they may have made an error when converting from entropy production to energy dissipation units for their MEP value.

Clearly, it is difficult to argue that MEP's S is close to the simulation, and it can only be harder to justify MEP's seemingly useful prediction on the vertically averaged meridional temperature gradient (for these control parameters). The original MEP argument fails to recognize that as important as the meridional structure of $\bar{T}$ to the determination of S is the vertical structure of $\bar{T}$, whose role is missing in Paltridge's model. In the next section, we explain why the thermal stratification is closely related to S by considering their dynamical relations in this idealized GCM.

5.3 Relating the mean thermal stratification to the strength of global entropy cycle

Consider the local energy balance between the restoring due to diabatic forcing and dynamical heat fluxes,

$$\frac{1}{\bar{\rho}} \frac{\partial \overline{\rho v \theta cos\phi}}{a cos\phi \partial \phi} + \frac{\partial \overline{\omega \theta}}{\partial p} \approx \frac{\bar{Q}}{c_p} \left(\frac{\bar{p}}{p_0} \right)^{-\kappa}, \tag{5.8}$$

where ρ is density, $\omega = dp/dt$ is pressure velocity, and $\theta = T(p/p_0)^{-\kappa}$ is potential temperature. The rhs of the equation contains the information of the mean diabatic heating. The lhs contains the information of the heat fluxes transported by the fluid, which can be related to the dynamics of the circulation. We here illustrate the two particular ways that Eq. (5.8) exerts control on the thermodynamic fields.

As in Chapter 2, following Held (2007), we can substitute Eq. (5.8) into Eq. (5.3) and obtain an expression for the global entropy destruction with an integration by parts,

$$S \approx -\left\langle \left(\frac{\bar{p}}{p_0}\right)^{\kappa} \frac{c_p}{\bar{\rho}} \frac{\overline{\rho v \theta}}{\bar{T}} \left. \frac{\partial \ln \bar{T}}{a \partial \phi} \right|_m \right\rangle, \tag{5.9}$$

where m denotes the surface along which the heat flux is aligned. That is, the slope of m is determined by the bulk ratio of the vertical and horizontal heat fluxes. This equation has been introduced as Eq. (2.6) and investigated in Chapter 2. While there is some fuzziness about how to diagnose m in the idealized GCM, we have showed Eq. (5.9) is consistent with the model simulations semi-quantitatively. As argued there, since the vertical heat flux cannot be zero, m is never exactly horizontal. S is therefore determined by not only the mean meridional temperature gradient but also the vertical temperature gradient. In other words, if one is to think of S as determined by a flux times a temperature gradient, the determination of S is a two-dimensional problem owing to the sloping nature of the dynamic heat fluxes. Eq. (5.9) thus serves as a reminder for why getting the mean thermal stratification right is vital to getting the strength of the entropy cycle right.

Second, we can also derive a more straightforward scaling relation between S and the mean thermal stratification taking advantage of the Newtonian relaxation form of Q. After replacing the rhs of Eq. (5.8) by Eq. (5.1), we differentiate Eq. (5.8) with p and perform the horizontal average at each σ level (denoted by the squared

brackets) to get

$$\frac{\partial^2[\overline{\omega\theta}]}{\partial p^2} \approx -\frac{\partial}{\partial p}[k_T\left(\bar{\theta} - \theta_{eq}\right)]. \tag{5.10}$$

The lhs of this equation depends only on the vertical heat flux, which we further connect to S via

$$\frac{\partial^2[\overline{\omega\theta}]}{\partial p^2} \sim \frac{p_0}{R}\frac{\langle\overline{\omega\alpha}\rangle}{\delta p^2} \sim \left(\frac{p_0 T_\epsilon}{R(\delta p)^2}\right) S, \tag{5.11}$$

where $\alpha = \rho^{-1}$ and δp is defined as the effective pressure depth. The ideal gas law gives the first scaling. The second scaling is derived by noticing the equality of energy conversion and kinetic energy dissipation (i.e. $\langle\overline{\omega\alpha}\rangle = \epsilon$) and the dominance of kinetic energy dissipation to the total entropy production in this model (i.e. $\epsilon/T_\epsilon \approx S$).

Physically, the rhs of Eq. (5.10) measures the differential diabatic heating in the vertical, which is mostly between the upper troposphere and the boundary layer. To modify it for an explicit dependence on mean thermal stratification, we consider the atmosphere as two layers, whose averaged $[\bar{\theta}]$ and $[\bar{\theta}_{eq}]$ differences are denoted as $\delta\theta$ and $\delta\theta_{eq}$, respectively. We next define an effective diabatic forcing strength k_{T0} that allow us to simplify the rhs of Eq. (5.10) as

$$\frac{\partial}{\partial p}[k_T\left(\bar{\theta} - \theta_{eq}\right)] \sim \frac{k_{T0}}{\delta p}(\delta\theta - \delta\theta_{eq}). \tag{5.12}$$

Eqs. (5.11) and (5.12) together suggest an intimate relation between S and $\delta\theta$,

$$S \sim K(\delta\theta - \delta\theta_{eq}), \tag{5.13}$$

where $K = R(\delta p)(k_{T0})(p_0 T_\epsilon)^{-1}$. This scaling relation is simply stating that the strength of global entropy cycle is controlled by the overall strength of the vertical heat flux and thus the vertical differential diabatic heating, which in turn is set by the mean thermal stratification when the diabatic heating is in the form of Newtonian relaxation. This relation has been used to explain how the climate varies with external

parameters in other studies where the diabatic heating is also in the form of Newtonian relaxation (Held 2007; Zurita-Gotor and Vallis 2010; Jansen and Ferrari 2013a).

We have also tried to evaluate Eq. (5.13)'s ability to predict the climates of the idealized GCM by examining a set of the model simulations that we have examined in Chapter 2. They are similar to the control simulation (the one described in Section 5.2) except for either their planetary rotation rate (Ω) or the meridional temperature gradient at radiative equilibrium (Δ_y in Eq. (5.2)), which are varied individually while keeping all other parameters fixed. To use Eq. (5.13), we assume K is approximately unchanged in all our simulations. We estimate $\delta\theta$ as the difference of simulated $[\bar{\theta}]$ at $\sigma = 0.35$ and $\sigma = 0.98$. Likewise, $\delta\theta_{eq}$ is calculated in the similar manner.

In Fig. 5.2, we plot the estimated $\delta\theta - \delta\theta_{eq}$ against the simulated S from these model simulations, with the set of simulations where we vary Ω separated from the simulations where we vary Δ_y in a different panel. The key finding of Fig. 5.2 is the reasonable fit of Eq. (5.13) to the simulations, verifying and restating the close relation between S and the mean thermal stratification. It is also worth emphasizing that the cases with varying Ω all share the same MEP solution since the MEP solution depends only on k_T and T_{eq} (as shown in Eq. (5.5)). Fig. 5.2 makes an obvious point that the MEP solution alone cannot predict the changes in S and $\delta\theta - \delta\theta_{eq}$ with Ω. It is therefore another simple clear demonstration of MEP's problem.

5.4 Imposing a constraint on the mean thermal stratification

The above investigation emphasizes MEP's limitations in predicting the thermal stratification (Section 5.2) and its violation of a scaling relation derived from the dynamic equations (Section 5.3). However, our interpretation of the inaccuracy of its predicted thermal stratification can be overturned by arguing that the MEP hypothesis

should be considered only once the thermal stratification is known. This may be a way to rescue the hypothesis and interpret Paltridge's results. It then leads us to ask whether there is a chance that the MEP climate would give a better behaved prediction if we explicitly constrain the thermal stratification in the variational problem. In this section, we study an alternative climate solution which maximizes S only among the climates that share the same horizontal mean thermal stratification as the simulation and thus automatically satisfy Section 5.3's scaling relation. We refer to this constrained MEP solution as the CMEP solution.

Given the simulated horizontally averaged potential temperature at every σ levels ($\vartheta(\sigma)$), CMEP solution is obtained by maximizing Eq. (5.3) subject to Eq. (5.4) and the following additional constraints

$$[\bar{T}(\phi, \sigma_i)\sigma_i^{-\kappa}] - [\vartheta(\sigma_i)] = 0 \tag{5.14}$$

at each equally-spaced σ_i, where $i = 1, 2, ..., n$ and n is the total number of the levels. Similar to the derivation for the MEP solution (Section 5.2), we introduce $n+1$ Lagrange multipliers (λ, λ_1, λ_2, ..., λ_n) for $n+1$ constraints. The local CMEP temperature $T_{ji} = T_{cmep}(\phi_j, \sigma_i)$ then satisfies

$$\begin{cases} f(T_{ji}) = \left\langle \frac{k_T(T_{ji} - T_{eq})}{T_{ji}} \right\rangle \\ g(T_{ji}) = -\left\langle k_T(T_{ji} - T_{eq}) \right\rangle \\ g_i(T_{ji}) = [\vartheta(\sigma_i)] - [T_{ji}(\phi, \sigma_i)\sigma_i^{-\kappa}] \\ \nabla_{T_{ji}} f(T_{ji}) = \lambda \nabla_{T_{ji}} g(T_{ji}) + \sum_{i=1}^{n} \lambda_i \nabla_{T_{ji}} g_i(T_{ji}) \end{cases}$$

This gives different T_{cmep} expressions for different σ levels, i.e.,

$$T_{cmep}(\sigma_i) = (\lambda k_T(\sigma_i) + \lambda_i \sigma_i^{-\kappa})^{-1/2} (k_T(\sigma_i) T_{eq}(\sigma_i))^{1/2},$$

for $i = 1, 2, ..., n$. Again, substituting this expression into the constraints Eqs. (5.4) and (5.14), a system of nonlinear equations with $n+1$ unknowns and $n+1$ constraints is then closed. However, unlike MEP solution, we can only solve this numerically.

With the numerically solved T_{cmep}, we can next calculate the corresponding S. For the control simulation, since the horizontal variations in p_s are negligible, the simulated horizontally averaged potential temperature is the simulated horizontally averaged temperature shown in Fig. 5.1c multiplying by the corresponding σ^κ at each level. Given this $\vartheta(\sigma)$, we obtain $S \approx 2.7\ wm^{-2}$ for the CMEP climate. Compared to the MEP climate ($S \approx 8.6\ wm^{-2}$), this is a great improvement as it now has the same order of magnitude as the simulated $S \approx 2.3\ wm^{-2}$ for the control climate. As in Section 5.3, we also perform the calculations for the other climates with varying Ω and Δ_y. For each of these different climates, we diagnose the corresponding $\vartheta(\sigma)$ from the model simulation and take it as the input parameter to compute its corresponding CMEP solution. Fig. 5.3 shows the S predicted by the CMEP solution as a function of these parameters. We can see that the CMEP's prediction is useful for tracking the variations in simulated S. For the scaling purpose, it is very good at predicting the changes with Δ_y and with Ω larger than Earth's value. It is not self-evident at first glance that this nice behavior of the CMEP solution is to be expected. While superficially promising, we proceed to explain that its seeming success is nonetheless a somewhat trivial result.

5.5 Interpreting the constrained MEP solution

As shown in Fig. 5.3, the CMEP solution can reasonably explain the parameter dependence of S seen in the simulations. However, the purpose of the MEP hypothesis is also to explain the meridional temperature gradient. We here try to interpret the CMEP solution by further examining its meridional temperature gradient. We first

show that the CMEP solution faces more difficulties in predicting the parameter dependence of the simulated meridional temperature gradient. We then discuss a special limit where the CMEP solution gives a problematic prediction on meridional temperature gradient. In doing so, we explain why its seeming success can be explained by the fact that it can, to a large extent, be considered overconstrained.

In Fig. 5.4, we plot the control climate's temperature profiles as shown in Fig. 5.1, but for the simulated $\bar{T}$ and the CMEP solution. We explicitly plot the vertical profiles of the horizontally averaged temperature to reconfirm that the CMEP solution is by design sharing the same $\vartheta(\sigma)$ with the simulation, as that is what we have explicitly constrained. Focusing first on the vertically averaged temperatures, we see that the CMEP solution slightly overestimates the meridional gradient of the simulated $\bar{T}$. For the lowest level temperatures, the deviation of CMEP solution from the simulated $\bar{T}$ are amplified, giving about a $10K$ cold bias in the poles and thus a $10K$ bias in the equator-to-pole temperature difference.

This discrepancy regarding the predicted lowest level meridional temperature gradient is worth more attention as it is indicating that the CMEP solution can only predict the simulated $\bar{T}$ qualitatively. To underscore the significance of this discrepancy, we also calculate the projection coefficients of the lowest level meridional temperature on the second Legendre polynomial in all the simulations and present them in Fig. 5.5 in the same way as Fig. 5.3. For the varying Ω cases, the $10K$ bias seen on the control climate persists to our largest Ω simulations and leads to a physically implausible prediction of a projection coefficient larger than $60K$, i.e., its corresponding value for the radiative equilibrium. For the varying Δ_y cases, the absolute value of the temperature bias in these projection coefficients is amplified for larger Δ_y. Therefore, if the concern is the lowest level meridional temperature gradient (Fig. 5.5) rather than the entropy destruction rate (Fig. 5.3), CMEP solution no longer looks as promising as it first appeared.

Another aspect of the CMEP solution's meridional temperature gradient that is worth a further illustration is for the special case when k_T in Eq. (5.2) is spatially uniform. When k_T is independent of ϕ and σ, the global energetic constraint, i.e., Eq. (5.4), is reduced to

$$\left\langle \bar{T} \right\rangle - \left\langle T_{eq} \right\rangle = 0. \tag{5.15}$$

This constraint is now redundant in the variational problem after we impose Eq. (5.14), i.e., the set of the constraints on the mean potential temperature at every σ levels. By getting rid of Eq. (5.4), the CMEP solution can be solved as

$$T_{cmep}(\sigma_i) = (\lambda_i \sigma_i^{-\kappa})^{-1/2} (k_T(\sigma_i) T_{eq}(\sigma_i))^{1/2} \tag{5.16}$$

with λ_i obtained by substituting the above expression into Eq. (5.14); it can then be written analytically as

$$T_{cmep}(\sigma_i) = \frac{[\vartheta(\sigma_i)]}{[T_{eq}(\sigma_i)^{1/2}]} T_{eq}(\sigma_i)^{1/2} \tag{5.17}$$

for $i = 1, 2, ..., n$. Likewise, we can also simplify the MEP solution as

$$T_{mep} = \frac{\langle T_{eq} \rangle}{\left\langle T_{eq}^{1/2} \right\rangle} T_{eq}^{1/2}. \tag{5.18}$$

If we compare the CMEP and MEP solutions, in this special case of uniform k_T, we immediately see that they share the same meridional temperature structure $T_{eq}^{1/2}$ but only different by their absolute values. That is, with uniform k_T, constraining the mean potential temperature at every σ level and thus the mean static stability no longer affects the meridional temperature structure. The CMEP solution is no longer able to explain the meridional temperature gradient's dependence on any parameter other than T_{eq}. We then immediately see that it would then fail to predict the changes

in meridional temperature gradient with Ω. (We note that while we do not conduct the uniform k_T simulations with varying Ω, we are confident that the Ω dependence in these simulations is qualitatively similar to the one reported in Fig. 5.5 as it is fundamentally controlled by the dynamics as discussed in Chapter 2 which does not rely on k_T being spatially variable. The fact that the meridional temperature gradient increases as Ω increases is illustrated in the GCM of Kaspi and Showman (2015) and in many other studies.)

In fact, the essence of the CMEP solution is likely best explained by considering a one-level atmosphere ($n = 1$, $\sigma_n = 1$) as studied by Paltridge (1975, 1978). With this minimum vertical structure case, the CMEP solution is equivalent to the MEP solution if k_T is spatially uniform, i.e., Eqs. (5.17) and (5.18) are identical. If k_T has spatial structure, given Eq. (5.14), the temperature of CMEP solution can be written without loss of generality as

$$T(\phi) = (\sum_{k=1}^{\infty} c_{2k} P_{2k}(\sin\phi) + \vartheta), \tag{5.19}$$

where $P_{2k}(\sin\phi)$ is the $2k$-th Legendre polynomial (as a function of $\sin\phi$), c_{2k} is its coefficient, and ϑ is a constant representing the global mean temperature that is given in Eq. (5.14). To obtain the CMEP solution, the coefficients, c_{2k} for $k = 1, 2, ..., \infty$, are optimized to maximize S in the variational problem subject to Eq. (5.4).

However, if we consider an approximation $c_{2k} = 0$ for $k \geq 2$, that is, the meridional temperature difference takes the simplest possible structure of the second Legendre polynomial ($P_2(\sin\phi)$), Eq. (5.19) becomes $T(\phi) = (c_2 P_2(\sin\phi) + \vartheta)$ which is then left with one degree of freedom, i.e., c_2. This degree of freedom is further eliminated by Eq. (5.4), so in the end the solution is fully constrained without any room for variational calculations. In other words, when imposing Eq. (5.14), we have effectively constrained the value of c_2, or equivalently, the equator-to-pole temperature differ-

ence. Therefore, unless the temperature structure is not dominated by $P_2(\sin\phi)$, the variational calculations only provides extra information on the higher order terms, i.e., c_{2k} for $k \geq 2$, which play secondary roles instead. From this perspective, we are then giving us too much prior knowledge when constructing the CMEP solution, and its seeming success is more naive than we would like it to be. Consistent with our previous results, these extra calculations verify again that there is nothing special about the MEP climates, whether with or without a constraint imposing on the mean thermal stratification.

5.6 Summary and discussion

In this chapter, we investigate the MEP hypothesis in the idealized GCM forced by Held-Suarez physics. For the standard setting described in Held and Suarez (1994), we show that the model's MEP climate has its vertically averaged meridional temperature gradient similar to the GCM's numerical simulation, but its horizontally averaged vertical temperature gradient is much smaller than the simulated. We argue that this failure on predicting the mean thermal stratification is of zeroth-order important for indicating that the MEP hypothesis does not hold in the model. This is because, in the process of searching for the MEP climate, the MEP hypothesis is not aware of that not every spatial structures of the diabatic heating can be maintained by the dynamic heat fluxes at the statistically steady state, i.e., not any arbitrary $Q(\phi, \sigma)$ is guaranteed to satisfy Eq. (5.8). To be accordance with Eq. (5.8), the entropy destruction (S) is related to both meridional and vertical temperature gradients described by Eq. (5.9). For Q parameterized as Newtonian relaxation, we further illustrate that S is also simply scaled with the differentiate diabatic heating and with the mean potential temperature differences in the vertical. This scaling relation (Eq. (5.13)) is verified in a set of model simulations with different planetary rotation rates and equator-to-pole

temperature differences at radiative equilibrium. Therefore, if one accepts the MEP's trouble in accurately estimating the vertical temperature gradient as a negligible detail, one must also accepts that the MEP climate violates the scaling relation and the dynamic and thermodynamic governing equations of the system on which it is based. Indeed, we have confirmed that the S predicted by the MEP climate is one order of magnitude larger than the simulated S, which makes it very hard to justify even the MEP climate's partial relevance to the simulation.

It is also worth noting that these results may have direct implications on the validity of another variational principle which postulates that the equilibrated climate prefers to maximize the strength of the kinetic energy cycle as opposed to the entropy cycle (Lorenz 1960; Pascale et al. 2012b). In the idealized GCM and for its simulations that we have studied, the two are nonetheless almost equivalent, because the entropy production in these model simulations comes mostly from the dissipative heating of kinetic energy dissipation and the dissipation occurs in the boundary layer whose temperature changes reflects little on the changes of its associated entropy production (Zurita-Gotor et al. 2015). Due to the simplicity, we can infer that the climates in these simulations are also not maximizing their strengths of the kinetic energy cycle. One can also easily recover Eqs. (5.9) and (5.13) from the available potential energy budget. Thinking from the available potential energy perspective, it becomes even more obvious that the mean thermal stratification plays an indispensable role in determining the rate of available potential energy generation. Hence, the ability for the MEP climate to get a reasonable meridional temperature gradient does not promise that it is getting the right answer by getting the strengths of the entropy and kinetic energy cycles right, as it can be achieving this by meanwhile messing up the prediction for the vertical temperature gradient.

The importance of the mean thermal stratification in the idealized GCM, however, makes our results difficult to connect with the results of Paltridge (1975, 1978), since

his model only has the meridional dimension. Motivated by this incompatibility, we ask whether it would instead be useful to consider an alternative MEP problem of the idealized GCM, whose solution is obtained under some constraint on the candidate climates' mean vertical thermal structure. We explore a specific solution that maximizes S among the climates whose horizontally average mean potential temperature is same as the model simulation at each vertical level, so the solution automatically satisfies the scaling relation between S and the vertical potential temperature differences we have identified. This solution, i.e., the CMEP solution, turns out to explain the simulated S very well in the model climates we have studied. To understand its seemingly promising result, we examine its prediction on the meridional temperature gradient. We show that the CMEP solution is less successful in explaining the simulated meridional temperature gradient. Also, in the limit of vanishing vertical dimension, the CMEP solution has its largest meridional temperature structure mostly set by the extra constraint and is considered to be a trivial result without enough room for variational calculations. Putting these different lines of reasoning together, we conclude that constraining the mean vertical thermal stratification unfortunately does not make the MEP hypothesis more convincing.

Evidently, this second part of our results depends heavily on the particular way that we impose constraints on the mean thermal stratification. Whether it is a good practice to make our two-dimensional variational problem more comparable to the one-dimensional variational problem considered by Paltridge remains questionable. In fact, relative to our specific calculations, we view that identifying and emphasizing this uncertainty in reconciling the MEP hypothesis in the two different model contexts as a more important message to convey. Interpreting this knowledge gap differently can lead us to ask different interesting questions. First, one can simply refuse to acknowledge the gap by arguing that the MEP hypothesis is not meant to apply to the idealized GCM, as the idealized GCM is by construction only a crude representation

of the real climate. Though, this would then force one to also deny the generality of the hypothesis and to face another question about how to determine whether the hypothesis shall hold in a certain system of interest or not. Alternatively, one can argue that it is strictly speaking the column-integrated diabatic heating divided by the surface temperature, rather than S, being maximized in Paltridge's calculations. We should instead maximize this quantity in the idealized GCM to better connect with Paltridge's model. In doing so, we are however already reinterpreting Paltridge's result differently from what is stated in the MEP hypothesis.

On the other hand, one can still remain optimistic about the existence of a clever way to constrain the system so that the MEP hypothesis, once considered with this ideal constraint, becomes valid. One can then criticize that the constraints we have adopted are not chosen well, which make our solution unable to demonstrate this possibility. Effectively, our calculations have instead demonstrated Goody (2007)'s concern on applying the MEP hypothesis to climate models. He discussed the difficulty of searching for dynamically justified constraints on the MEP hypothesis, and he cautioned regarding the subtlety that too strong or too many constraints can ultimately result in the unnecessary of invoking MEP. These concerns are vividly exemplified by our calculations. Our initial pursuit of this study is motivated by asking whether the search for the dynamical constraints envisioned by Goody (2007) might be easier in this relatively well understood idealized GCM. We in the end still find it a conundrum even in the context of this model.

If anything, we believe that the above discussion also reflects the most important reason why it is so hard to reach a general agreement regarding the MEP hypothesis' validity. Essentially, there is not even a general agreement upon the definitions of the classes of models and of the variational problems for which it is relevant. Hence, perhaps a more reasonable question to ask is, given that we still need to define the applicable systems and study extra constraints by understanding the dynamics and

physics of energy transport in climate models, what is left for the merit of studying the MEP hypothesis, which was supposed to help us avoid all these hard tasks? Regardless of how one thinks about the MEP hypothesis, it therefore seems for now that efforts directed to studying individual climate processes, including the eddy equilibration in the extratropical troposphere, remain essential.

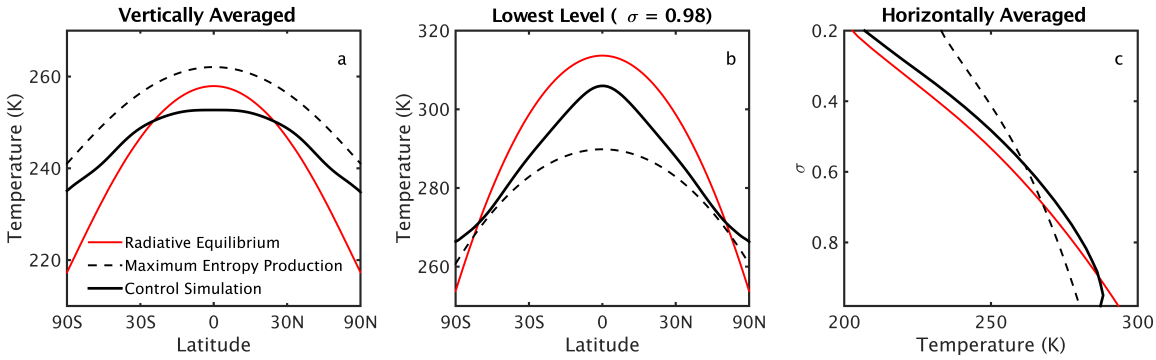

Figure 5.1: The temperature structures in three climates: the radiative equilibrium (red), the MEP solution (dashed black), and the control simulation (solid black). Shown from left to right are (a) meridional profiles of the vertically averaged temperature, (b) meridional profiles of the lowest-level temperature, and (c) vertical profiles of the horizontally averaged temperature.

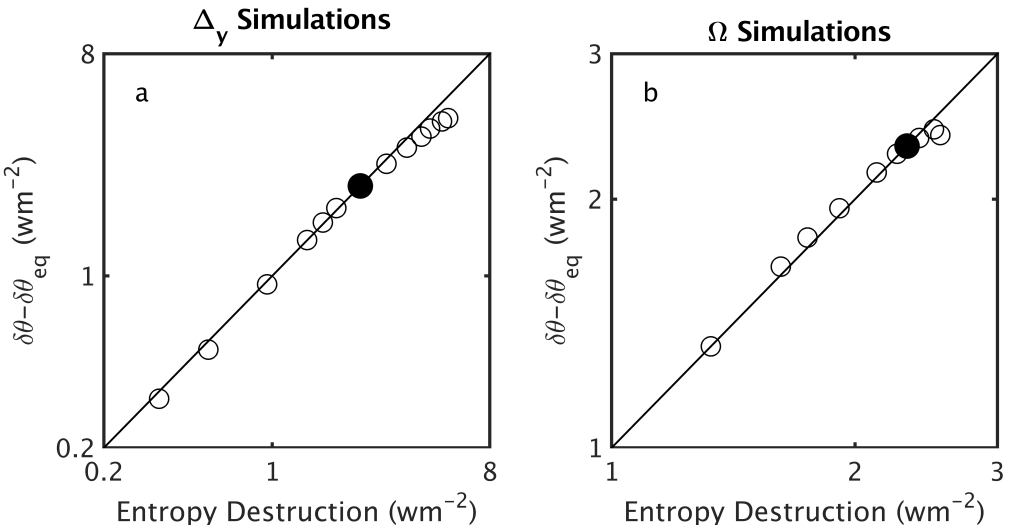

Figure 5.2: Simulated entropy destruction versus the prediction based on the vertical potential temperature difference in Eq. (5.13). The simulations with varying (a) Δ_y and (b) Ω are shown separately. The black solid dot denotes for the control climate. Its prediction by Eq. (5.13) is multiplied by a constant to ensure a perfect fit to the simulated value. The predictions for all other cases are then normalized by this constant accordingly.

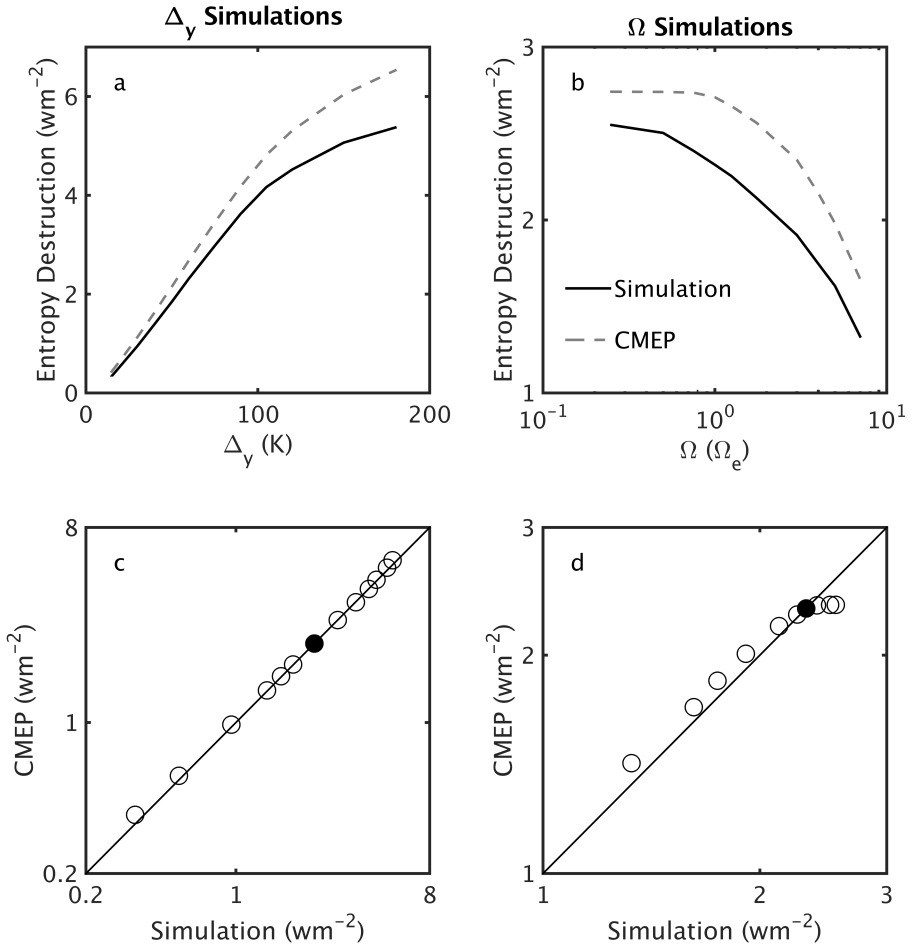

Figure 5.3: A comparison of the entropy destruction in three climates: the numerical simulation (black) and the CMEP solution (dashed gray). Upper panels show the entropy destruction as a function of (a) Δ_y and (b) Ω, respectively. Lower panels plot the simulated entropy destruction versus the one computed from the CMEP solution for the varying (c) Δ_y and (d) Ω simulations, respectively.

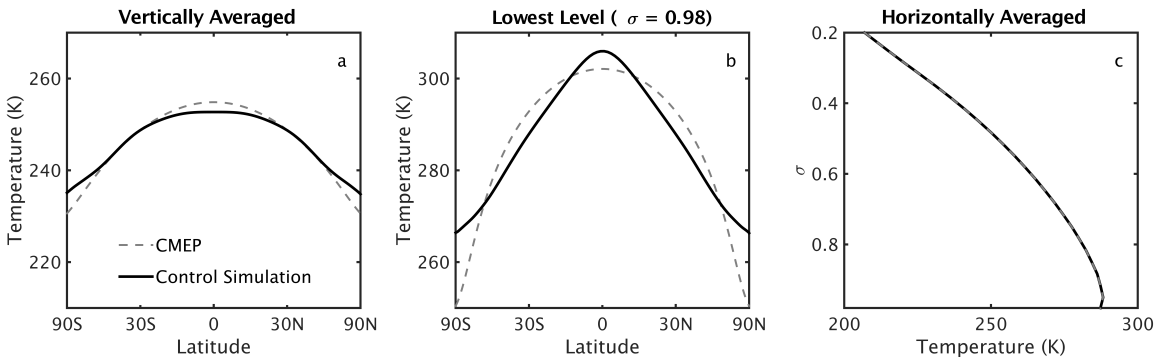

Figure 5.4: As in Fig. 5.1, but for the control simulation (solid black) and its corresponding CMEP solution (dashed gray).

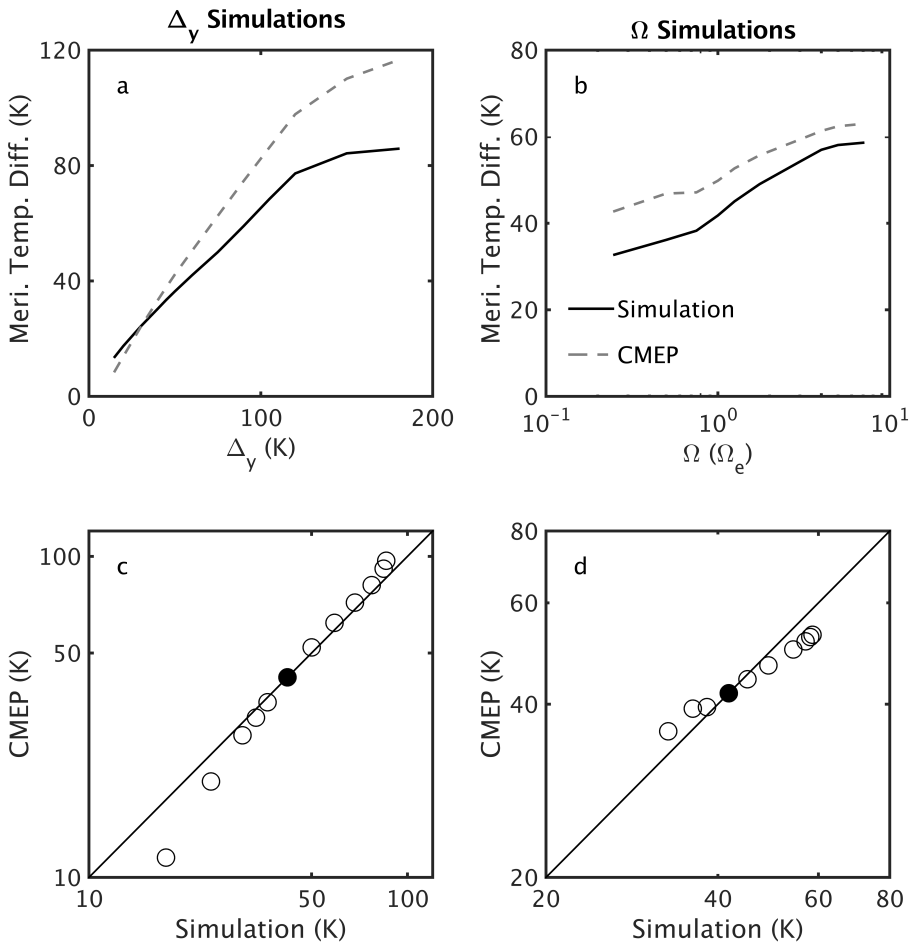

Figure 5.5: As in Fig. 5.3, but for the meridional temperature difference evaluated at the lowest model level ($\sigma = 0.98$) as the estimated value for the projected coefficient of the second Legendre polynomial.

Chapter 6

Conclusion

The age-old quest for a theory of eddy equilibration in the extratropical troposphere has motivated numerous work on its various aspects. Since the subject is in its essence a turbulence system, these research have to tackle a single aspect and a single complexity at a time by studying a particular model for the extratropical troposphere that is idealized in the other aspects. Progress has been made using a hierarchy of idealized models but with gaps left between them reflecting our lack of knowledge on the overall problem. This thesis contributes by filling some of these knowledge gaps, with one focus on the idealized dry GCM and (Chapter 2 and Chapter 5) and another on the two-layer QG models (Chapter 3 and Chapter 4). We here summarize our findings to redefine the state of our knowledge. We conclude by discussing some possible directions for the future pursuit on the problem.

6.1 Summary of the findings

We have participated mostly in re-examining studies criticizing or proposing modifications to the theory of Held and colleagues developed in the two-layer QG context but potentially having wider relevance (Fig. 1.1). To explain how the eddies equilibrate in the idealized models of the extratropical troposphere, all these theories

involve some assumptions on the determination of the diffusivity for the meridional eddy heat flux, the kinetic energies of eddies, the mixing length of eddies, and the strengths of global kinetic energy and entropy cycles. The recurring theme of this thesis is then to study and clarify the similarities and differences in the assumptions among the various theories and the extent to which they hold in various models and their parameter regimes.

In Chapter 2, we compared the theory of Held and Larichev (1996) with the theory of Barry et al. (2002) for the eddy heat flux diffusivity in the idealized GCM forced by Held-Suarez physics. The two theories are similar in assuming that the Rhines scale acts as the mixing length and that the relation between eddy kinetic energy and kinetic energy dissipation is determined by classic inverse energy cascade arguments. They differ however in how they relate kinetic energy dissipation to the characteristics of the mean state, with Barry et al. (2002) claiming the superiority of the entropy budget over available potential budget used in Held and Larichev (1996). We investigated how well these assumptions hold in the model climates that are departures from an Earth-like control climate obtained by varying the radiative equilibrium equator-to-pole temperature difference and planetary rotation rate. We showed that while the Rhines scale assumption explains all the simulations nicely, the inverse energy cascade argument is not always valid. In addition, the different kinetic energy dissipation scaling used in the two theories are found to be reconcilable by a more general form, and a heuristic approach to diagnose it within the simulations is presented. These results help in resolving the seeming controversy on the relevant thermodynamic budgets assumed in the two theories and illustrating their true difference as being in the assumptions concerning the effective mixing slope for the eddy heat flux. In addition, the results also point to a mismatch between the baroclinic model simulations and the inverse energy cascade arguments, derived from

the barotropic QG theory. It hence directly motivates Chapter 3's reassessment of this part of Held and Larichev (1996)'s theory.

In Chapter 3, we investigated the problems with the inverse energy cascade arguments in the simplest baroclinic systems, that is, the two-layer QG models. In these models, both β and surface friction can control the equilibrated scales of baroclinic eddies by stopping the inverse cascade. A scaling theory on how surface friction alone sets these scales is proposed by Held (1999) in the case of a quadratic drag law. However, the theory breaks down when friction is modeled by linear damping, and there are other reasons to suspect that it is oversimplified. An ideal system to test the theory is the model in the homogeneous limit with quadratic damping and $\beta = 0$. We studied the model's numerical simulations and identified two reasons for the theory's breakdown: the asymmetry between two layers due to confinement of friction to the lower layer and the deviation from a spectrally local inverse energy cascade due to the spread of wavenumbers over which energy is input into the barotropic mode. We analyzed the former by comparing the simulations with drag appearing asymmetrically or symmetrically between the two layers. We addressed the latter with a heuristic modification of Larichev and Held (1995)'s theory designed to fit the simulations. We then made a comparison between quadratic and linear drag simulations to discuss our modified argument's connection to Thompson and Young (2006)'s competing theory based on the dynamics of equivalent barotropic vortices with thermal signatures. Following Pavan and Held (1996), we also presented an example of an inhomogeneous statistically steady state to argue that the diffusivity obtained from the homogeneous model has relevance to more realistic configurations.

In Chapter 4, we studied the extent to which the lessons learned in the $\beta = 0$ case can provide insights to understanding the nonzero β cases, when eddy heat flux diffusivity is seen to depend on β and surface friction. For simplicity, we focused on the homogeneous QG two-layer model simulations with the quadratic friction of the

same damping strength appearing in the both layers. By purposely setting it up to minimize its difference from the stirred barotropic model, the model again allows us to better restore the theoretical connection between the heat flux diffusivity in the two-layer turbulence and the passive tracer diffusivity in the barotropic turbulence. Thompson and Young (2007) have argued that the dynamics of the two systems are too different for our knowledge of one diffusivity to be easily transferred to the other. With the help of Kong and Jansen (2017)'s recent progress on understanding the barotropic passive tracer diffusivity, we found that a missing link between the two diffusivities can be recovered, to a large extent, after we took into account of two aspects of the important dynamics. One is the suppression of mixing by the eddy phase propagation relative to the mean flow due to the presence of β. The other is the effect of the spectrally nonlocal energy input into the barotropic mode, which we identified in Chapter 3. This second effect introduces the deformation radius as a necessary parameter for characterizing the diffusivity even if there is large separation between the radius of deformation and the energy-containing scale. Throughout the analyses, the results are also presented and discussed in the way to enable a direct comparison with Lapeyre and Held (2003) and Chapter 2's idealized GCM results.

In Chapter 5, we tested the maximum entropy production (MEP) hypothesis of Paltridge (1975, 1978). We asked whether it can explain the climate mean states of the idealized GCM so that the efforts on detailed understanding of the eddy dynamics can be avoided. While this theory cannot be adequate in its unmodified form, we considered it worthy of a closer look to help understand the possibility for useful modification. We first analytically solved for the temperatures at the MEP state, whose mean thermal stratification is much stable than the one in the model simulation. This hypothetical state is unlikely to be relevant to the simulated climate since its thermal stratification is wrong and given the known important role of static stability in determining the strength of of entropy cycle discussed in Chapter 2. We also de-

rived another closer scaling relation between the bulk static stability and the entropy destruction to underscore how the climate of the MEP state violates our understanding of the model's dynamics. Since Paltridge's results are originally proposed for a model without a vertical dimension, we considered an alternative hypothetical state maximizing the entropy production among all the states possessing the same global mean vertical temperature profile as the simulation. We demonstrated that this new hypothetical state reproduces many features of the simulated climate. However, upon further examination, it is found that this constraint is too strong in the sense that the variational calculation adds little to the quality of the fit, due to the particular formulation of the forcing in the idealized GCM. Thus, its promising results have little interest for the purpose of improving our knowledge on this topic. We therefore concluded a step by step investigation on eddy dynamics, such as through Chapter 2 to Chapter 4, is still necessary to advance our understanding of the climate.

6.2 Directions for future work

6.2.1 Connecting back to barotropic turbulence

One of our key results is to reemphasize the gap between our understanding of two-layer QG turbulence and our understanding of barotropic QG turbulence. We showed that the classic dual cascade framework still holds generally, as the two-layer model's barotropic eddy kinetic energy spectrum is still determined by the local wavenumber and local energy cascade flux. However, the latter is itself wavenumber dependent, distinct from the Kolmogorov's inertial range observed typically in the barotropic models stirred at small scales. This is certainly due to the two-layer model's spectrally nonlocal energy transfer from the baroclinic to the barotropic mode, but we only characterized it with a simple functional form and did not provide an explanation for why it takes this form. To better understand its dynamics, extensive calculations on

the individual triad interactions as described in Salmon (1978, 1980) are likely needed to provide further insights.

Alternatively, an entirely different view to approach the problem is to completely abandon the inverse energy cascade arguments and focus rather on the roles of coherent structures, i.e., vortices and zonal jets, in shaping the eddy statistics in the two-layer models (Thompson and Young 2006, 2007). In this thesis, we touched on these coherent structures a little bit, but we did not carefully examine this view. Whether it can be reconciled with the inverse energy cascade arguments remains unclear to us. If one is to pursue this direction, we feel it is important to stress that the coherent structures can also exist in the stirred barotropic models (e.g. Panetta 1993; Grianik et al. 2004). Careful work in parallel on the stirred barotropic and self-stirred two-layer problems is needed so that one more easily identifies the complexities introduced by the baroclinic dynamics. To bridge the two problem, our two-layer model with symmetric drag should remain ideal for this purpose.

6.2.2 Introducing spatial inhomogeneity

Among the (horizontally) homogeneous two-layer models we studied, spatial inhomogeneity appears as the domain averaged differences between the upper and lower layers in two specific setups: asymmetric drag with $\beta = 0$ and symmetric drag with nonzero β. The former has its layer asymmetry arising from the bottom confinement of surface friction, whose complexity is not fully addressed in this thesis. To compare this two-layer model with the real atmosphere, one can assume that the strength of the quadratic damping needs to be rescaled to account for the friction only applying to the boundary layer, a small portion of the entire vertical extent. Therefore, the effective quadratic damping strength may be smaller given the same frictional coefficient. The extent to which this simple rescaling works may be interesting to study

by comparing a series of models with increasing number of vertical layers but with friction presenting only in the lowest layer.

The model with symmetric drag and nonzero β, on the other hand, has different dynamics in the two layers due solely to the presence of β. This layer asymmetry nevertheless is not considered explicitly in our eddy heat flux analysis, which seems to be inconsistent with the earlier work that highlights its importance to these fluxes (Lapeyre and Held 2003; Thompson and Young 2007). The discrepancy here is likely related to the fact that our analysis did not take the advantage of the fact that the heat flux diffusivity approaches to zero as β approaches to its critical value. This implies, perhaps, that our analysis is more justifiable if the strength of β is not too large. The limit of stronger β deserves a more detailed investigation.

Moving away from the homogeneous models, we also showed that the homogeneous diffusivity, once properly normalized, predicts the local diffusivity observed in the channel model that includes meridional inhomogeneity. An important feature of the inhomogeneous model is that its eddies are also damped thermally, since thermal relaxation, representing radiative forcing, is a necessary feature of the model. Within the parameter range we described in this thesis, the effects of thermal damping are too small to quantify. Yet, we did find it important in other cases, especially to maintain an substantially narrower and sharper jet. Thus, it is an aspect of the model that we believe shall be studied more cautiously, before we try to understand when the inhomogeneity becomes significant enough for the eddies in these flows to deviate from the homogeneous limit. Relative to the nonzero β cases in Pavan and Held (1996), our $\beta = 0$ and quadratic drag simulations are an easier starting point to quantify these potential deviations and to ask whether the inhomogeneous results can be explained by considering some spatial average derived from the homogeneous theory even when the homogeneous theory becomes inaccurate locally.

6.2.3 Determining the thermal stratification

A strong limitation of QG is that the static stability is prescribed. By contrast, the static stability in the primitive-equation systems is an internal degree of freedom. Wherever its information is needed for the idealized GCM calculations, we simply used the diagnosed static stability from the simulations and did not develop a closed theory. To achieve the latter goal, additional relations between the static stability and the other variables in the theory have to be provided (e.g. Held 1982). These relations can be based on the prior knowledge on how the system is diabatically forced. For the diabatic forcing parameterized as Newtonian relaxation, an example is the scaling relation between the static stability and the entropy destruction we derived from considering the vertical heat fluxes. A similar approach was taken by Jansen and Ferrari (2013a) following Held (2007) to form a closed theory for a multi-layer Boussinesq channel model. There are however two subtleties about their theory. First, it only provides a crude estimate of the mean thermal stratification rather than its entire vertical profile. Zurita-Gotor (2008) examined an idealized GCM (similar to ours) and found that, in some parameter ranges, it is important to distinguish the bulk stability defined in the pressure coordinate and the gross stability defined in the isentropic coordinate. The latter appears to be more intimately related to the strength of kinetic energy cycle. In fact, an equivalent way to state this difference is that the mixing slope is not always the same as the isentropic slope, as in the expression we derived to connect the kinetic energy dissipation and the mean thermal structure. While we understand that this complexity arises from the direct interaction between the eddies and the diabatic forcing, we are unsure how to best quantify its importance. Sorting out this uncertainty may thus be a prerequisite to develop theories for the thermal stratification that are adequate for closure theories.

6.2.4 Toward a moist theory

As envisioned by Lorenz (1978), the roles of water vapor in the climate has become one of this century's central focus of study. On the problem of moist eddy equilibration in the extratropical troposphere, its recent progress can be described similarly to that on the dry problem, divided these research into two schools. From the (quasi-)linear prospective, O'Gorman (2011) tried to incorporate the moisture into the linear baroclinic instability theory by directly replacing the dry static stability with an effective one which considers the latent heating effect on the mean thermal stratification. However, O'Gorman et al. (2018) also reported limitations of this perspective in an idealized moist GCM's simulations of a warming climate. On the other hand, From the turbulence perspective, the most promising results seem to be concentrating on the discussion of the Rhines scale. Also studying an idealized moist GCM, Frierson et al. (2006) showed that the equilibrated eddy energy containing length scale is explained well by Rhines scale (at the latitude of maximum eddy kinetic energy). In Frierson et al. (2007), they found that Rhines scale can be further used as an eddy mixing length estimate for determining the meridional energy transport, consistent with the Barry et al. (2002) study discussed in depth in this thesis. Indeed, the Rhines scale's relevance to different measures of the eddy length scales has been later confirmed in other simulations of idealized GCMs, although the reason for the relevance seems to leave some room for different interpretations (Chai and Vallis 2014; Chemke and Kaspi 2015). We did not pin down an exact explanation for the Rhines scale's relevance, but our results reveal that its emergence in both the idealized GCM and two-layer QG models cannot be simply attributed to Rhines (1975)'s original cascade halting argument. Given Rhines scale's repeatedly appearance in a variety of systems and an unsatisfied understanding of its underlying dynamics, even in the simplest models, it is likely an important piece of the puzzle to link the dry and moist theories and is worth more systematic research across the levels of the model hierarchy.

6.3 In a nutshell

For the readers who wish to quickly skim a few key points in this thesis, we present a list of the summary points in the following, along with a corresponding schematic plot of the before/after view on the core concepts involved in each chapters (Fig. 6.1) and how they piece together in understanding the the eddy equilibration in the extratropical troposphere (Fig. 6.2).

SUMMARY POINTS

1. The strength of kinetic energy (entropy) cycle is determined by the heat transport between the heating and cooling regions. This heat transport is not oriented horizontally but along a sloping surface. A theory for this slope is a requirement for a satisfying closure theory (Chapter 2).

2. The energy in the two-layer models transfers from the baroclinic to barotropic mode. This energy transfer is not confined at the scale of deformation radius but spreads over a range of larger scales, causing departures from expectations based on classical barotropic inverse cascade theory (Chapter 3).

3. The heat flux diffusivity is reduced in the presence of β. This is not only because β halts the energy cascades at smaller scales than would otherwise be the case, but also because β causes the eddies to propagate zonally and shortens the effective mixing distance in the meridional direction (Chapter 4).

4. The atmosphere is a thermally-driven heat engine whose strength is determined internally by the dynamic and physical properties of its fluid. It does not necessarily maximizing its entropy production or kinetic energy dissipation (Chapter 5).

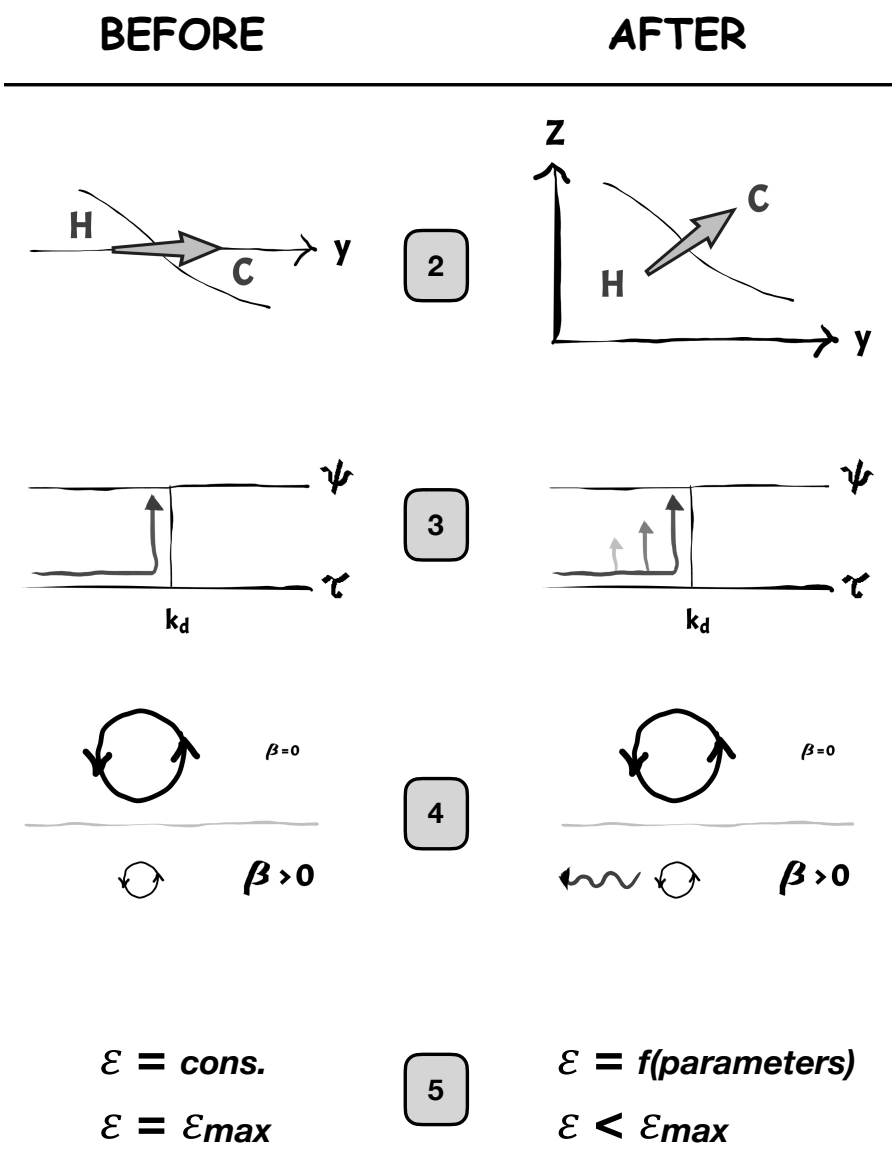

Figure 6.1: A schematic plot of the before and after views with the numbered ovals indicating the corresponding chapters (see the "SUMMARY POINTS" text box).

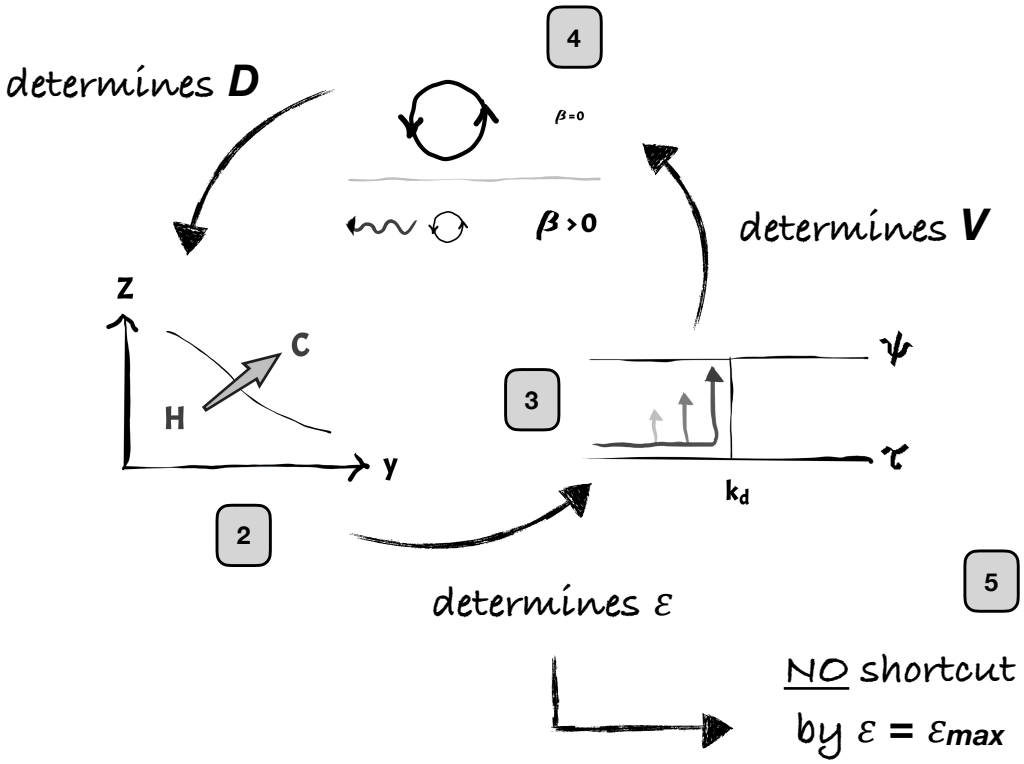

Figure 6.2: As in Fig. 6.1, but for the illustration of how the core concepts described in "SUMMARY POINTS" fit together.

Bibliography

Arbic, B. K., and G. R. Flierl, 2004: Baroclinically unstable geostrophic turbulence in the limits of strong and weak bottom ekman friction: Application to midocean eddies. *Journal of Physical Oceanography*, **34 (10)**, 2257–2273.

Arbic, B. K., and R. B. Scott, 2008: On quadratic bottom drag, geostrophic turbulence, and oceanic mesoscale eddies. *Journal of Physical Oceanography*, **38 (1)**, 84–103.

Barry, L., G. C. Craig, and J. Thuburn, 2002: Poleward heat transport by the atmospheric heat engine. *Nature*, **415 (6873)**, 774–777.

Branscome, L. E., 1983: A parameterization of transient eddy heat flux on a beta-plane. *Journal of the Atmospheric Sciences*, **40 (10)**, 2508–2521.

Cehelsky, P., and K. K. Tung, 1991: Nonlinear baroclinic adjustment. *Journal of the Atmospheric Sciences*, **48 (17)**, 1930–1947.

Cessi, P., 2008: An energy-constrained parameterization of eddy buoyancy flux. *Journal of Physical Oceanography*, **38 (8)**, 1807–1819.

Chai, J., 2016: Understanding geostrophic turbulence in a hierarchy of models. Ph.D. thesis, Princeton University, 211 pp.

Chai, J., M. Jansen, and G. K. Vallis, 2016: Equilibration of a baroclinic planetary atmosphere toward the limit of vanishing bottom friction. *Journal of the Atmospheric Sciences*, **73 (8)**, 3249–3272.

Chai, J., and G. K. Vallis, 2014: The role of criticality on the horizontal and vertical scales of extratropical eddies in a dry GCM. *Journal of the Atmospheric Sciences*, **71 (7)**, 2300–2318.

Chang, C.-Y., and I. M. Held, 2019: The control of surface friction on the scales of baroclinic eddies in a homogeneous quasigeostrophic two-layer model. *Journal of the Atmospheric Sciences*, **76 (6)**, 1627–1643.

Charney, J. G., 1947: The dynamics of lone waves in a baroclinic westerly current. *Journal of Meteorology*, **4 (5)**, 136–162.

Charney, J. G., and M. E. Stern, 1962: On the stability of internal baroclinic jets in a rotating atmosphere. *Journal of the Atmospheric Sciences*, **19 (2)**, 159–172.

Chemke, R., and Y. Kaspi, 2015: The latitudinal dependence of atmospheric jet scales and macroturbulent energy cascades. *Journal of the Atmospheric Sciences*, **72 (10)**, 3891–3907.

Chemke, R., and Y. Kaspi, 2016: The effect of eddy-eddy interactions on jet formation and macroturbulent scales. *Journal of the Atmospheric Sciences*, **73 (5)**, 2049–2059.

Dewar, R. C., and A. Maritan, 2014: A theoretical basis for maximum entropy production. *Beyond the Second Law: Entropy Production and Non-equilibrium Systems*, R. C. Dewar, C. H. Lineweaver, R. K. Niven, and K. Regenauer-Lieb, Eds., Springer Berlin Heidelberg, Berlin, Heidelberg, 49–71.

Farrell, B. F., and P. J. Ioannou, 2008: Formation of jets by baroclinic turbulence. *Journal of the Atmospheric Sciences*, **65 (11)**, 3353–3375.

Ferrari, R., and M. Nikurashin, 2010: Suppression of eddy diffusivity across jets in the southern ocean. *Journal of Physical Oceanography*, **40 (7)**, 1501–1519.

Frierson, D. M. W., I. M. Held, and P. Zurita-Gotor, 2006: A gray-radiation aquaplanet moist GCM. Part I: Static stability and eddy scale. *Journal of the Atmospheric Sciences*, **63 (10)**, 2548–2566.

Frierson, D. M. W., I. M. Held, and P. Zurita-Gotor, 2007: A gray-radiation aquaplanet moist GCM. Part II: Energy transports in altered climates. *Journal of the Atmospheric Sciences*, **64 (5)**, 1680–1693.

Fukumura, Y., and H. Ozawa, 2014: Entropy production in planetary atmospheres and its applications. *Beyond the Second Law: Entropy Production and Non-equilibrium Systems*, R. C. Dewar, C. H. Lineweaver, R. K. Niven, and K. Regenauer-Lieb, Eds., Springer Berlin Heidelberg, Berlin, Heidelberg, 225–239.

Gent, P. R., and J. C. Mcwilliams, 1990: Isopycnal mixing in ocean circulation models. *Journal of Physical Oceanography*, **20 (1)**, 150–155.

Goody, R., 2007: Maximum entropy production in climate theory. *Journal of the Atmospheric Sciences*, **64 (7)**, 2735–2739.

Green, J. S. A., 1970: Transfer properties of the large-scale eddies and the general circulation of the atmosphere. *Quarterly Journal of the Royal Meteorological Society*, **96 (408)**, 157–185.

Grianik, N., I. M. Held, K. S. Smith, and G. K. Vallis, 2004: The effects of quadratic drag on the inverse cascade of two-dimensional turbulence. *Physics of Fluids*, **16 (1)**, 73–78.

Haidvogel, D. B., and I. M. Held, 1980: Homogeneous quasi-geostrophic turbulence driven by a uniform temperature gradient. *Journal of the Atmospheric Sciences*, **37 (12)**, 2644–2660.

Hallberg, R., 2013: Using a resolution function to regulate parameterizations of oceanic mesoscale eddy effects. *Ocean Modelling*, **72**, 92–103.

Held, I. M., 1978: The vertical scale of an unstable baroclinic wave and its importance for eddy heat flux parameterizations. *Journal of the Atmospheric Sciences*, **35 (4)**, 572–576.

Held, I. M., 1982: On the height of the tropopause and the static stability of the troposphere. *Journal of the Atmospheric Sciences*, **39 (2)**, 412–417.

Held, I. M., 1999: The macroturbulence of the troposphere. *Tellus A*, **51 (1)**, 59–70.

Held, I. M., 2005: The gap between simulation and understanding in climate modeling. *Bulletin of the American Meteorological Society*, **86 (11)**, 1609–1614.

Held, I. M., 2007: Progress and problems in large-scale atmospheric dynamics. *The Global Circulation of the Atmosphere*, T. Schneider, and A. H. Sobel, Eds., Princeton University Press, 1–21.

Held, I. M., and V. D. Larichev, 1996: A scaling theory for horizontally homogeneous, baroclinically unstable flow on a beta plane. *Journal of the Atmospheric Sciences*, **53 (7)**, 946–952.

Held, I. M., and M. J. Suarez, 1994: A proposal for the intercomparison of the dynamical cores of atmospheric general circulation models. *Bulletin of the American Meteorological Society*, **75 (10)**, 1825–1830.

Ito, T., and A. Kleidon, 2005: Entropy production of atmospheric heat transport. *Non-equilibrium Thermodynamics and the Production of Entropy: Life, Earth, and Beyond*, A. Kleidon, and R. D. Lorenz, Eds., Springer Berlin Heidelberg, Berlin, Heidelberg, 93–106.

Jansen, M., and R. Ferrari, 2012: Macroturbulent equilibration in a thermally forced primitive equation system. *Journal of the Atmospheric Sciences*, **69 (2)**, 695–713.

Jansen, M., and R. Ferrari, 2013a: Equilibration of an atmosphere by adiabatic eddy fluxes. *Journal of the Atmospheric Sciences*, **70 (9)**, 2948–2962.

Jansen, M., and R. Ferrari, 2013b: The vertical structure of the eddy diffusivity and the equilibration of the extratropical atmosphere. *Journal of the Atmospheric Sciences*, **70 (5)**, 1456–1469.

Jansen, M. F., A. J. Adcroft, R. Hallberg, and I. M. Held, 2015: Parameterization of eddy fluxes based on a mesoscale energy budget. *Ocean Modelling*, **92**, 28–41.

Juckes, M. N., 2000: The static stability of the midlatitude troposphere: The relevance of moisture. *Journal of the Atmospheric Sciences*, **57 (18)**, 3050–3057.

Jupp, T. E., and P. M. Cox, 2010: Mep and planetary climates: insights from a two-box climate model containing atmospheric dynamics. *Philosophical Transactions of the Royal Society B: Biological Sciences*, **365 (1545)**, 1355–1365.

Kaspi, Y., and A. P. Showman, 2015: Atmospheric dynamics of terrestrial exoplanets over a wide range of orbital and atmospheric parameters. *The Astrophysical Journal*, **804 (1)**, 60.

Kleidon, A., K. Fraedrich, E. Kirk, and F. Lunkeit, 2006: Maximum entropy production and the strength of boundary layer exchange in an atmospheric general circulation model. *Geophysical Research Letters*, **33 (6)**, L06 706.

Kleidon, A., K. Fraedrich, T. Kunz, and F. Lunkeit, 2003: The atmospheric circulation and states of maximum entropy production. *Geophysical Research Letters*, **30 (23)**, 2223.

Klocker, A., R. Ferrari, and J. H. LaCasce, 2012: Estimating suppression of eddy mixing by mean flows. *Journal of Physical Oceanography*, **42 (9)**, 1566–1576.

Kong, H., and M. F. Jansen, 2017: The eddy diffusivity in barotropic β-plane turbulence. *Fluids*, **2 (4)**.

Kunz, T., K. Fraedrich, and E. Kirk, 2008: Optimisation of simplified GCMs using circulation indices and maximum entropy production. *Climate Dynamics*, **30 (7)**, 803–813.

Lapeyre, G., and I. M. Held, 2003: Diffusivity, kinetic energy dissipation, and closure theories for the poleward eddy heat flux. *Journal of the Atmospheric Sciences*, **60 (23)**, 2907–2916.

Larichev, V. D., and I. M. Held, 1995: Eddy amplitudes and fluxes in a homogeneous model of fully developed baroclinic instability. *Journal of Physical Oceanography*, **25 (10)**, 2285–2297.

Lorenz, E. N., 1960: Generation of available potential energy and the intensity of the general circulation. *Dynamics of Climate*, R. Pfeffer, Ed., Pergamon Press, 86–92.

Lorenz, E. N., 1967: *The nature and theory of the general circulation of the atmosphere*. World Meteorological Organization, 161 pp.

Lorenz, E. N., 1978: Available energy and the maintenance of a moist circulation. *Tellus*, **30 (1)**, 15–31.

Lorenz, R. D., J. I. Lunine, P. G. Withers, and C. P. McKay, 2001: Titan, Mars and Earth : Entropy production by latitudinal heat transport. *Geophysical Research Letters*, **28 (3)**, 415–418.

Martyushev, L., and V. Seleznev, 2006: Maximum entropy production principle in physics, chemistry and biology. *Physics Reports*, **426 (1)**, 1–45.

Martyushev, L., and V. Seleznev, 2014: The restrictions of the maximum entropy production principle. *Physica A: Statistical Mechanics and its Applications*, **410**, 17–21.

Merlis, T. M., and T. Schneider, 2009: Scales of linear baroclinic instability and macroturbulence in dry atmospheres. *Journal of the Atmospheric Sciences*, **66 (6)**, 1821–1833.

North, G. R., 1975: Theory of energy-balance climate models. *Journal of the Atmospheric Sciences*, **32 (11)**, 2033–2043.

O'Gorman, P. A., 2011: The effective static stability experienced by eddies in a moist atmosphere. *Journal of the Atmospheric Sciences*, **68 (1)**, 75–90.

O'Gorman, P. A., T. M. Merlis, and M. S. Singh, 2018: Increase in the skewness of extratropical vertical velocities with climate warming: fully nonlinear simulations versus moist baroclinic instability. *Quarterly Journal of the Royal Meteorological Society*, **144 (710)**, 208–217.

O'Gorman, P. A., and T. Schneider, 2007: Recovery of atmospheric flow statistics in a general circulation model without nonlinear eddy-eddy interactions. *Geophysical Research Letters*, **34 (22)**, L22 801.

Ozawa, H., A. Ohmura, R. D. Lorenz, and T. Pujol, 2003: The second law of thermodynamics and the global climate system: A review of the maximum entropy production principle. *Reviews of Geophysics*, **41 (4)**.

Paltridge, G. W., 1975: Global dynamics and climate - a system of minimum entropy exchange. *Quarterly Journal of the Royal Meteorological Society*, **101 (429)**, 475–484.

Paltridge, G. W., 1978: The steady-state format of global climate. *Quarterly Journal of the Royal Meteorological Society*, **104 (442)**, 927–945.

Panetta, R. L., 1993: Zonal jets in wide baroclinically unstable regions: Persistence and scale selection. *Journal of the Atmospheric Sciences*, **50 (14)**, 2073–2106.

Pascale, S., J. M. Gregory, M. H. P. Ambaum, and R. Tailleux, 2012a: A parametric sensitivity study of entropy production and kinetic energy dissipation using the FAMOUS AOGCM. *Climate Dynamics*, **38 (5)**, 1211–1227.

Pascale, S., J. M. Gregory, M. H. P. Ambaum, R. Tailleux, and V. Lucarini, 2012b: Vertical and horizontal processes in the global atmosphere and the maximum entropy production conjecture. *Earth System Dynamics*, **3 (1)**, 19–32.

Pascale, S., F. Ragone, V. Lucarini, Y. Wang, and R. Boschi, 2013: Nonequilibrium thermodynamics of circulation regimes in optically thin, dry atmospheres. *Planetary and Space Science*, **84**, 48–65.

Pavan, V., and I. M. Held, 1996: The diffusive approximation for eddy fluxes in baroclinically unstable jets. *Journal of the Atmospheric Sciences*, **53 (9)**, 1262–1272.

Phillips, N. A., 1954: Energy transformations and meridional circulations associated with simple baroclinic waves in a two-level, quasi-geostrophic model. *Tellus*, **6 (3)**, 273–286.

Phillips, N. A., 1956: The general circulation of the atmosphere: A numerical experiment. *Quarterly Journal of the Royal Meteorological Society*, **82 (352)**, 123–164.

Rhines, P. B., 1975: Waves and turbulence on a beta-plane. *Journal of Fluid Mechanics*, **69 (3)**, 417–443.

Rhines, P. B., 1977: The dynamics of unsteady currents. *The Sea*, E. D. G. et al., Ed., Marine Modelling, Vol. 6, Wiley and Sons, 189–318.

Rodgers, C. D., 1976: Comments on Paltridge's minimum entropy exchange principle. *Quarterly Journal of the Royal Meteorological Society*, **102 (432)**, 455–458.

Salmon, R., 1978: Two-layer quasi-geostrophic turbulence in a simple special case. *Geophysical & Astrophysical Fluid Dynamics*, **10 (1)**, 25–52.

Salmon, R., 1980: Baroclinic instability and geostrophic turbulence. *Geophysical & Astrophysical Fluid Dynamics*, **15 (1)**, 167–211.

Schneider, T., 2004: The tropopause and the thermal stratification in the extratropics of a dry atmosphere. *Journal of the Atmospheric Sciences*, **61 (12)**, 1317–1340.

Schneider, T., and C. C. Walker, 2006: Self-organization of atmospheric macroturbulence into critical states of weak nonlinear eddy-eddy interactions. *Journal of the Atmospheric Sciences*, **63 (6)**, 1569–1586.

Schneider, T., and C. C. Walker, 2008: Scaling laws and regime transitions of macroturbulence in dry atmospheres. *Journal of the Atmospheric Sciences*, **65 (7)**, 2153–2173.

Scott, R. B., and F. Wang, 2005: Direct evidence of an oceanic inverse kinetic energy cascade from satellite altimetry. *Journal of Physical Oceanography*, **35 (9)**, 1650–1666.

Shaw, T. A., and Coauthors, 2016: Storm track processes and the opposing influences of climate change. *Nature Geoscience*, **9**, 656–664.

Smagorinsky, J., 1963: General circulation experiments with the primitive equations. *Monthly Weather Review*, **91 (3)**, 99–164.

Smith, K. S., G. Boccaletti, C. C. Henning, I. Marinov, C. Y. Tam, I. M. Held, and G. K. Vallis, 2002: Turbulent diffusion in the geostrophic inverse cascade. *Journal of Fluid Mechanics*, **469**, 13–48.

Smith, K. S., and G. K. Vallis, 2002: The scales and equilibration of midocean eddies: Forced-dissipative flow. *Journal of Physical Oceanography*, **32 (6)**, 1699–1720.

Stone, P. H., 1972: A simplified radiative-dynamical model for the static stability of rotating atmospheres. *Journal of the Atmospheric Sciences*, **29 (3)**, 405–418.

Stone, P. H., 1978a: Baroclinic adjustment. *Journal of the Atmospheric Sciences*, **35 (4)**, 561–571.

Stone, P. H., 1978b: Constraints on dynamical transports of energy on a spherical planet. *Dynamics of Atmospheres and Oceans*, **2 (2)**, 123–139.

Stone, P. H., and L. Branscome, 1992: Diabatically forced, nearly inviscid eddy regimes. *Journal of the Atmospheric Sciences*, **49 (4)**, 355–367.

Thompson, A. F., and W. R. Young, 2006: Scaling baroclinic eddy fluxes: Vortices and energy balance. *Journal of Physical Oceanography*, **36 (4)**, 720–738.

Thompson, A. F., and W. R. Young, 2007: Two-layer baroclinic eddy heat fluxes: Zonal flows and energy balance. *Journal of the Atmospheric Sciences*, **64 (9)**, 3214–3231.

Tulloch, R., J. Marshall, C. Hill, and K. S. Smith, 2011: Scales, growth rates, and spectral fluxes of baroclinic instability in the ocean. *Journal of Physical Oceanography*, **41 (6)**, 1057–1076.

Visbeck, M., J. Marshall, T. Haine, and M. Spall, 1997: Specification of eddy transfer coefficients in coarse-resolution ocean circulation models. *Journal of Physical Oceanography*, **27 (3)**, 381–402.

Welch, W. T., and K.-K. Tung, 1998: Nonlinear baroclinic adjustment and wavenumber selection in a simple case. *Journal of the Atmospheric Sciences*, **55 (8)**, 1285–1302.

Yuval, J., and Y. Kaspi, 2017: The effect of vertical baroclinicity concentration on atmospheric macroturbulence scaling relations. *Journal of the Atmospheric Sciences*, **74 (5)**, 1651–1667.

Zurita-Gotor, P., 2007: The relation between baroclinic adjustment and turbulent diffusion in the two-layer model. *Journal of the Atmospheric Sciences*, **64 (4)**, 1284–1300.

Zurita-Gotor, P., 2008: The sensitivity of the isentropic slope in a primitive equation dry model. *Journal of the Atmospheric Sciences*, **65 (1)**, 43–65.

Zurita-Gotor, P., J. Blanco-Fuentes, and E. P. Gerber, 2014: The impact of baroclinic eddy feedback on the persistence of jet variability in the two-layer model. *Journal of the Atmospheric Sciences*, **71 (1)**, 410–429.

Zurita-Gotor, P., I. M. Held, and M. F. Jansen, 2015: Kinetic energy-conserving hyperdiffusion can improve low resolution atmospheric models. *Journal of Advances in Modeling Earth Systems*, **7 (3)**, 1117–1135.

Zurita-Gotor, P., and R. S. Lindzen, 2006: A generalized momentum framework for looking at baroclinic circulations. *Journal of the Atmospheric Sciences*, **63 (8)**, 2036–2055.

Zurita-Gotor, P., and G. K. Vallis, 2009: Equilibration of baroclinic turbulence in primitive equations and quasigeostrophic models. *Journal of the Atmospheric Sciences*, **66 (4)**, 837–863.

Zurita-Gotor, P., and G. K. Vallis, 2010: Circulation sensitivity to heating in a simple model of baroclinic turbulence. *Journal of the Atmospheric Sciences*, **67 (5)**, 1543–1558.